UNIVERSITY OF CALIFORNIA
SANTA CRUZ

**Advanced Cathodes for Electrochemical Energy Storage Devices**

A dissertation submitted in partial satisfaction
of the requirements for the degree of

DOCTOR OF PHILOSOPHY
in
CHEMISTRY

by
**Dun Lin**
June 2023

The Dissertation of Dun Lin is approved:

_____
Professor Yat Li, Chair

_____
Professor Jin Zhong Zhang

_____
Professor Scott Oliver

_____
Peter F. Biehl
Vice Provost and Dean of Graduate Studies

## Table of Contents

## List of Figures

**Chapter 4**

## List of Tables

### Chapter 2



### Chapter 3

**Abstract**

**Advanced Cathodes for Electrochemical Energy Storage Devices**

by

Dun Lin

The growing awareness of the detrimental effects of fossil fuel consumption on the environment has led to an increased demand for sustainable and clean energy sources worldwide. This has driven the development and application of electrochemical energy storage devices (EESDs), including rechargeable batteries and supercapacitors, in order to better utilize intermittent renewable energy sources such as solar and wind power, and to provide continuous and reliable power supply. The cathodes of EESDs have been found to play a critical role in determining their performance, including specific capacity, output voltage, rate capability, energy/power density, and efficiencies, as well as their calendar life, thermal stability, cost, and environmental impact. Unfortunately, cathodes are still one of the major challenges in the advancements of EESDs. Developing advanced cathodes based on different electrochemical energy storage mechanisms, such as electric double-layer capacitance, pseudocapacitance, bulk ion insertion/desertion, and conversion reactions, has been an important task in order to fulfill the demands of EESDs for different application scenarios.

The scope of this dissertation covers the research of my past five years in designing and optimizing different types of cathodes for high-performance EESDs. Chapter one presents the background of EESDs and explains the advances of different

types of cathodes for EESDs. Chapter two introduces a 3D printed porous carbon cathode templated by microporous metal-organic framework, which serves as EDLC-type cathodes for aqueous zinc-ion hybrid capacitors with high areal capacitance and energy density. Chapter three focuses on the graded design of a 3D printed graphene aerogel substrate, which improves electrodeposition uniformity and electrochemical accessibility of ultrahigh-loading $MnO_2$ cathode based on lithium-ion insertion/desertion for non-aqueous lithium-ion hybrid capacitors with high volumetric energy density. A double-layered cathode dealing with the efficiency of iodide/iodine conversion chemistry for high-performance aqueous zinc-iodine batteries is discussed in Chapter four. Finally, in Chapter five, an outlook targeting the challenges and opportunities of developing advanced cathodes beyond cathode material itself is provided.

**Dedication**

DEDICATED

TO

MY PARENTS, LI LIN & SHAOYAN CHEN

## Acknowledgements

The past five years have undisputedly been the most extraordinary period of my life. Not only have I experienced unprecedented global clashes, crises, and changes, but also under such circumstances endeavored to complete my Ph.D. study and research at the beautiful campus of University of California, Santa Cruz with Pacific coastlines, redwood forests, and California sunshine. I feel such a blessing, during these five years, to stay alive and healthy, to acquire a wealth of knowledge, and to contribute to human progress. I always keep in mind that this journey cannot be accomplished without help from numerous people. Here I would like to express my sincere acknowledgements to everyone who has accompanied, supported, encouraged, and loved me along the way.

First and foremost, I would like to thank my nice advisor, Professor Yat Li. I still clearly remember our very first contact, when I hung up a strange number from the United States during a seminar, cautiously dialed back later in case it wasn't a spam call, and happily recognized him and his gentle voice. I will never forget how he expressed his interest in me and selflessly assisted with my program application, online interview, scholarship application, and admission. During my Ph.D. study, he always works hard, responds timely, and organizes things efficiently, setting up a great model for me. I like how he motivated me to come up with and try out my own ideas freely, while at the same time providing pivotal suggestions with his fast learning and critical thinking. He also cares about my life with his wholehearted support, warm encouragement, and enlightening wisdom, without which I cannot achieve what I am today. It's my great pleasure to be friends with him, to work with him, to trust and rely

on him, and more importantly, to learn from his knowledge, attitude, and personality. He really gave me more than I could give back.

My dissertation committee members, Prof. Jin Zhong Zhang, Prof. Yat Li, and Prof. Scott Oliver, along with Prof. Nobuhiko P. Kobayashi who served as the outside committee member of my qualification exam, also played a critical role in my pursuit of the Ph.D. title. They not only set up a high standard in evaluating my second-year seminar, qualification exam, and yearly reviews, but also gave me valuable advice and help all the way. Despite being strict in academics, they are actually kind and lovely people. I cannot thank you enough for your support for the past five years.

I would also like to thank many talented and dedicated peers who I am fortunate to work with and learn from during my time at University of California, Santa Cruz. I appreciate all the help from the doctors who graduated from the Li Lab: Dr. Gongming Wang, Dr. Yichuan Ling, Dr. Hanyu Wang, Dr. Yi Yang, Dr. Tianyu Liu, Dr. Tianyi Kou, Dr. Bin Yao, Dr. Megan Freyman, Dr. Mingpeng Chen, and Dr. Shanwen Wang; Graduate students who worked or are working in the Li lab: Daniel Bulmanh, Anica Pinongcos, Qiu Ren, Xinzhe Xue, Samuel Eisenburg, Ella Davidi, Riley Ball, and Nathan Delaney; Scholars who joined the Li lab: Prof. Xihong Lu, Prof. Teng Zhai, Dr. Mingyang Li, Prof. Yu Song, Prof. Zihang Huang, Dr. Jing Zhang, Dr. Huarong Peng, Dr. Xiaoli Fan, Prof. Wei Xu, Dr. Cheng Cheng, Dr. Lei Zhang, Dr. André Luiz Martins de Freitas, and Prof. Dewei Rao; Undergraduate students who worked in the Li Lab: Junzhe Kang, Dana Bryne, Soren Faulkner, Adam Carleton, Frances Li, Eric Po Ching Hsu, Emma Coester, and Ashley Middling; Community college and high school

students who worked with me: Andrew Martinez, Marisela Landaverde, Colin Chu, Ishan Roy, and Levente Ecsedi; Peers from Prof. Jin Zhong Zhang's lab: Dr. Ke Xu, Dr. Li Liu, Dr. Yan Sun, Heng Zhang, and Kai Chun (Kevin) Chou; Peers from Shaowei Chen's lab: Dr. Gabriella Jia-En Lu, Dr. Yi Peng, Dr. Bingzhang Lu, Dr. Chenzhong Yao, Qiming Liu, Dingjie Pan, Bingzhe Yu, and Tianchen Cui; Peers from Prof. Yuan Ping's lab: Chunhao Guo, Kejun Li, and Shimin Zhang; Peers from Prof. Alexander Ayzner's lab: Dr. Anna Johnston and Levi Matsushima; Peer from Prof. Scott Oliver's lab: Jeremy Barnett; Peer from Prof. Scott Lokey's lab: Panpan Zhang; Peer from Prof. Jevgenij Raskatov's lab: Ka Chan; Peers from other departments: Dr. Yang Xiang, Dr. Xiongbin Kang, Dr. Xiaotian Zheng, Dr. Wencheng Shao, Yan Zhang, Shijun Sun, Yiluan Song, Qiuxia Tang, Yannong He, Yifei Luo, Linfeng Wan, Yufei Si, Jiahao Luo, Vivian Zheng, Qianhui Shi, Xinyun Cui, Kejun Chen, Yi Liu, Dongyi Liu, Yufei Shan, Siyu Zhu, Xiaodong Zhang, Nan Wang, Jorge Ruiz Gonzalez, and many more.

I cannot complete my research work without professional external collaborators. I greatly appreciate my undergraduate advisor at Sun Yat-sen University, Prof. Xihong Lu, and his students for their continuous support; Prof. Gongming Wang and his research group at University of Science and Technology of China and Prof. Ming-Hsien Lee for teaching me density-functional theory calculations; Dr. Dewei Rao at Jiangsu University for conducting density-functional theory calculations for the zinc-iodine battery project; Dr. Tom Yuzvinsky in the W.M. Keck Center for Nanoscale Optofluidics at University of California, Santa Cruz for SEM image acquisitions; Dr.

Jennifer Lu at University of California, Merced and her team members: Dr. Jiasheng Qian, Samuel Chiovoloni, Han Lin Kuo, and Yaneth Hernandez for collaborations on multiple projects of energy storage devices; Scientists at Lawrence Livermore National Lab: Dr. Fang Qian, Dr. Cheng Zhu, Dr. Marcus Worsley, Dr. Swetha Chandrasekaran, Dr. Jean-Baptiste Forien, Dr. Noelle R. Catarineu, Dr. Diego I. Oyarzun, Dr. Mariana Desireé Reale Batista, Dr. Miguel Salazar de Troya, Dr. Thomas Roy, Dr. Victor A. Beck, Dr. Chris Orme, Dr. Zhen Qi, and Dr. Jianchao Ye, with whom we worked closely on multiple projects of 3D-printed energy storage devices; Prof. Bruce Dunn at University of California, Los Angeles and his students: Yunkai Luo, Bintao Hu, and Makena White, with whom we worked together on high-energy-density and high-power-density 3D-printed supercapacitors and other projects.

I also highly appreciate the generous financial support by the Chinese Scholarship Council-University of California, Santa Cruz Graduate Scholars Program for my Ph.D. study and research.

Last but not least, I would like to thank my family. Despite being separated by the Pacific Ocean and several time zones for nearly five years, they are always with me, whether I have fun things or good news to share, or mentally broken, or need to make major life decisions. I understand it takes a lot of courage for them to send their only son abroad to chase his dreams alone. I owe them too much, but I cherish everything they have done for me. My grandparents, uncles, aunts, and cousins also care about me at home and back me up all the way. My girlfriend, Yanfan Chen, has bravely joined

me on our lifelong adventures together. She lights up my world. Thank you all for being in my life. I love you all so much!

---

The text of this dissertation includes reprints of the following previously published materials:

1. Catarineu, N. R.*, **Lin, D.**† (equal contribution), Zhu, C., Oyarzun, D. I., and Li, Y., High-Performance Aqueous Zinc-Ion Hybrid Capacitors based on 3D Printed Metal-Organic Framework Cathodes. ***Chem. Eng. J.*** **2023**, *465*, 142544.
2. **Lin, D.**, Chandrasekaran, S., Forien, J.-B., Xue, X., Pinongcos, A., Coester, E., Worsley, M. A.*, and Li, Y.*, 3D-Printed Graded Electrode with Ultrahigh $MnO_2$ Loading for Non-Aqueous Electrochemical Energy Storage. ***Adv. Energy Mater.*** **2023**, *13*(20), 2300408.
3. **Lin D.**, Rao D., Chiovoloni S., Wang S., Lu J., and Li Y.*. Prototypical Study of Double-Layered Cathodes for Aqueous Rechargeable Static Zn-$I_2$ Batteries. ***Nano Lett.*** **2021**, *21*(9), 4129-4135.

# Chapter 1 - Introduction of Cathodes for Electrochemical Energy Storage Devices


## Abstract

As the negative consequences of fossil fuel consumption on the environment become more apparent, the global demand for clean and sustainable energy sources is increasing. The pursuit of better utilizing unstable renewable energy sources such as solar and wind power as well as reliably powering electronic products have stimulated the developments and applications of electrochemical energy storage devices (EESDs). The performances of EESDs, including rechargeable batteries and supercapacitors, have been significantly dictated by the cathodes. Unfortunately, cathodes are still one of the major challenges in the advancements of EESDs. Researchers have made substantial progress in developing cathodes based on different electrochemical energy storage mechanisms, including electric double-layer capacitance, pseudocapacitance, bulk ion insertion/desertion, and conversion reactions. This chapter presents the background of EESDs, fundamental concepts and working principles, as well as a brief overview of advances of different types of cathodes for EESDs.

## 1.1 Background

Due to the adverse effects of climate change caused by the burning of fossil fuels, the demand for clean and sustainable energy is increasing globally.[1-4] As renewable energy sources such as solar and wind power are becoming more prevalent, their intermittent nature has amplified the need to store excess energy generated during high-output periods and provide power during low-output periods.[5,6] At the same time, the wide spread of portable electronic devices, electric vehicles, and renewable energy systems has required reliable and efficient energy storage devices that can provide high energy density, fast charging, and long cycle life.[7,8] Electrochemical energy storage devices (EESDs), mainly including rechargeable batteries and supercapacitors, have thus been extensively developed by worldwide researchers and deployed in a huge variety of application scenarios according to their individual features (Figure 1.1a).[9] EESDs generally consist of several components, including an electrolyte, an anode, and a cathode (Figure 1.1b). The electrolyte is a medium that allows the transfer of ions between the anode and the cathode to complete the circuit. The cathode is the electrode that gains electrons from the anode through the outer circuit during discharging and outputs electrons during charging, while the anode does the opposite.[10]The input of electrons towards the cathode during discharging could initiate the electrostatic cation adsorption/anion desorption and/or the electrochemical reduction reactions.[11] Reverse processes occur during charging.

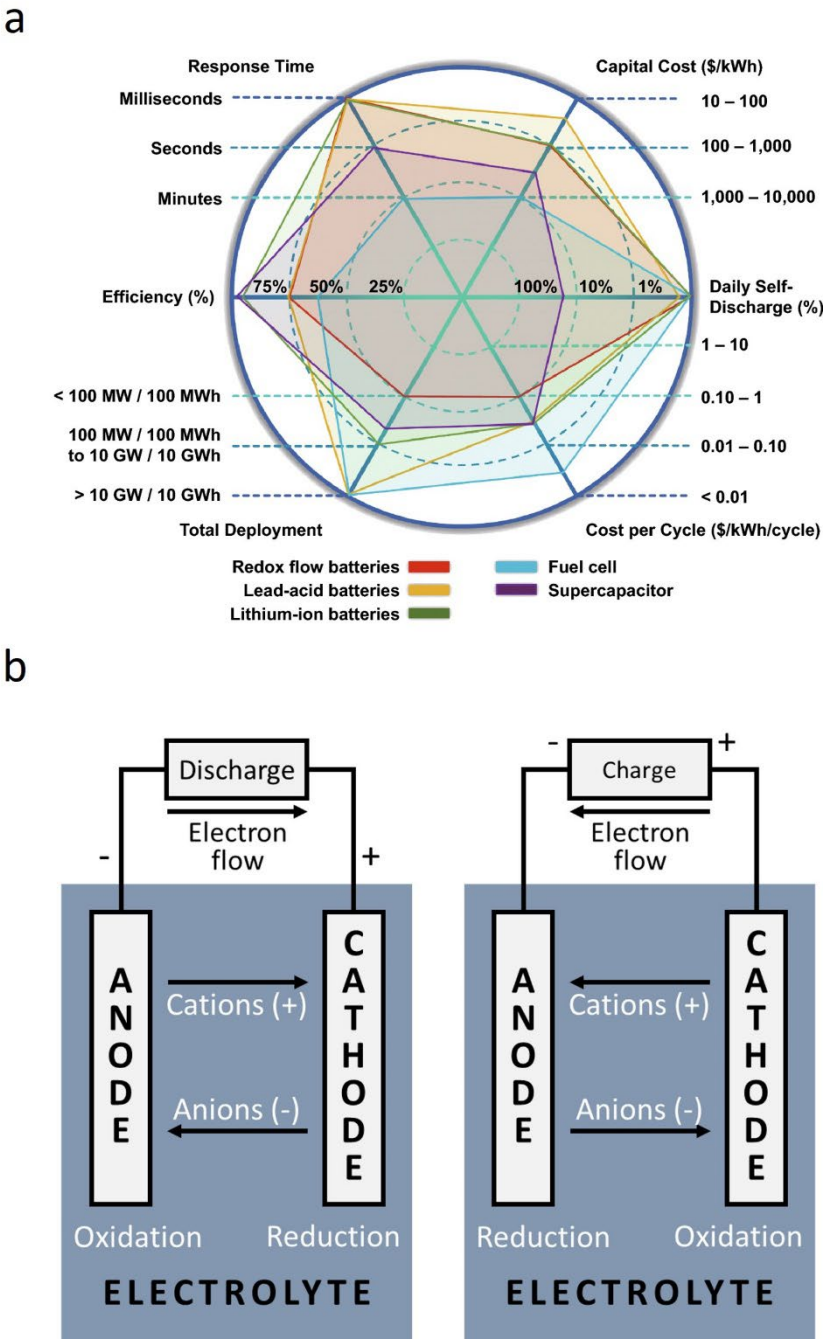


**Figure 1.1** (a) Spider graph representation of critical parameters of the different EESDs. Reproduced with permission.[9] Copyright 2018, Springer Nature. (b) Schematic illustrations of general structures and working mechanisms of EESDs.

Developing high-performance cathodes is essential for next-generation EESDs, because the cathode material is a critical factor in determining the specific capacity, output voltage, rate capability, energy/power density, and efficiencies of EESDs, as well as their calendar life, thermal stability, cost, and environmental impacts.[12,13] On the other hand, there is a huge variety of cathode materials available and under development to satisfy the demands in practical applications, such as large capacity, high voltage, fast charge/discharge, extreme temperature, long service life, *etc*. Unfortunately, cathodes are still one of the bottlenecks in the advancements of EESDs. The challenges faced by cathodes, while diversified with their energy storage mechanisms and materials, have some in general. When pairing with anodes in common EESDs like graphite, Li, Na, and Zn, most cathode materials show apparent disadvantages in terms of specific capacity, electrical conductivity, and cost.[13] Besides, despite being a research goal, high-energy cathodes and their corresponding charging process are highly oxidative, bringing potential risks of corrosion, degradation, and even combustion of other components in EESDs, such as aqueous and organic electrolytes, polymer binder and separator, active anode, metal or carbon current collector, and plastic packaging.[14] Suppressing chemical dissolution, structural collapse and side reactions are also major tasks to improve the reliability.[11] Meanwhile, the complex elemental and phase compositions as well as the hybridized energy storage mechanisms make the in-depth investigations of most cathodes even more difficult.[7] Therefore, it is of great practical significance to study and exploit advanced cathodes for EESDs.

To date, ongoing research has had substantial achievements in cathodes based on different electrochemical energy storage mechanisms, including electric double-layer capacitance (EDLC), pseudocapacitance, bulk ion insertion/desertion, and conversion reactions, which will be introduced in the following sections.

### 1.2 Cathodes based on EDLC

The charge storage mechanism in EDLC is based on the electric double layer at the interface between the electrode and the electrolyte, which is formed when ions with opposite charges in the electrolyte are attracted to the surface of the electrode with an applied voltage.[15] The electrical double layer consists of two regions: the Stern layer, which is a thin layer of ions adsorbed to the surface of the electrode, and the diffuse layer, which is a layer of ions that are loosely bound to the Stern layer (Figure 1.2).[16] The charge storage mechanism in EDLC is fast, reversible, and pure physical process. The capacitance of the EDLC-based electrodes is dependent on the surface area, although the charge storage capability is generally limited without redox reactions. The specific capacitance and capacity can reach ~200 F $g^{-1}$ and ~20 mA h $g^{-1}$, respectively.[15,17]

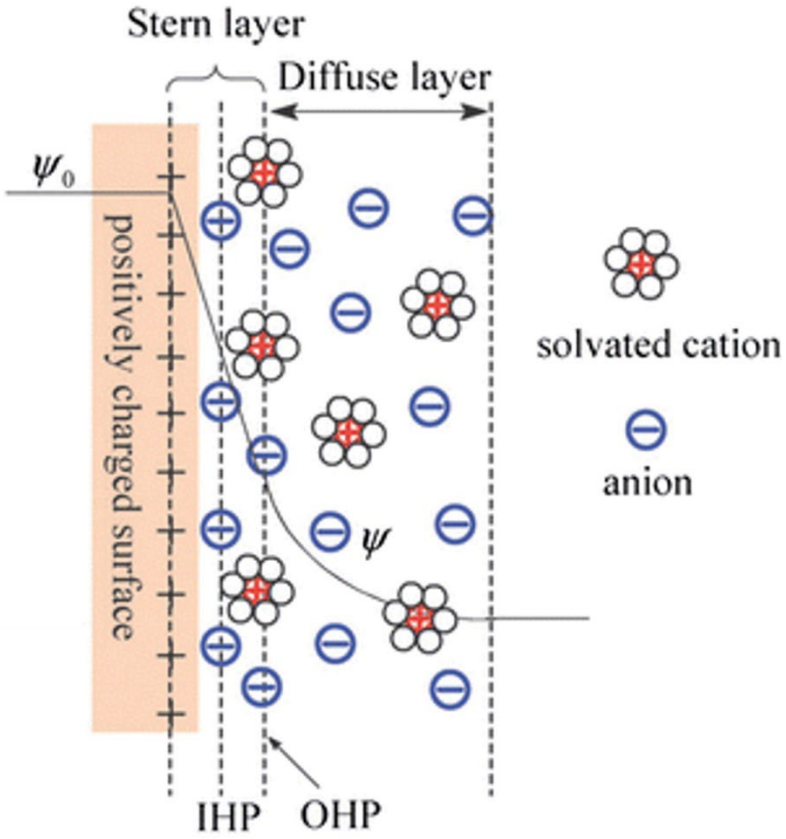


**Figure 1.2** Stern model of the electrical double layer at a positively charged surface, showing the inner Helmholtz plane (IHP) and outer Helmholtz plane (OHP). The IHP refers to the distance of closest approach of specifically adsorbed ions (generally anions) and OHP refers to that of the non-specifically adsorbed ions. The OHP is also the plane where the diffuse layer begins. $\psi_0$ and $\psi$ are the potentials at the electrode surface and the electrode/electrolyte interface, respectively. Reproduced with permission.[16] Copyright 2015, Springer Nature.

The most common cathodes based on EDLC are carbon-based materials with high porosity and surface area.[15] During charging, cations (e.g., $H^+$, $Li^+$, $Na^+$, $Zn^{2+}$) are

desorbed and anions (e.g., $Cl^-$, $SO_4^{2-}$) are adsorbed on the positively charged cathode surface, while the reverse processes occur upon discharge. Porous carbon cathodes, such as activated carbon,[18] carbon nanotubes,[19] graphene aerogels,[20] *etc.*, have been widely reported in symmetric and asymmetric supercapacitors. Recently, by coupling EDLC-type cathodes with battery-type anodes (e.g., Zn), battery-supercapacitor hybrid devices have been developed to incorporate the fast charging/discharging capability of the cathode and the high energy storage capability of the anode.[21] Advancements of EDLC-type cathodes mainly focus on increasing the specific surface area for high capacitance, as well as tuning the porous structures to improve the ion transport. Optimizations on carbonaceous precursors, etching methods, pore template and other synthetic conditions have been extensively explored to obtain high-performance EDLC-type carbon-based cathodes with high surface area and hierarchical porous structures.[15]

### 1.3 Cathodes based on Pseudocapacitance

Pseudocapacitance originates from fast reversible redox reactions at the electrode-electrolyte interface, which is also dependent on the area of interface (active sites).[22] Benefited from the charge transfer of the redox reactions, pseudocapacitance shows a much higher charge storage capability (up to ~200 mA h $g^{-1}$) compared to EDLC despite slightly slower kinetics and inferior stability.[17,23]

Pseudocapacitance can be categorized into three types. The first type, under-potential deposition, describes electrodeposition of a species occurring at a potential below the corresponding theoretical reduction potential, such as the deposition of lead

single-atom films on gold substrates (Figure 1.3a).[24,25] Due to the limited amount of deposition (charge stored), under-potential deposition mechanism is rarely utilized in pseudocapacitance-based cathodes. The second type is the surface redox reactions due to adsorption/desorption of small ions (Figure 1.3b).[24] Ruthenium dioxide ($RuO_2$) cathode in aqueous $H_2SO_4$ electrolyte is a typical example of this mechanism, where $RuO_2$ is protonated and partially reduced ($Ru^{IV}$ to $Ru^{III}$) during discharging, and deprotonated and fully oxidized back to $RuO_2$ during charging.[26] These redox reactions are fast, reversible, and only occur at the surface of $RuO_2$. Other representative cathodes include manganese dioxide ($MnO_2$)[27] and carbon with surface functional groups[28]. Conducting polymers like polyaniline and polypyrrole exhibit pseudocapacitance via the reversible redox reactions of the polymer chain accompanied by the doping/de-doping of counterions, which also fit in this category.[29,30] The third type of pseudocapacitance is contributed by the surface redox reactions due to insertion/desertion of small ions (e.g., $Li^+$), which do not trigger any phase change (Figure 1.3c).[24] Cathodes such as orthorhombic niobium pentoxide (T-$Nb_2O_5$)[31], bronze-phase titanium dioxide [$TiO_2$(B)][32] and 2D layered MXene,[33] are capable of this mechanism because of their channeled or layered crystal structures to allow fast transport and accommodation of $Li^+$ (insertion during discharging and desertion during charging) as well as multivalent transition metal centers to balance the charge. [24]

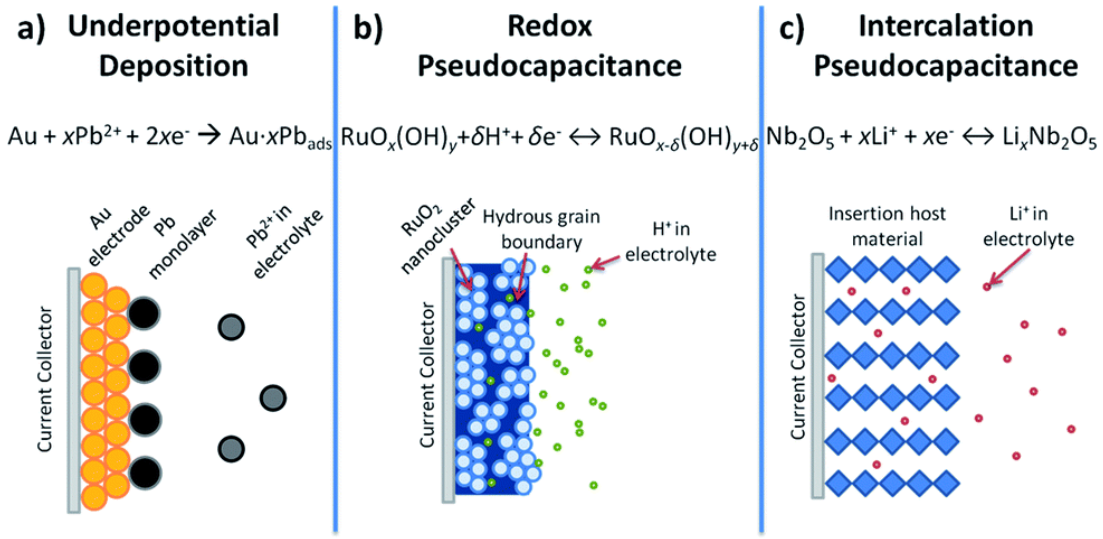


**Figure 1.3** Different types of reversible redox mechanisms that give rise to pseudocapacitance: (a) underpotential deposition, (b) redox pseudocapacitance, and (c) intercalation pseudocapacitance. Reproduced with permission.[24] Copyright 2014, Royal Society of Chemistry.

Notice that some battery-type electrodes with bulk redox reactions can show pseudocapacitive behaviors when the particle size or film thickness is small enough to reach a large surface-to-bulk ratio.[17,34] This size dependence applies to most reported pseudocapacitive electrode materials. Examples include nanosized $LiCoO_2$,[35] transition-metal oxide (e.g., $MoO_2$),[36] transition-metal dichalcogenides (e.g., $MoS_2$),[37] *etc*. Constructing nanostructures, improving conductivity and active site availability, as well as preserving the structural integrity are the most important tasks in developing pseudocapacitance-based cathodes.[17]

### 1.4 Cathodes based on Bulk Ion Insertion/Desertion

Cathodes based on ion insertion/desertion are commonly used in batteries to serve as a host solid for the reversible intercalation of guest species from electrolyte. This type of cathode material consists of a specific type of compound that allows for the reversible insertion of mobile guest species such as atoms, molecules, or ions into a crystalline host lattice.[10] The host lattice structure contains interconnected empty lattice sites of appropriate size (like channels and layers) to accommodate guest species while preserving the host lattice's structural integrity (Figure 1.4).[38] Host materials include metal chalcogenides (e.g., $TiS_2$),[39] metal oxides (e.g., $MnO_2$, $V_2O_5$, $LiMn_2O_4$, $LiCoO_2$),[40-43] polyanion compounds (e.g., $VOPO_4$, $LiFePO_4$),[44,45] 2D layered MXene,[46] Prussian blue analogues,[47] *etc*., while guest species are typically ions (e.g., $Li^+$, $Na^{2+}$, $Zn^{2+}$, $NH^{4+}$, $F^-$).[48]

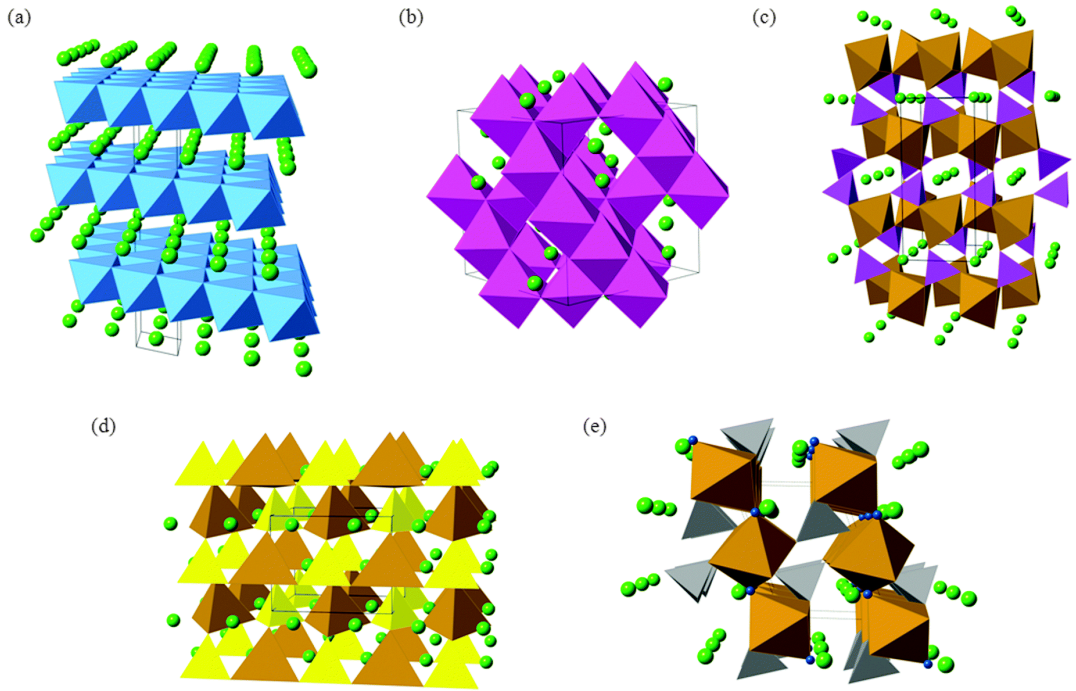

**Figure 1.4** Representative crystal structures of intercalation cathode materials for lithium-ion batteries: (a) layered α-$LiCoO_2$; (b) cubic spinel $LiMn_2O_4$; (c) olivine-structured $LiFePO_4$; (d) $\beta_{II}$-$Li_2FeSiO_4$; and (e) tavorite-type $LiFeSO_4F$. Li ions are shown as light green spheres, $CoO_6$ octahedra in blue; $MnO_6$ octahedra in mauve, Fe-O polyhedra in brown, $PO_4$ tetrahedra in purple, $SiO_4$ tetrahedra in yellow, $SO_4$ tetrahedra in grey, and in (e) fluoride ions in dark blue. Black lines demarcate one unit cell in each structure. Reproduced with permission.[38] Copyright 2014, Royal Society of Chemistry.

Cathodes based on battery-type (bulk) ion insertion/desertion are capable of high potential.[14] With the participation of the active materials in the bulk structure, the ion insertion/desertion also contributes to a higher specific capacity up to ~400 mA h $g^{-1}$,[49] while the rate capability and the structural stability during repetitive charge/discharge are sacrificed compared to the aforementioned pseudocapacitive cathodes.[6] It is also worth noting that the insertion/desertion of ions into/from host lattices of the bulk material leads to various structural changes, such as changes in interlayer spacing, altered stacking modes of the layers, and the formation of intermediate phases, which substantially differs from pseudocapacitive (surface) ion insertion/desertion.[10]

### 1.5 Cathodes based on Conversion Reactions

Conversion reactions depict a huge variety of electrochemical reactions that involve breaking and formation of chemical bonds, which contrast with the ion

insertion/desertion processes (Figure 1.5).[50] Without the need of preserving original phase or host structure, multi-electron transfer can be realized to significantly boost the specific capacity (up to ~2000 mA h $g^{-1}$).[50] Therefore, conversion-type cathodes have the potential of matching the high-capacity anodes like metallic Zn, Li, Na, *etc*., which offer great opportunities for future high-energy-density EESDs. Conversion-type cathodes show a wide range of candidates, including metallic compounds [e.g., $Ni(OH)_2$, $PbO_2$, $FeF_2$, $FeF_3$],[51-54] non-metallic solids (e.g., S, Se, $I_2$),[55-57] liquids and solutions (e.g., $Br_2$, $VO_2^+$),[58,59] and even gas (e.g., $O_2$).[60] Unfortunately, conversion-type cathodes face several challenges, such as poor conductivity, slow kinetics, low reversibility, degradation due to huge structural changes, and unfavorable interactions with electrolyte.[50] Developing the optimization strategies has thus been one of the most important tasks in the research of EESDs.

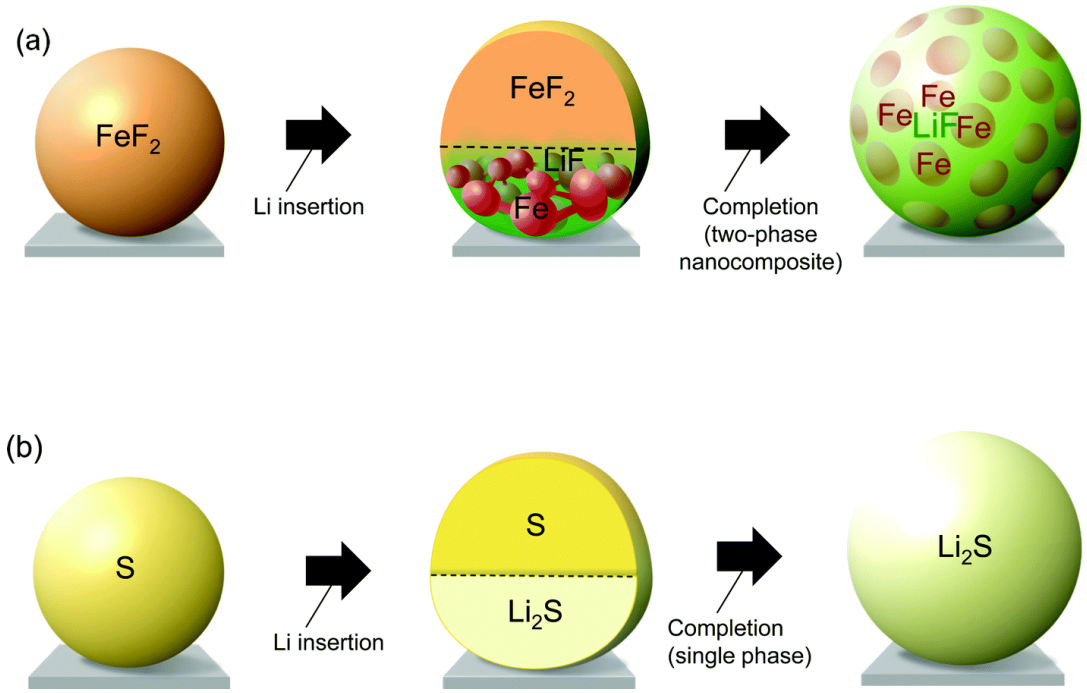

**Figure 1.5** Two types of conversion reactions using lithiation of S and $FeF_2$ as examples: (a) true conversion with the formation of two new phases; (b) chemical transformation with a single new phase formation. Note that each type of cathodes could be produced in both fully lithiated and Li-free states. Reproduced with permission.[50] Copyright 2017, Royal Society of Chemistry.

## References


1. J. P. Holdren. *Science* **2007**, *315*, 737-737.
2. S. Chu, A. Majumdar. *Nature* **2012**, *488*, 294-303.
3. S. Chu, Y. Cui, N. Liu. *Nat. Mater.* **2017**, *16*, 16-22.
4. B. Obama. *Science* **2017**, *355*, 126-129.
5. B. Dunn, H. Kamath, J.-M. Tarascon. *Science* **2011**, *334*, 928-935.
6. M. R. Lukatskaya, B. Dunn, Y. Gogotsi. *Nat. Commun.* **2016**, *7*, 12647.
7. M. R. Palacín. *Chem. Soc. Rev.* **2009**, *38*, 2565-2575.
8. F. Cheng, J. Liang, Z. Tao, J. Chen. *Adv. Mater.* **2011**, *23*, 1695-1715.
9. S. Mukherjee, Z. Ren, G. Singh. *Nano Micro Lett.* **2018**, *10*, 70.
10. Y. Wang, G. Cao. *Adv. Mater.* **2008**, *20*, 2251-2269.
11. P. Canepa, G. Sai Gautam, D. C. Hannah, R. Malik, M. Liu, K. G. Gallagher, K. A. Persson, G. Ceder. *Chem. Rev.* **2017**, *117*, 4287-4341.
12. A. Manthiram. *Nat. Commun.* **2020**, *11*, 1550.
13. N. Nitta, F. Wu, J. T. Lee, G. Yushin. *Mater. Today* **2015**, *18*, 252-264.
14. W. Li, B. Song, A. Manthiram. *Chem. Soc. Rev.* **2017**, *46*, 3006-3059.

15. L. L. Zhang, X. S. Zhao. *Chem. Soc. Rev.* **2009**, *38*, 2520-2531.

16. H. Du, X. Lin, Z. Xu, D. Chu. *J. Mater. Sci.* **2015**, *50*, 5641-5673.

17. C. Choi, D. S. Ashby, D. M. Butts, R. H. DeBlock, Q. Wei, J. Lau, B. Dunn. *Nat. Rev. Mater.* **2020**, *5*, 5-19.

18. M. Yu, D. Lin, H. Feng, Y. Zeng, Y. Tong, X. Lu. *Angew. Chem. Int. Ed.* **2017**, *56*, 5454-5459.

19. D. T. Pham, T. H. Lee, D. H. Luong, F. Yao, A. Ghosh, V. T. Le, T. H. Kim, B. Li, J. Chang, Y. H. Lee. *ACS Nano* **2015**, *9*, 2018-2027.

20. C. Zhu, T. Liu, F. Qian, T. Y.-J. Han, E. B. Duoss, J. D. Kuntz, C. M. Spadaccini, M. A. Worsley, Y. Li. *Nano Lett.* **2016**, *16*, 3448-3456.

21. H. Wang, M. Wang, Y. Tang. *Energy Storage Mater.* **2018**, *13*, 1-7.

22. S. Fleischmann, J. B. Mitchell, R. Wang, C. Zhan, D.-e. Jiang, V. Presser, V. Augustyn. *Chem. Rev.* **2020**, *120*, 6738-6782.

23. T. Liu, Y. Li. *InfoMat* **2020**, *2*, 807-842.

24. V. Augustyn, P. Simon, B. Dunn. *Energy Environ. Sci.* **2014**, *7*, 1597-1614.

25. E. Herrero, L. J. Buller, H. D. Abruña. *Chem. Rev.* **2001**, *101*, 1897-1930.

26. J. P. Zheng, P. J. Cygan, T. R. Jow. *J. Electrochem. Soc.* **1995**, *142*, 2699.

27. T. Zhai, S. Xie, M. Yu, P. Fang, C. Liang, X. Lu, Y. Tong. *Nano Energy* **2014**, *8*, 255-263.

28. H. Zhang, Q. Liu, Y. Fang, C. Teng, X. Liu, P. Fang, Y. Tong, X. Lu. *Adv. Mater.* **2019**, *31*, 1904948.

29. A. M. Bryan, L. M. Santino, Y. Lu, S. Acharya, J. M. D'Arcy. *Chem. Mater.* **2016**, *28*, 5989-5998.

30. T. Liu, L. Finn, M. Yu, H. Wang, T. Zhai, X. Lu, Y. Tong, Y. Li. *Nano Lett.* **2014**, *14*, 2522-2527.

31. V. Augustyn, J. Come, M. A. Lowe, J. W. Kim, P.-L. Taberna, S. H. Tolbert, H. D. Abruña, P. Simon, B. Dunn. *Nat. Mater.* **2013**, *12*, 518-522.

32. M. Zukalová, M. Kalbáč, L. Kavan, I. Exnar, M. Graetzel. *Chem. Mater.* **2005**, *17*, 1248-1255.

33. M. Okubo, A. Sugahara, S. Kajiyama, A. Yamada. *Acc. Chem. Res.* **2018**, *51*, 591-599.

34. P. Simon, Y. Gogotsi, B. Dunn. *Science* **2014**, *343*, 1210-1211.

35. M. Okubo, E. Hosono, J. Kim, M. Enomoto, N. Kojima, T. Kudo, H. Zhou, I. Honma. *J. Am. Chem. Soc.* **2007**, *129*, 7444-7452.

36. H.-S. Kim, J. B. Cook, S. H. Tolbert, B. Dunn. *J. Electrochem. Soc.* **2015**, *162*, A5083.

37. J. B. Cook, H.-S. Kim, T. C. Lin, C.-H. Lai, B. Dunn, S. H. Tolbert. *Adv. Energy Mater.* **2017**, *7*, 1601283.

38. M. S. Islam, C. A. J. Fisher. *Chem. Soc. Rev.* **2014**, *43*, 185-204.

39. M. S. Whittingham. *Science* **1976**, *192*, 1126-1127.

40. W. Sun, F. Wang, S. Hou, C. Yang, X. Fan, Z. Ma, T. Gao, F. Han, R. Hu, M. Zhu, C. Wang. *J. Am. Chem. Soc.* **2017**, *139*, 9775-9778.

41. N. Zhang, Y. Dong, M. Jia, X. Bian, Y. Wang, M. Qiu, J. Xu, Y. Liu, L. Jiao, F. Cheng. *ACS Energy Lett.* **2018**, *3*, 1366-1372.

42. H.-W. Lee, P. Muralidharan, R. Ruffo, C. M. Mari, Y. Cui, D. K. Kim. *Nano Lett.* **2010**, *10*, 3852-3856.

43. K. Mizushima, P. C. Jones, P. J. Wiseman, J. B. Goodenough. *Mater. Res. Bull.* **1980**, *15*, 783-789.

44. F. Wang, W. Sun, Z. Shadike, E. Hu, X. Ji, T. Gao, X.-Q. Yang, K. Xu, C. Wang. *Angew. Chem. Int. Ed.* **2018**, *57*, 11978-11981.

45. A. K. Padhi, K. S. Nanjundaswamy, J. B. Goodenough. *J. Electrochem. Soc.* **1997**, *144*, 1188.

46. B. Anasori, M. R. Lukatskaya, Y. Gogotsi. *Nat. Rev. Mater.* **2017**, *2*, 16098.

47. Y. Li, J. Zhao, Q. Hu, T. Hao, H. Cao, X. Huang, Y. Liu, Y. Zhang, D. Lin, Y. Tang, Y. Cai. *Mater. Today Energy* **2022**, *29*, 101095.

48. G. Wang, M. Yu, X. Feng. *Chem. Soc. Rev.* **2021**, *50*, 2388-2443.

49. W. Xu, Y. Wang. *Nano Micro Lett.* **2019**, *11*, 90.

50. F. Wu, G. Yushin. *Energy Environ. Sci.* **2017**, *10*, 435-459.

51. H. Zhang, R. Wang, D. Lin, Y. Zeng, X. Lu. *ChemNanoMat* **2018**, *4*, 525-536.

52. P. P. Lopes, V. R. Stamenkovic. *Science* **2020**, *369*, 923-924.

53. A. W. Xiao, H. J. Lee, I. Capone, A. Robertson, T.-U. Wi, J. Fawdon, S. Wheeler, H.-W. Lee, N. Grobert, M. Pasta. *Nat. Mater.* **2020**, *19*, 644-654.

54. W. Fu, E. Zhao, Z. Sun, X. Ren, A. Magasinski, G. Yushin. *Adv. Funct. Mater.* **2018**, *28*, 1801711.

55. A. Manthiram, Y. Fu, Y.-S. Su. *Acc. Chem. Res.* **2013**, *46*, 1125-1134.

56. J. Sun, Z. Du, Y. Liu, W. Ai, K. Wang, T. Wang, H. Du, L. Liu, W. Huang. *Adv. Mater.* **2021**, *33*, 2003845.

57. D. Lin, Y. Li. *Adv. Mater.* **2022**, *34*, 2108856.

58. W. Lu, P. Xu, S. Shao, T. Li, H. Zhang, X. Li. *Adv. Funct. Mater.* **2021**, *31*, 2102913.

59. X.-Z. Yuan, C. Song, A. Platt, N. Zhao, H. Wang, H. Li, K. Fatih, D. Jang. *Int. J. Energy Res.* **2019**, *43*, 6599-6638.

60. H.-F. Wang, Q. Xu. *Matter* **2019**, *1*, 565-595.

## Chapter 2 - High-Performance Aqueous Zinc-Ion Hybrid Capacitors based on 3D Printed Metal-Organic Framework Cathodes


### Abstract

The zinc-ion hybrid capacitor is a promising energy storage device, but current overall capacity is limited by the capacitance of the carbon cathode. We produced a hierarchically porous, nitrogen-doped carbon cathode with good cycling and mechanical stability by 3D printing and pyrolysis of the zinc-based metal-organic framework ZIF-8. When incorporated into a zinc-ion hybrid capacitor, we achieved an areal capacitance of 16.9 F $cm^{-2}$ and energy density of 7.23 mW h $cm^{-2}$, outperforming zinc-ion hybrid capacitors based on conventional cathodes.

## 2.1 Introduction

Improved energy storge devices are the cornerstone of sustainable energy infrastructure.[1] While great strides have been made in the production of energy from renewable sources, most of this energy comes from intermittent wind and solar sources which cannot deliver uninterrupted power. Energy storage devices are needed for power supply when it is dark, cloudy, or calm[2] and are increasingly in demand for electronic consumer goods.[3] Hybrid capacitors are energy storage devices that contain a battery-like anode that stores charge in the bulk phase as well as a capacitor-like cathode that stores charge on a surface.[4] They therefore combine the high energy density of batteries with the high power density and long cycle lifetime of electric double layer supercapacitors.[5] Aqueous zinc-ion hybrid capacitors (ZIHC) are appropriate for the clean energy transition since they rely on an abundant, non-toxic metal and avoid the hazards of organic electrolyte solvents.[6]

Currently, the overall capacity of hybrid capacitors is limited by the carbon cathode.[7] Several varieties of carbon have been investigated recently for suitability in ZIHCs, such as natural sources, activated carbon,[8] graphene,[9] and zeolite templates.[10] The challenge remains to produce carbon cathodes with higher surface area and ion affinity to raise the upper limit of ion capacity. More ordered porosity within the cathode is also needed to facilitate ion diffusion.[11] Given this breadth of requirements, we sought a more versatile source of carbon than those tested thus far.

We chose metal-organic frameworks (MOFs) as a diverse category of materials to template a carbon cathode specifically designed to absorb zinc ions. The high surface

area, chemical tunability, ordered porosity, and the inherent presence of metal ions in MOFs[12] could simultaneously solve several of the current limitations of carbon cathodes for ZIHCs. Although most MOFs are electrical insulators, it has been shown that pyrolysis of certain MOFs, including ZIF-8, converts them to an electrically conductive graphitic structure that retains the porosity of the MOF template.[13-15]

We produced cathodes specially tailored to zinc ion insertion by additive manufacturing and pyrolysis of a zinc-based metal-organic framework (Figure 2.1). When incorporated into a ZIHC, this cathode yielded an exceptionally high areal capacitance of 16.9 F $cm^{-2}$ at a current density of 5 mA $cm^{-2}$. The MOF we chose, a zeolitic imidazolate framework known as ZIF-8, is practical for large-scale applications given its commercial availability,[16] low cost,[17] and water stability.[18] The outstanding capacitance is likely attributed to the ion capacity imparted by the ZIF-8 template. ZIF-8 is an exceptional broad-spectrum adsorbent due to its ultrahigh surface area of 1,947 $m^2$ $g^{-1}$ and micropores of 11.6 Å diameter.[19] Additionally, ZIF-8's wealth of Zn-N bonds, in the form of zinc ions coordinated by imidazolate ligands, serve as a template of ion adsorption sites. Chemical adsorption sites for ions present in the cathode may increase energy storage capacity by charge transfer-based pseudocapacitance.[20,21] Finally, the 3D printed architecture creates hierarchical porosity that allows a thick electrode (0.3 cm) to remain electrochemically active and accessible to ions throughout its depth.[22]

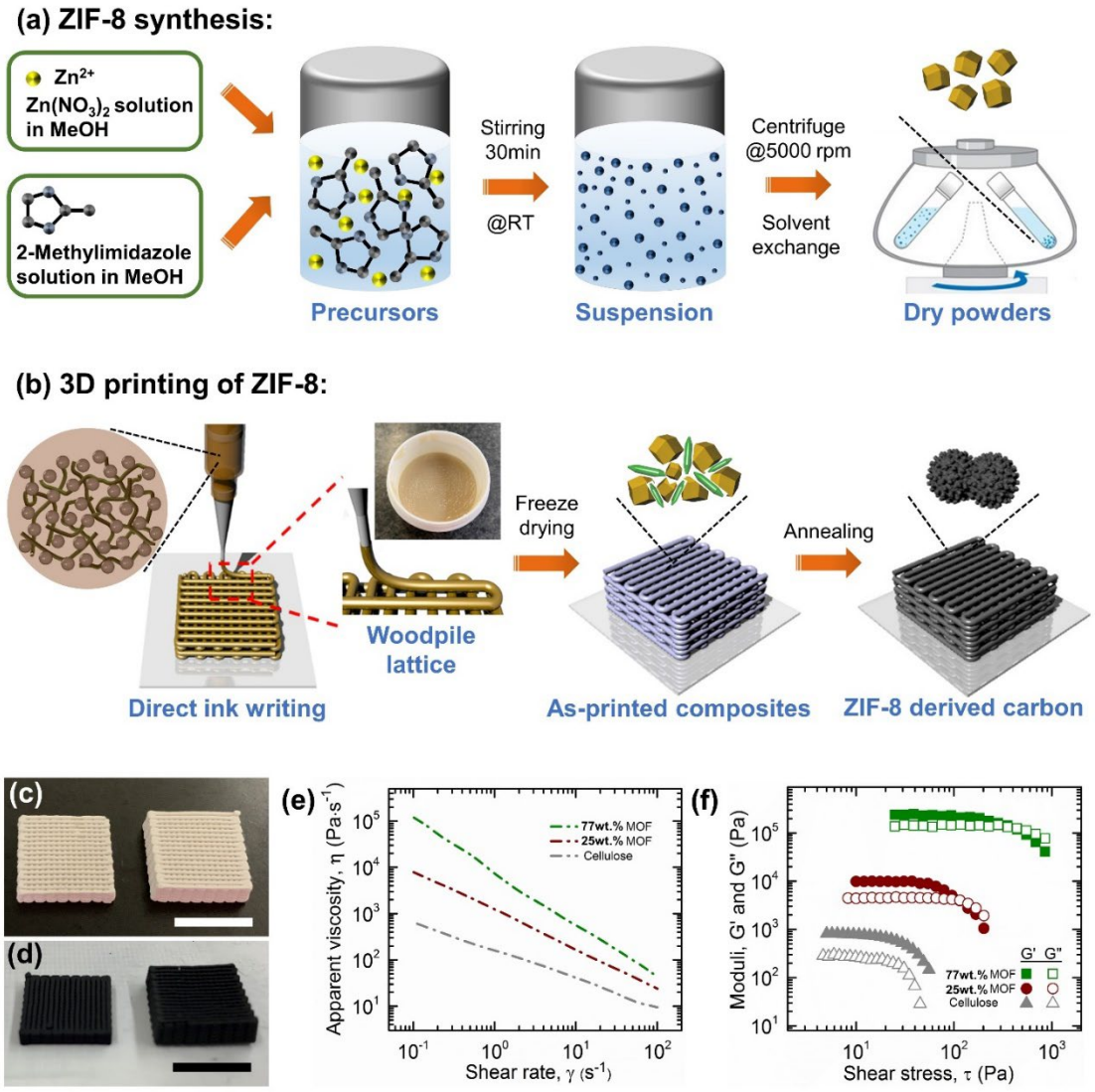


**Figure 2.1** Schematic of (a) ZIF-8 powder synthesis process and (b) 3D printing process of ZIF-8 ink. Optical images of (c) 3D printed ZIF-8 lattices and (d) pyrolyzed ZIF-8 lattices, scale bars are 1 cm. Rheology of ZIF-8 ink with varying formulations: (e) apparent viscosity as a function of shear rates and (f) elastic modulus and loss modulus as a function of shear stress.

## 2.2 Experimental Section

### ZIF-8 Synthesis and Activation

ZIF-8 was synthesized and activated following a modified version of a previously reported procedure for the formation of ZIF-8 nanocrystals (Figure 2.1a).[23] Typically, 2.93 g (9.85 mmol) of zinc nitrate hexahydrate were dissolved in 200 mL of methanol. Separately, 6.49 g (79.0 mmol) of 2-methlyimidazole were dissolved in 200 mL of methanol. The zinc nitrate solution was rapidly poured into the 2-methylimidazole solution. The resulting combined solution was stirred for 30 min at room temperature. The transparent, colorless solution slowly turned opaque white. To isolate and activate the nanocrystals, the mixture was centrifuged at 5,000 rpm for 10 min. The methanol was decanted and replaced with fresh methanol. The centrifugation followed by methanol replacement was repeated twice per day for three days. After the final decantation, the nanocrystals were allowed to dry in air. The resulting fine white powder was then dried under dynamic vacuum for 5 h at room temperature followed by 5 h at 300 °C reaching an ultimate vacuum of <5 μmHg. A final amount of 0.915 g of pure, dry product was isolated corresponding to a 41.1% yield.

### Ink Formulation

Typically, 0.65 g of cellulose nanocrystalline powders were dispersed in 4.0 g of deionized water to form a suspension. Then, 2.2 g of ZIF-8 were added to this suspension. The composites were homogenized in a planetary centrifugal speed mixer

(ARE-250, Thinky) at 2,200 rpm for 2 min. The homogenization step was repeated twice.

**3D Printing**

The 3D printing process is illustrated in Figure 2.1(b). The inks were loaded into 10 mL syringes (Nordson EFD) attached by a Luer-Lok to a smooth-flow tapered conical nozzle of 600 μm inner diameter (ø). An air-powered fluid dispenser (Ultimus V, Nordson EFD) provided the appropriate pressure to extrude the ink through the nozzle. The target patterns were printed using a three-axis positioning stage (ABL9000, Aerotech) onto a hydrophobized silicon wafer and extruded under pressures of 40 psi at a speed of 10 mm $s^{-1}$. The printed parts were freeze dried for 24 h to obtain the 3D printed ZIF-8 lattices (Figure 2.1c).

**Ink Rheology Characterization**

Viscoelastic properties of the ink were measured using a stress-controlled rheometer (AR 2000ex, TA Instruments) with a 40 mm flat-plate geometry and a gap of 500 μm in the presence of solvent trap to avoid solvent evaporation. A strain sweep from 0.1 to 100 $s^{-1}$ was first performed to record the $\eta$ as a function of varying $\gamma$. A stress sweep from $10^{-2}$ to $10^{3}$ Pa at a constant frequency of 1 Hz was also conducted to record the G' and G" as a function of sweep stress. The $\tau_y$ is defined as the stress at which G' fell to 90% of the plateau value. The G' creep data was recorded after applying a pre-shear at 100 $s^{-1}$ for 1 min as a function of time from 0.1-10 min to evaluate the structural recovery of the ink after deposition during 3D printing.

**Pyrolysis**

Freeze-dried 3D printed ZIF-8 lattices were placed in crucibles in a 1 in. tube furnace and pyrolyzed to maximum temperatures of 400, 800, 1,000, 1,200, and 1,400 °C under $N_2$ or Ar at a flow rate of 50 sccm. After reaching the maximum temperature, the samples were allowed to cool to room temperature within the furnace. The lattices heated to maximum temperatures of 400 and 800 °C were heated at a rate of 5 °C $min^{-1}$ from room temperature and then held at maximum temperature for 2 h followed by cooling to room temperature within the furnace. The lattices heated to a maximum temperature of 1,000 °C were heated at a rate of 5 °C $min^{-1}$. They were held at 200 °C for 1 h, then at 600 °C for 1 h, then at 1,000 °C for 2 h. The lattices heated to maximum temperatures of 1,200 or 1,400 °C reached 1,000 °C following the same procedure. They were then heated at 2.5 °C $min^{-1}$ to reach the target maximum temperature and held at maximum temperature for 2 h. A cooling rate of 5 °C/min was then used to reach 1,000 °C followed by cooling naturally to room temperature within the furnace to obtain the pyrolyzed 3D ZIF-8 lattices (Figure 2.1d).

**Porosity Characterization**

Brunauer-Emmett-Teller (BET) surface areas and pore size distribution were calculated from $N_2$ gas sorption isotherms measured on a volumetric analyzer (ASAP 2020, Micromeritics Instrument Corp.). Liquid $N_2$ was used as a bath to achieve cryogenic temperature of 77 K. Ultrahigh purity $N_2$ (99.999%) was used as the adsorption gas. Ultrahigh purity He (99.999%) was used to calculate the free space of the measurement cell. Immediately prior to sorption experiments, 200 mg of sample

was activated by drying in the measurement cell on the degas port of the adsorption analyzer. The sample was placed under dynamic vacuum for 5 h at room temperature followed by 5 h at 300 °C reaching an ultimate vacuum of <5 μmHg. The $N_2$ adsorption isotherm was collected at 77 K in the pressure range of 0.001 to 1 bar.

The total BET surface area was calculated by first determining the linear fit of data points in the pressure range of $10^{-7}$ to $10^{-5}$ bar plotted as relative pressure ($P/P_0$) vs. 1/[Quantity adsorbed ($m^3\ g^{-1}$) · Inverse relative pressure ($P_0/P$)-1]. The monolayer volume ($m^3\ g^{-1}$) was then calculated as the inverse of the sum of the slope and intercept. Finally, the total BET surface area ($m^2\ g^{-1}$) was calculated as the product of the monolayer volume ($m^3\ g^{-1}$), Avogadro's constant ($mol^{-1}$) and the $N_2$ cross sectional area ($m^2$) divided by the molar volume of an ideal gas ($m^3\ mol^{-1}$). The pore size distribution of the ZIF-8 lattice pyrolyzed at 1,000 °C was estimated based on the density functional theory slit pore model within the MicroActive software (Micromeritics Instrument Corp.).

**X-Ray Diffraction**

Powder X-ray diffraction patterns were collected on Bruker D8 Advance diffractometer using Cu $K_\alpha$ X-rays of 1.5405 Å within a range of $5° \leq 2\theta \leq 40°$ with a step size of 0.02° and a counting time of 5 s/step. 3D printed lattices were ground in a mortar and pestle prior to measurement. The simulated pattern was generated in the software Mercury from the atomic coordinates of ZIF-8 contained in the crystallographic information file.

**Thermostability Characterization**

The dimensions of the typical 3D printed sample were 1.5 × 1.5 × 0.1-0.3 $cm^3$. The dimensions of the 3D printed lattices were measured with a caliper with an accuracy of 0.01 mm. The linear shrinkage was calculated from longitudinal dimensions determined before and after the freeze drying and pyrolysis steps. The weight was determined with an ultra-micro balance (XP204, Mettler Toledo) with an accuracy of 0.001 mg. The geometric density is calculated from the measured mass and volume of each specimen. The uniaxial compression of the 3D printed lattice was measured under quasi-static condition with an Instron 6800 Series dual column table model testing system fitted with a 1,000 N load cell operating at a compression rate of 5 μm $s^{-1}$. The yield strength (σ*) is calculated by the 0.2% offset method with the proof stress corresponding to a permanent plastic strain of 0.2%. The Young's modulus was calculated based on the initial linear slope of the stress-strain curve. Thermogravimetric analysis (TGA) was performed on a TA Instruments Discovery 5500 with a precision of ±0.001 mg. A sample of 10 mg was loaded into an alumina ceramic pan, heated at 5 °C $min^{-1}$ from room temperature to 1,000 °C and at 10 °C $min^{-1}$ to 1,200 °C under a constant flow of $N_2$.

**Imaging and Spectroscopy**

The morphology of the 3D printed lattice was observed by optical camera and field-emission SEM and TEM. Real-time videos of the 3D printing process were obtained by a CCD camera (Thorlabs). EDS was performed on both SEM and TEM instruments. SEM was performed on a Thermo Fisher Scientific Helios G4 PFIB at an

acceleration voltage of 5 kV and a current of 0.2-3 nA in secondary electron imaging mode with a working distance of 3-5 mm. EDS was performed on a Thermo Fisher Scientific Pathfinder equipped with a drifted silicon detector using an acceleration voltage of 3 kV, a current of 0.8 nA, and a working distance of 5 mm generating 4,000 counts per second. TEM specimens were prepared by first crushing the 3D printed lattices into powders with a mortar and pestle. The powders were then suspended in deionized water and ultrasonicated for 5 min before drop casting directly onto TEM grids with an amorphous carbon membrane. TEM characterizations were conducted using a Thermo Fisher Scientific Titan 80-300 (S)TEM operated at 300 kV. EDS was performed with a Super-X G2 detector. EELS was performed with a Gatan GIF Quantum spectrometer. Elemental maps were obtained with both EDS and EELS in STEM mode. Spectral image pixel time was kept below 0.05 s to minimize electron beam damage. XPS was performed on a PHI Quantum 2000 Scanning ESCA Microprobe using Al $K_\alpha$ X-rays of 1486.6 eV. The analysis area was 200 mm. The Zn $2p_{3/2}$ binding energy referenced to 1022.0 eV.

**Electrochemical Characterizations**

All electrochemical tests, including the single-electrode characterizations in three-electrode systems and ZIHC device tests in two-electrode systems, were performed in a 50 mL beaker cell (Figure 2.2). The 3D carbon samples ($0.5 \times 0.5$ $cm^2$) were wrapped in a piece of Ti gauze, and the extension of the Ti gauze was held by a Pt electrode holder. A vacuum degas process was then conducted in 2 M $ZnSO_4$ aqueous solution to enhance the electrolyte infiltration into the carbon structure. A

piece of Zn foil (1.0 × 1.0 $cm^{-2}$) was also held by a Pt electrode as counter electrode (three-electrode system) or anode (ZIHC device). 30 mL 2 M $ZnSO_4$ aqueous solution was added as electrolyte. Saturated calomel electrode (SCE) was used as reference electrode in the three-electrode system. The electrochemical tests were conducted using a BioLogic EC-Lab SP-300 electrochemical workstation.

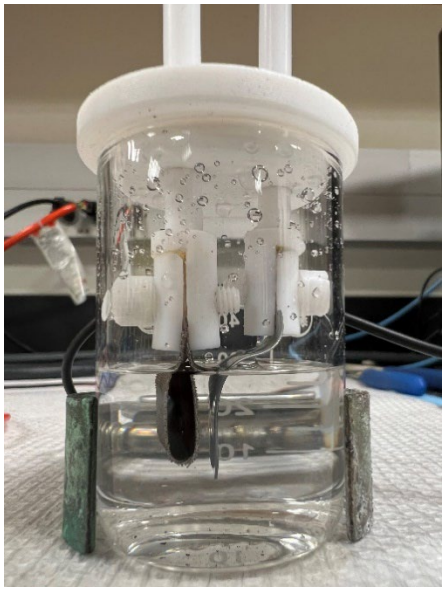

**Figure 2.2** Photograph of electrochemical test cell in a 50 mL breaker.

**Calculations**

The areal capacitance ($C_A$) of the single electrode was calculated based on the CV curves using Equation 2.1.

$$C_A = \frac{S}{2 \times \Delta U \times v \times A} \tag{2.1}$$

where $C_A$ is the areal capacitance (F $cm^{-2}$), $S$ is the integrated area of the CV curve, $\Delta U$ is the potential window (V), $v$ is the scan rate (V $s^{-1}$), and $A$ is the geometric electrode working area ($cm^2$).

The areal capacity ($Q_A$) of the of the ZIHC device was calculated based on the galvanostatic charging and discharging tests using Equation 2.2.

$$Q_A = \frac{Q_{dis}}{A} \tag{2.2}$$

where $Q_A$ is the areal capacity (mA h $cm^{-2}$), $Q_{dis}$ is the discharging capacity (mA h) obtained from the galvanostatic discharging voltage profile of the single electrode, $A$ is the geometric electrode working area ($cm^2$).

The areal capacitance ($C_A$), gravimetric capacitance ($C_G$) and volumetric capacitance ($C_V$) of the ZIHC device were calculated based on the galvanostatic charging and discharging tests using Equations 2.3, 2.4 and 2.5, respectively.

$$C_A = \frac{3600 \times Q_{dis}}{1000 \times \Delta U \times A} \tag{2.3}$$

$$C_G = \frac{3600 \times Q_{dis}}{1000 \times \Delta U \times M} \tag{2.4}$$

$$C_V = \frac{3600 \times Q_{dis}}{1000 \times \Delta U \times V} \tag{2.5}$$

where $C_A$, $C_G$, and $C_V$ are the areal, gravimetric, and volumetric capacitances (F $cm^{-2}$, F $g^{-1}$, and F $cm^{-3}$, respectively), $Q_{dis}$ is the discharging capacity (mA h) obtained from the galvanostatic discharging voltage profiles of the device, $\Delta U$ is the potential window (V) excluding the $iR$ drop, $A$ is the geometric working area of the 3D

carbon electrode ($cm^2$), $M$ is the mass of the 3D carbon electrode (g), and $V$ is the volume of the 3D carbon electrode ($cm^3$).

The areal energy density ($E_A$, mW h $cm^{-2}$) and power density ($P_A$, mW $cm^{-2}$) of the ZIHC device were calculated using the following equations:

$$E_A = \frac{Q_{dis} \times \Delta U}{2A} \tag{2.6}$$

$$P_A = \frac{3600 \times E_A}{t_{dis}} \tag{2.7}$$

where $Q_{dis}$ is the discharging capacity (mA h) obtained from the galvanostatic discharging voltage profiles of the device, $\Delta U$ is the potential window (V) excluding the $iR$ drop, $t_{dis}$ is the discharging time (s) in the galvanostatic discharging test, and $A$ is the geometric working area of the 3D carbon electrode ($cm^2$).

**Trasatti Capacitance Contribution Analysis**

The areal capacities ($C_{A,CV}$) at different scan rates were calculated from cyclic voltammetry (CV) curves using Equation 2.8.

$$C_{A,CV} = \frac{S_{CV}}{2vU} \tag{2.8}$$

where ($C_{A,CV}$) is the areal capacitance (mF $cm^{-2}$), $S_{CV}$ is the mathematical integrated area of the CV curve (mA V $cm^{-2}$), $v$ is the scan rate (V $s^{-1}$), and $U$ is the voltage window of the CV test (V). With the assumption of semi-finite ion diffusion, a linear relation of $C_{A,CV}$ vs. $v^{-1/2}$ can be observed at slow scan rates (1-5 mV $s^{-1}$). Due to the intrinsic electrical resistance of the electrode, the capacitances obtained at high scan rates were deviated from the linearity, and thus excluded from the linear fitting. The extrapolation

of the fitting line yields a y-intercept ($v \rightarrow +\infty$) that represents the kinetically fast $C_{capacitive}$ contributed by the surface capacitive-controlled process, because capacitance with relatively sluggish kinetics ($C_{diffusion}$), which is controlled by ion diffusion behaviors, doesn't show effect when $v \rightarrow +\infty$. Since $C_{A,CV}$ at each scan rate can be decoupled with $C_{capacitive}$ and $C_{diffusion}$, the portion of capacitance contribution from both $C_{capacitive}$ can thus be calculated.

## 2.3 Results and discussion

### Ink Formulation

We formulated an ink consisting of 77 wt.% ZIF-8 that we printed by direct ink writing with a 600 μm nozzle. The prerequisite for this fabrication strategy was to develop a printable ink with self-supporting features.[24] However, agglomeration of MOF particles often prevents high mass loading, and recent attempts to achieve printability have relied on the addition of excessive amounts of binders.[25-28] Here, we innovate an aqueous-based, highly concentrated zinc MOF (ZIF-8) ink with minimal additives. Our ink formulation was composed of nanocrystals of both ZIF-8 and cellulose in water. The cellulose served as a binder and gelation agent in which a hydrogel is formed by hydrogen bonding of the cellulose hydroxyl groups.[29] Additionally, discrete cellulose nanocrystals work as a surfactant to assist de-agglomeration of ZIF-8 crystals.[30] Unlike other polymer binders, cellulose in the form of nanocrystals is anisotropic and does not have physical entanglements, so it accommodates a greater quantity of solid material at a lower viscosity.[31] The cellulose

acts as a humectant to prevent solid-liquid phase separation and drying-induced jamming and cracking during printing. In addition, the nanocellulose has a high Young's Modulus of 150 GPa, which helps maintain structural integrity.[32]

Appropriate rheology is a crucial aspect of ink development. The ink must flow smoothly through the nozzle without clogging and set immediately to maintain shape.[33] Shear thinning facilitates reliable flow while viscoelasticity provides rapid recovery of a solid-like phase after printing to maintain filamentary shape and self-support printed features against gravity.[34] Apparent viscosities ($\eta$) of the ZIF-8 inks decrease as the shear rates ($\gamma$) increase to those applied during extrusion flow (0.1 to 100 $s^{-1}$, Figure 2.1e). The onset of shear thinning is observed in pure cellulose nanocrystal suspensions. Upon increasing the ZIF-8 loading from 25 to 77 wt.%, the viscosity of the ink approaches extremely high values at low shear rates (>$10^5$ Pa s at 0.1 $s^{-1}$). These results indicate that the ink behaves like a solid at low shear rates or at rest, which is further supported by the oscillatory frequency sweep results.

To evaluate the viscoelastic properties, the shear stress ($\tau$) as a function of storage (G') and loss (G") moduli were measured (Figure 2.1f). Although the ZIF-8 and cellulose are held together by weak interactions at rest, these interactions are overcome when the applied shear exceeds the yield stress ($\tau_y$). At this point, the ink flows and adopts shear-thinning behavior. The yield stress point can be estimated from the oscillatory stress sweep curve, where the storage modulus drops to 90% of the plateau value. The cellulose nanocrystal suspension without ZIF-8 has a short linear viscoelastic region with a storage modulus plateau below $10^3$ Pa and a yield stress of

only 20 Pa. The loss modulus is always lower than storage modulus indicating a more liquid like behavior after yielding. We investigated the printability of the inks at various ZIF-8 loadings. When ZIF-8 is added at 25 wt.%, the storage modulus and yield stress increase by approximately an order of magnitude to $10^4$ Pa and 80 Pa, respectively, indicating the ink's ability to sustain higher yield stress without losing homogeneity. At a loading of 77 wt.% ZIF-8, the storage modulus is close to the loss modulus at $2\times10^5$ Pa, and the yield stress is 200 Pa. These data suggest good phase stability compared to dilute inks. The higher mass loading increases viscosity and internal stress to enhance the printability and maintain cohesion of the printed structure without the need for rheology modifiers. The mass fraction of the ZIF-8 powder should be higher than 50 wt.% to minimize shrinkage. However, ZIF-8 inks with too high of a solid loading (> 77 wt.%) become dilatant and non-extrudable due to high yield stress during flow. The magnitudes of these key rheological parameters are in good agreement with those reported for other colloidal inks designed for this 3D filamentary printing technique.[35]

**3D Printing**

The ZIF-8 ink was loaded into a syringe barrel affixed to a 600 μm nozzle and deposited in a layer-by-layer manner following a pre-defined tool path. After deposition, the nanocellulose fibers adhere ZIF-8 crystals together and enable the ink's fast transition from extrusion flow to dilatant hardening for better shape retention. We printed 3D cuboid lattices by depositing multiple orthogonal layers of parallel filaments successively (Figures 2.1b and 2.3a). These woodpile lattice structures are designed

with a center-to-center filament spacing (L) of 1,200 μm and a filament diameter (d) of around 600 μm, resulting in a spacing-to-diameter ratio (L/d) of 2 as well as a layer height (Δz) of 360 μm (0.6 d). The printed layers are well-bonded to one another. By simply changing the number of printed layers, we can print lattices with varying thickness over a wide range. Their height increases linearly with layer number while their width is nearly constant. After printing, the lattices were solidified by freeze drying for 24 h to remove residual water from the aqueous ink.

The resulting dried lattice consists of ZIF-8 crystals embedded in a nanocellulose network. The characteristic cubic and rhombic dodecahedral crystals of ZIF-8 are visible as the predominant component and are homogeneously distributed (Figure 2.3a). The crystals retain a regular structure with sharp facets 250 μm in length suggesting the ink formulation and 3D printing process retains the ZIF-8 crystals intact as a template for subsequent modification. The X-ray diffraction pattern of the 3D printed lattice matches that of pure ZIF-8 and confirms the ZIF-8 crystal structure was maintained (Figure 2.4a). Based on X-ray photoelectron spectroscopy (XPS) of N 1*s* electrons (Figure 2.5), the 3D printed ZIF-8 lattice consists of two types of nitrogen: pyrrole (400 eV)[36] and Zn-N (397 eV)[37]. These results indicate that the 2-methylimidazole linkers and their coordination to the zinc ions persist and that the ZIF-8 molecular structure is retained in the 3D printed architecture. The preservation of the ZIF-8 crystal structure allows it to serve as a template to obtain other microporous products after further processing steps, such as pyrolysis to impart an electrical conductivity.

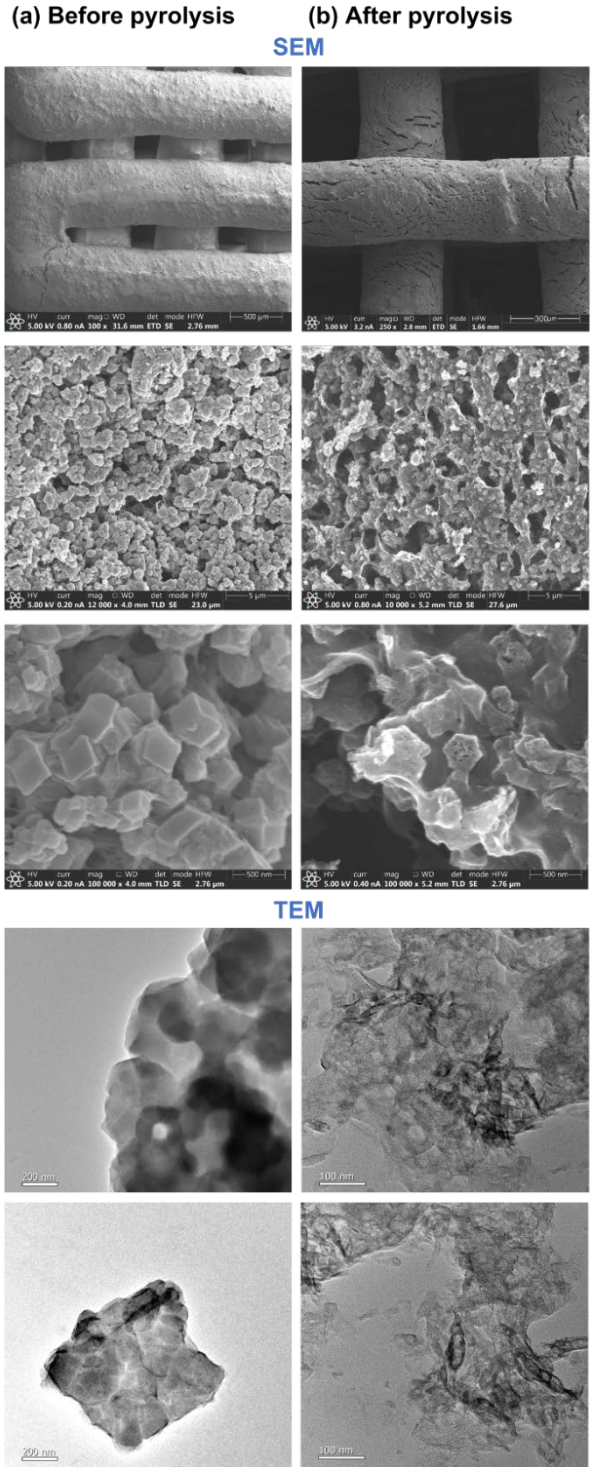


**Figure 2.3** Electron microscope images of 3D printed ZIF-8 lattices (a) before pyrolysis and (b) after pyrolysis at 1,000 °C.

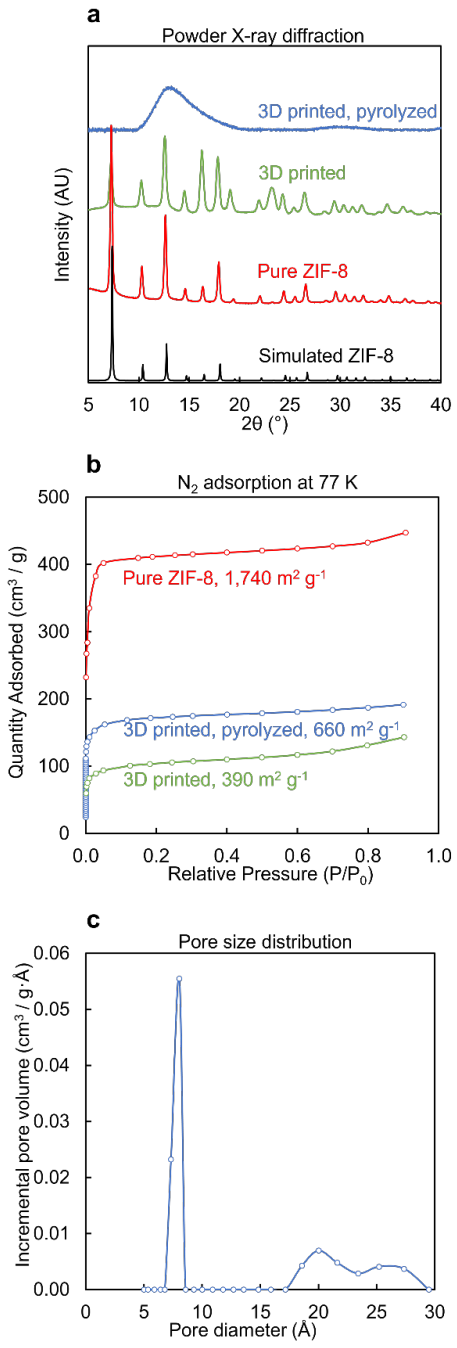


**Figure 2.4** Porosity characteristics of ZIF-8 (red), 3D printed ZIF-8 lattice (green), and pyrolyzed ZIF-8 lattice (blue). (a) Powder X-ray diffraction. (b) $N_2$ adsorption (filled

circles) and desorption (hollow circles) isotherms at 77 K. (c) Pore size distribution of 3D printed ZIF-8 lattice after pyrolysis at 1,000 °C based on DFT slit pore model.

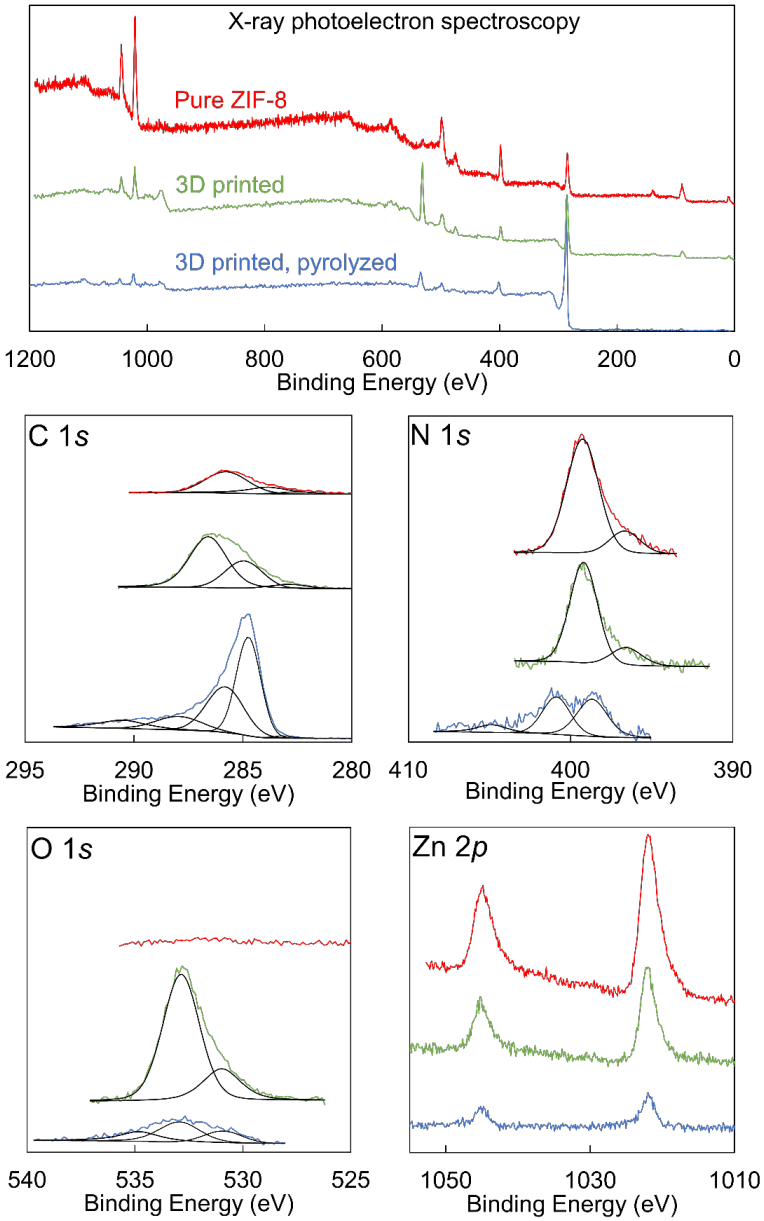


**Figure 2.5** X-ray photoelectron spectroscopy of ZIF-8 (red), 3D printed ZIF-8 lattice (green), and pyrolyzed ZIF-8 lattice (blue).

**Pyrolysis to Induce Electrical Conductivity**

To overcome the insulating nature of the ZIF-8, the 3D printed lattice was pyrolyzed to induce partial conversion to a graphitic molecular structure. Although some electrically conductive metal-organic frameworks have been reported,[38] the vast majority are electrically insulating which precludes their incorporation into electrochemical devices. We investigated pyrolysis temperatures from 800 to 1,400 °C in an inert atmosphere. Pyrolysis at 1,000 °C provided the best electrochemical performance based on the extremely high areal capacitance. We compared the effects of pyrolysis temperature on electrical conductivity, porosity, and retention of zinc and nitrogen. We found that pyrolysis at 800 °C corresponded to lower surface area than pyrolysis at 1,000 °C. Pyrolysis at 1,200 or 1,400 °C yielded similar surface area to 1,000 °C but with broader pore size distributions and less retention of nitrogen and zinc (Table 2.1).

**Table 2.1** Effect of pyrolysis on elemental composition and porosity of 3D printed ZIF-8 lattices. Elemental compositions are reported as atomic percent from energy dispersive X-ray spectra (EDS). Surface area is calculated from the Brunauer-Emmett-Teller (BET) equation[39] based on the $N_2$ adsorption isotherm measured at 77 K.

| | Before pyrolysis | 800 °C | 1,000 °C | 1,200 °C | 1,400 °C |
|---|---|---|---|---|---|
| Carbon | 67% | 71% | 83% | 90% | 94% |
| Oxygen | 12% | 10% | 10% | 8% | 5% |
| Zinc | 10% | 10% | 5% | 0% | 0% |
| Nitrogen | 11% | 9% | 2% | 2% | 1% |
| Surface Area | 392 $m^2$ $g^{-1}$ | 220 $m^2$ $g^{-1}$ | 660 $m^2$ $g^{-1}$ | 660 $m^2$ $g^{-1}$ | 605 $m^2$ $g^{-1}$ |
| Pore Diameter | 11 Å | 11, 15-17 Å | 7.5, 20-25 Å | 7.5, 12-15, 30 Å | 7, 8.5, 10-15, 30 Å |

The 3D architecture was well-preserved after pyrolysis (Figure 2.4d). Due to the high mass loading of ZIF-8, the 3D printed lattice shrinks by less than 10% linearly after heat treatment. Thermal gravimetric analysis (TGA) reveals two decomposition steps with the second beginning at 600 °C corresponding to the thermal conversion of ZIF-8 (Figure 2.6a). The polyhedral morphology of ZIF-8 persists in the pyrolyzed product. We determined the microstructure by imaging the 3D printed lattices with scanning electron microscopy (SEM) followed by grinding them and imaging the resulting small particles by transmission electron microscopy (TEM). Cubic and rhombic dodecahedral particles of 250 μm dimensions are homogeneously distributed throughout the lattice and encapsulated by thin sheets (Figure 2.3b). In contrast to the particle appearance prior to pyrolysis, the pyrolyzed particles contain mesopores that are visible at 100,000x magnification. Mesopores are also evident in the pore size distribution (Figure 2.4c) calculated from the $N_2$ adsorption isotherm (Figure 2.4b).

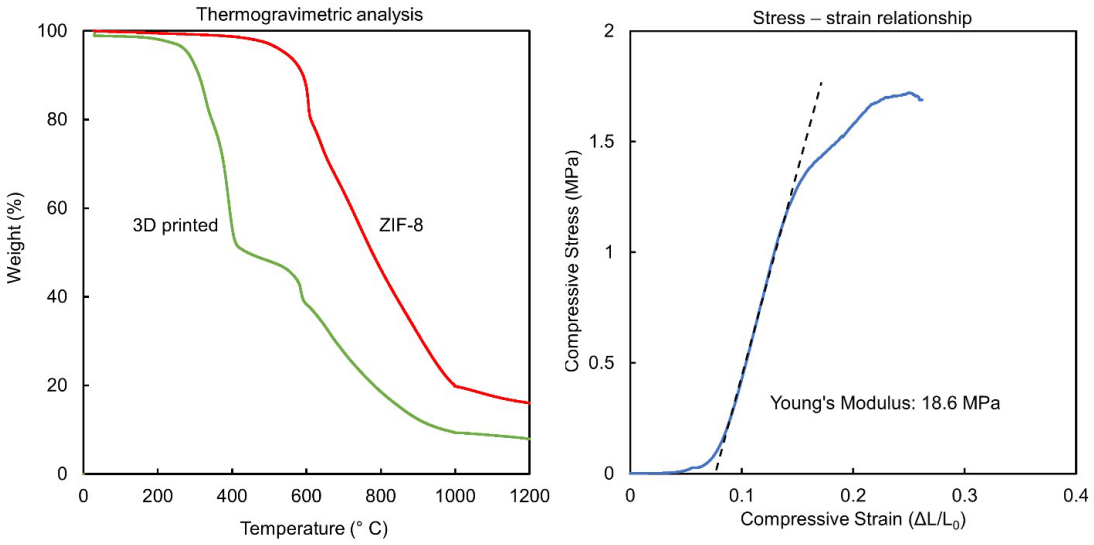


**Figure 2.6** (a) Thermogravimetric analysis of pure ZIF-8 crystalline powder and ZIF-8 3D printed with nanocellulose. (b) Compressive stress-strain curve of the 3D printed lattice pyrolyzed at 1,000 °C.

Although the calculated Brunauer-Emmett-Teller (BET) surface area of 660 $m^2$ $g^{-1}$ is quite high, other significant benefits of the ZIF-8 derived material are the nano-sized pores and narrow pore size distribution. Two distinct pore sizes are contained within the pyrolyzed ZIF-8: micropores retained from the ZIF-8 template and mesopores that are not found in pure ZIF-8. The pore size distribution in the microporous region is exceptionally narrow and corresponds with the pore diameter of pure ZIF-8. We conclude that ZIF-8 served as a template to produce a carbonized material with uniform micropores, the presence of which provides high surface area and maximizes interactions with small guest species such as zinc ions. Mesopores were formed during pyrolysis and provide a third length scale of porosity intermediate

between the micropores of the ZIF-8 template and the macroscopic pores of the 3D printed architecture. We expect this hierarchical porosity to aid in the mass transport of guest species within the pore space.[40]

Pyrolysis caused graphitization of the ZIF-8 lattice with some zinc and nitrogen remaining as evidenced by several methods, including XPS, energy dispersive X-ray spectroscopy (EDS), and electron energy loss spectroscopy (EELS). The elemental atomic composition indicated by both EDS and EELS consisted of 83% carbon, 10% oxygen, 5% zinc, and 2% nitrogen after pyrolysis compared to 67% carbon, 12% oxygen, 10% zinc, and 11% nitrogen before pyrolysis (Table 2.1). While carbon is generally overestimated and nitrogen is underestimated by these methods, comparison before and after pyrolysis confirms carbonization of the 3D printed ZIF-8 lattice has occurred with the retention of some nitrogen and zinc. Elemental mapping revealed carbon and nitrogen are homogeneously distributed while zinc and oxygen sometimes co-locate as a segregated phase (Figure 2.7a). Thin sheets consisting of carbon and nitrogen are also visible. The carbon 1*s* to $\pi^*$ transition of 285 eV predominates in XPS (Figure 2.5), EDS (Figure 2.7b), and EELS (Figure 2.7c) corresponding to a carbon hybridization of $sp^2$ and indicating amorphous graphitic carbon. The N 1*s* electron binding energies correspond in equal proportion to graphitic (401 eV) and pyridinic (399 eV) species indicating the nitrogen is distributed within the graphitic carbon layers.[41] Taken together, these results support conversion of the ZIF-8 to a nitrogen-doped graphitic material suitable for integration into electrical devices.[42]

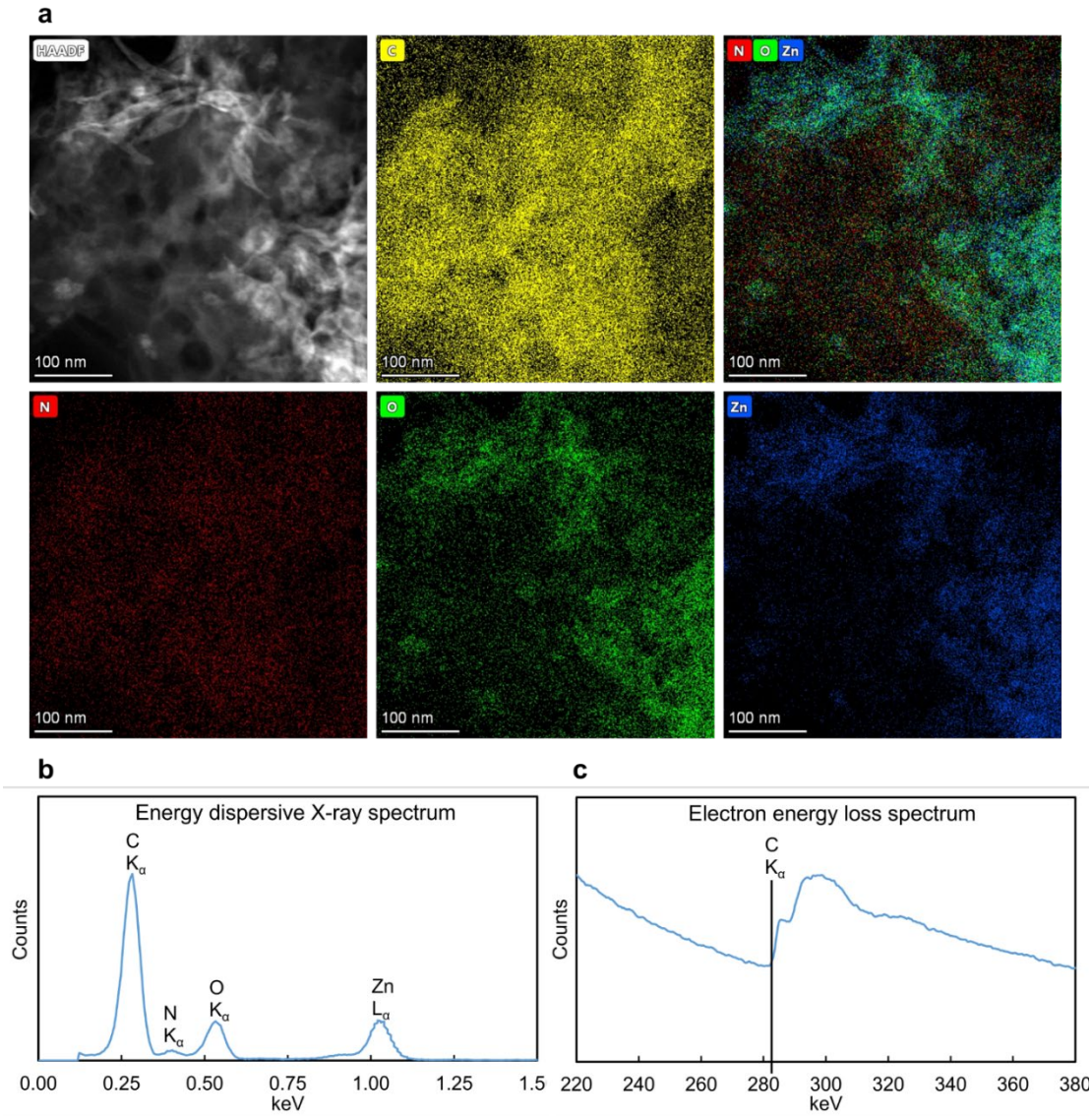


**Figure 2.7** Elemental composition of the 3D printed ZIF-8 lattice after pyrolysis. (a) High-angle annular dark field image of pyrolyzed ZIF-8 and the corresponding elemental atomic maps, (b) energy dispersive X-ray spectrum, and (c) electron energy loss spectrum.

We expect the retention of zinc and nitrogen in the structure may improve the ion capacity of the ZIF-8 derived material compared to pure carbon. ZIF-8 lattices pyrolyzed at temperatures above 1,000 °C retained less nitrogen and no zinc (Table 2.1) and did not perform nearly as well. A previous study demonstrated that zinc and sulfate ion coordination by a nitrogen-containing cathode contributed to the capacitance of a ZIHC. Attractive interactions of the nitrogen ligands with the zinc and sulfate ions provided pseudocapacitance and increased charge storage of the device.[43] A separate study also demonstrated an increase in the areal capacitance of a ZIHC when coordination sites for zinc ions were incorporated into the carbon-based cathode to promote chemical adsorption.[44] In the case of our cathode material, pyridinic nitrogen is a good ligand for zinc ions and may hydrogen-bond with counterions such as sulfate, so its presence may increase ion affinity.[45] The presence of zinc throughout the pyrolysis may help template suitable binding environments for additional zinc ions. The retention of zinc at 1,000 °C may indicate that zinc ion adsorption sites persist in the cathode material when pyrolyzed at this temperature. Pyrolysis at higher temperatures may induce a structural evolution that is no longer templated by the presence of zinc and therefore has lower affinity for zinc ions. Greater zinc ion adsorption in the cathode increases overall capacitance.[46]

**Electrochemical Tests as Zinc-Ion Hybrid Capacitor Cathodes**

The electrochemical properties of the graphitized ZIF-8 lattice with a thickness of 1 mm (denoted as ZIF8/cel-1mm) was tested in a three-electrode system using zinc foil as a counter electrode, saturated calomel electrode (SCE) as a reference electrode,

and 2 M $ZnSO_4$ aqueous solution as electrolyte. The 1 mm-thick graphitized lattice cathode printed from pure cellulose without ZIF-8 (denoted as cel-1mm) was also tested for comparison. Cyclic voltammetry (CV) curves collected at 5 mV $s^{-1}$ (Figure 2.8) reveal that the graphitized cathode has a wide potential window from -0.8 to 0.6 V vs. SCE, while the zinc anode operates from -1.2 to -0.8 V vs. SCE. Together, they achieve a broad device voltage window of 1.8 V. Both ZIF8/cel-1mm and cel-1mm exhibited quasi-rectangular shaped CV curves, indicating capacitor-type behavior. Significantly, the ZIF8/cel-1mm achieves an excellent areal capacitance of 2.40 F $cm^{-2}$, substantially higher than that of cel-1mm (0.671 F $cm^{-2}$).

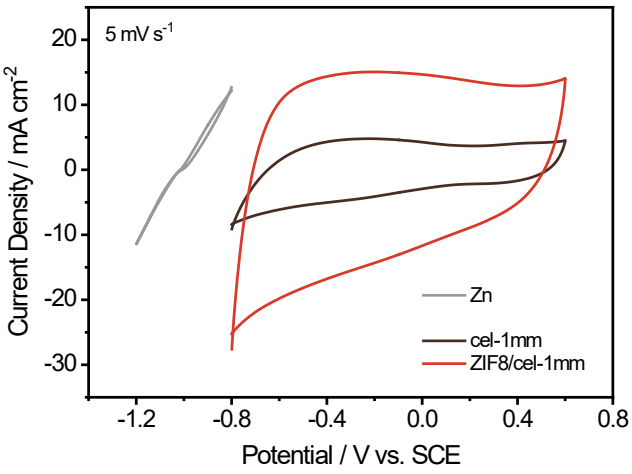


**Figure 2.8** CV curves of the ZIF8/cel-1mm and cel-1mm cathodes paired with a Zn anode measured at a scan rate of 5 mV $s^{-1}$.

We suspect the significant capacitance improvement is a result of the increased surface area, microporosity, and attractive interactions with ions imparted by the ZIF-

8 template. The CV curves of ZIF8/cel-1mm and cel-1mm were collected at scan rates from 0.1-1.0 mV $s^{-1}$ (Figures 2.9a and 2.9b). The cathodic and anodic current densities at 0 V vs. SCE as were plotted as a function of scan rate (Figure 2.10). We observed a linear relation of the scan rate with the average of the cathodic and anodic current densities (Figure 2.11), where the slope is the electrochemical double-layer capacitance ($C_{dl}$) per projected electrode area. The electrochemical double-layer capacitance of ZIF8/cel-1mm (3.27 F $cm^{-2}$) is roughly 5-fold higher than that of cel-1mm (0.523 F $cm^{-2}$). Assuming both samples have the same nominal value of double-layer capacitance of a smooth carbon surface ($C_{dl(smooth)}$, 60 μF $cm^{-2}$), ZIF8/cel-1mm has a considerably larger electrochemically active (ion accessible) surface area (ECSA) than cel-1mm.

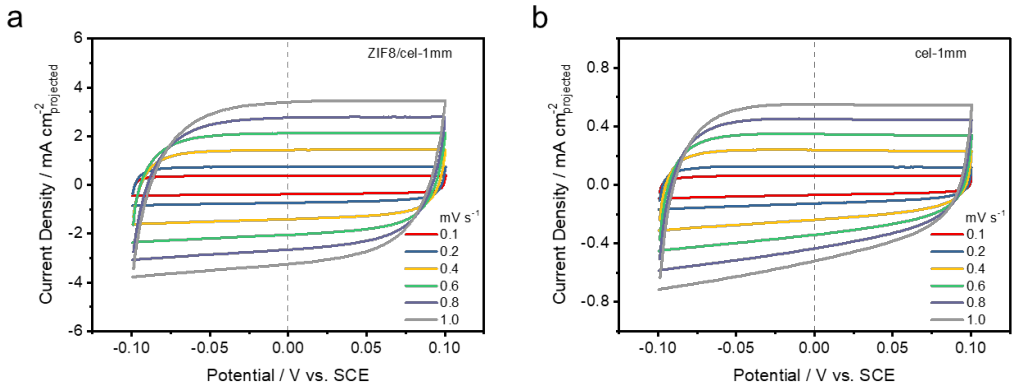


**Figure 2.9** CV curves measured at scan rates from 0.1 to 1.0 mV $s^{-1}$ of (a) ZIF8/cel-1mm and (b) cel-1mm.

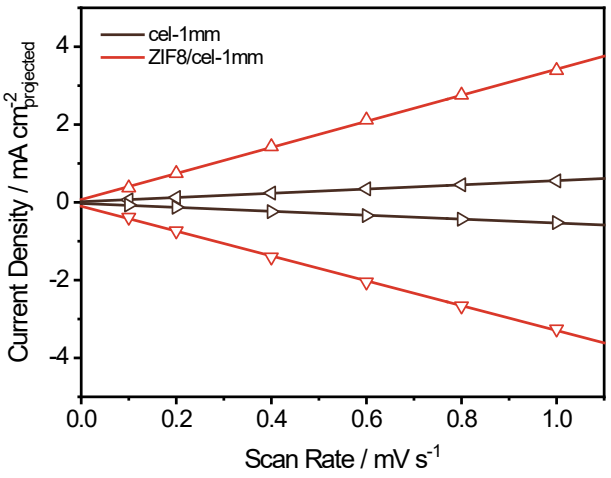


**Figure 2.10** Cathodic and anodic current densities of ZIF8/cel-1mm and cel-1mm measured at 0 V vs. SCE as a function of scan rate.

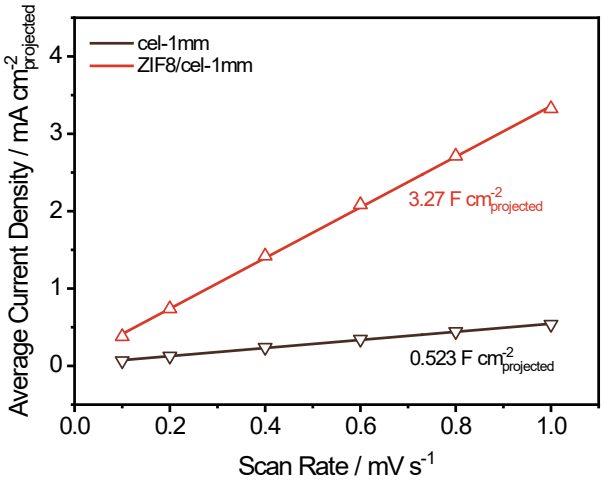


**Figure 2.11** Average areal current densities of ZIF8/cel-1mm and cel-1mm measured at 0 V vs. SCE as a function of scan rate.

To investigate the charge storage mechanism of ZIF8/cel-1mm, Trasatti capacitance contribution analysis was employed to quantitatively deconvolute the contributions from surface capacitive process and diffusion-controlled process.[47-49] The areal capacitances were calculated from cyclic voltammetry curves (Figure 2.12) and plotted against $v^{-1/2}$ ($v$ is scan rate) in (Figure 2.13). A linear relation at low scan rates can be observed assuming semi-infinite ion diffusion. An exceptionally high areal capacitance ($C_{surface}$) of 2.03 F cm$^{-2}$ contributed by surface capacitive process was determined from the y-intercept ($v \rightarrow +\infty$) of the extrapolated fitting line. The surface capacitive process involves fast reversible adsorption/desorption of ions ($Zn^{2+}$, $SO_4^{2-}$, $H^+$, *etc.*) at the electric double layer of the high surface area carbon electrode. Even at a low scan rate of 1 mV s$^{-1}$, the surface capacitance accounts for as high as 62.5% of the total capacitance (Figure 2.14). When the scan rate increases to 5 and 10 mV s$^{-1}$, the contribution rises to 79.8% and 92.6%. These results evidence that the surface capacitive behavior dominates the charge storage of the ZIF8/cel cathode, especially at high scan rates.

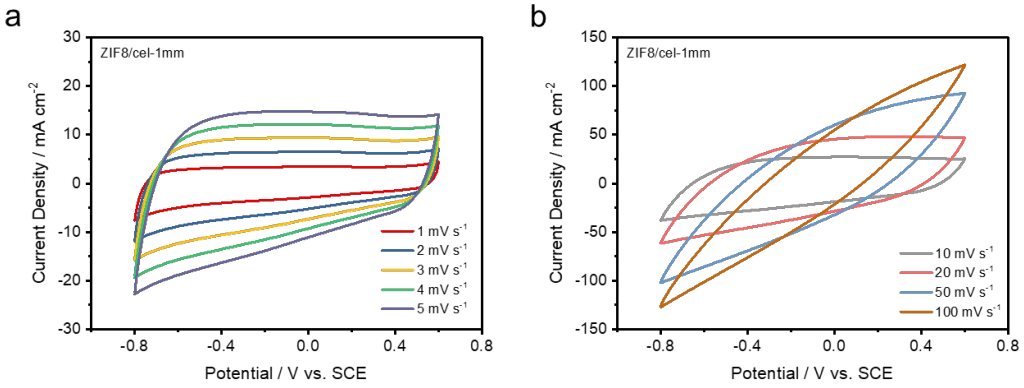

**Figure 2.12** CV curves of ZIF8/cel-1mm measured at (a) low scan rates and (b) high scan rates.

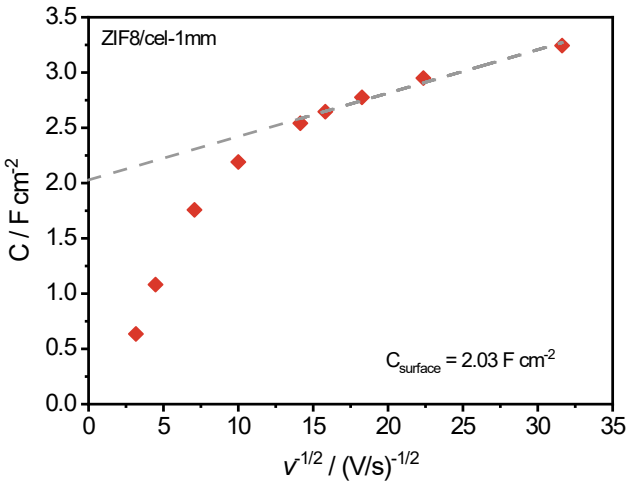


**Figure 2.13** Plot of areal capacitance ($C$) vs. $v^{-1/2}$ for ZIF8/cel-1mm.

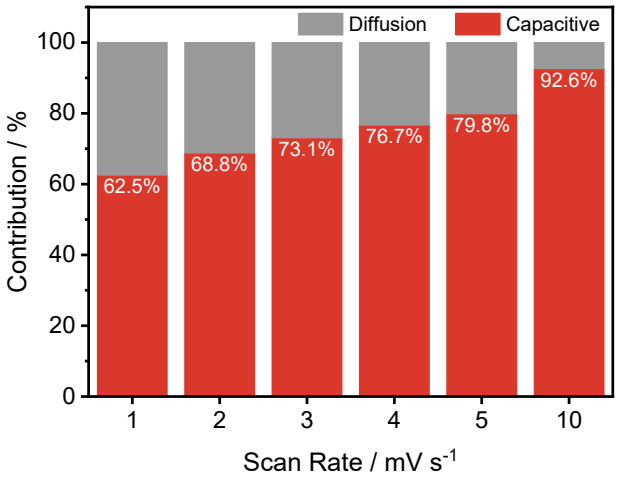

**Figure 2.14** Capacitive and diffusion contribution of ZIF8/cel-1mm at various scan rates.

We fabricated ZIHCs in a beaker cell (Figure 2.2) using ZIF8/cel-1mm and cel-1mm as cathodes and zinc foil as the anode. The quasi-rectangular CV curves (Figure 2.15) and the quasi-triangular galvanostatic charge/discharge (GCD) curves (Figure 2.16) were obtained from both devices, as expected for typical capacitor-battery hybrid behavior. Since the capacity of the zinc anode in a ZIHC device is typically in excess, the device capacity is largely determined by the capacity of the carbon cathode. The device data show good agreement with the electrode results. Because of the significantly improved ECSA, the ZIF8/cel-1mm//Zn device shows a 5-fold enhancement in both areal capacity and capacitance compared to the cel-1mm//Zn device (Figures 2.17a and 2.17b). It achieved a maximum areal capacity of 2.64 mA h $cm^{-2}$ and a capacitance of 5.30 F $cm^{-2}$. The enhanced capacitance can be attributed to the addition of ZIF-8 to the ink formulation that effectively boosts the cathode's surface area by retaining the porosity of the ZIF-8 template. We also compared the areal capacitances of ZIHC devices using 3D printed ZIF-8 lattices pyrolyzed at temperatures 1,000, 1,200, and 1,400 °C (Figure 2.18). Although these electrodes have comparable surface area (Table 2.1), the ZIF-8 lattices pyrolyzed at higher temperatures (1,200 and 1,400 °C) retained little nitrogen and no zinc, and the capacitances of the corresponding ZIHC devices are considerably lower than the sample pyrolyzed at 1,000 °C. The results suggest the presence of nitrogen and zinc in

the pyrolyzed ZIF-8 cathode also play a positive role in improving the capacitance by enhancing the conductivity and ion affinity of the cathode.[10,13] Electrochemical impedance spectroscopy (EIS) data (Figure 2.19) further shows the ZIF8/cel-1mm//Zn device has a considerably smaller charge transfer resistance, indicating the important role of the hierarchically porous structure created by the microporous ZIF-8 template combined with the macroporous 3D printed lattice in facilitating ion diffusion. As a result, the ZIF8/cel-1mm//Zn device demonstrates an excellent capacitance retention of 57.6% (Figure 2.17b).

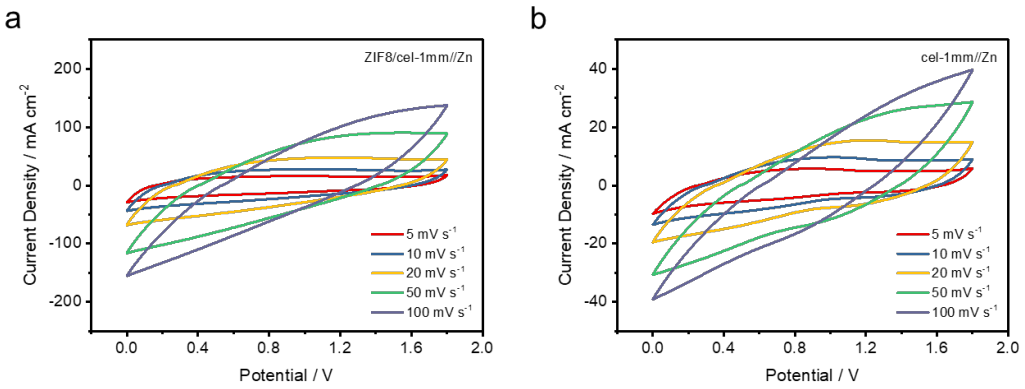


**Figure 2.15** CV curves measured at scan rates from 5 to 100 mV $s^{-1}$ of (a) ZIF8/cel-1mm//Zn and (b) cel-1mm//Zn.

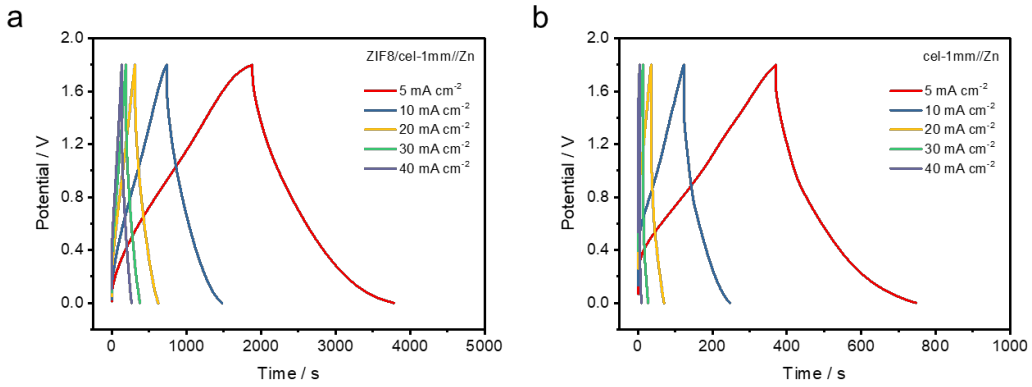


**Figure 2.16** GCD curves measured at current densities from 5 to 40 mA $cm^{-2}$ of (a) ZIF8/cel-1mm//Zn and (b) cel-1mm//Zn.

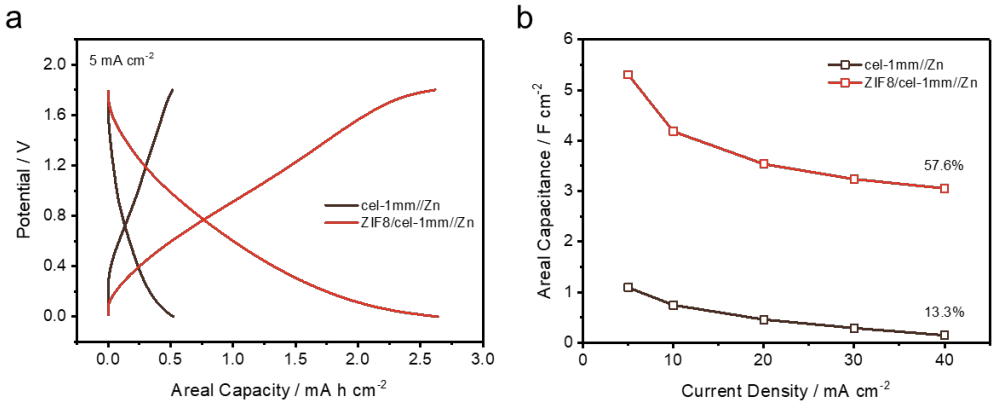


**Figure 2.17** (a) Charge-discharge capacities of ZIF8/cel-1mm//Zn and cel-1mm//Zn measured at a current density of 5 mA $cm^{-2}$. (b) Areal capacitances and capacitance retentions of ZIF8/cel-1mm//Zn and cel-1mm//Zn at different current densities.

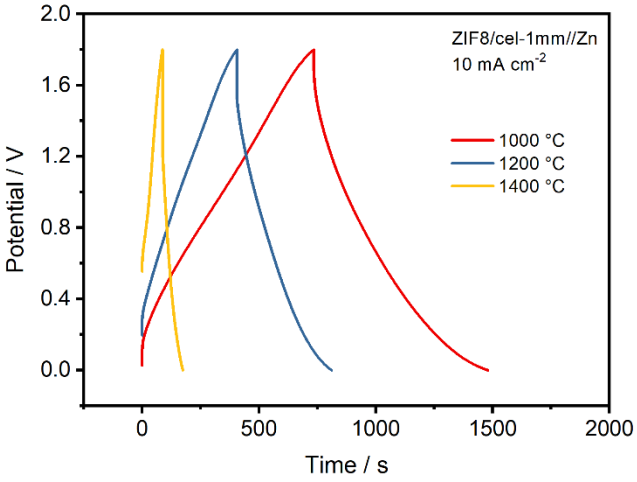


**Figure 2.18** GCD curves measured at 10 mA $cm^{-2}$ of ZIHC devices with ZIF8/cel-1mm cathodes pyrolyzed at different temperatures.

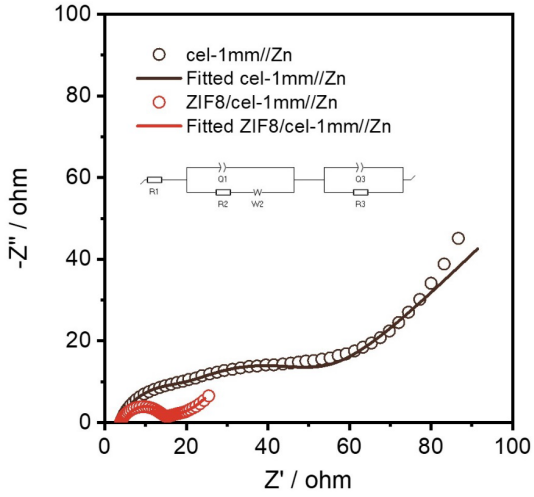


**Figure 2.19** Electrochemical impedance spectra of ZIF8/cel-1mm//Zn and cel-1mm//Zn. Frequency range: $10^{-2}$-$10^{6}$ Hz.

3D printing offers great flexibility and new opportunities in design and fabrication of energy storage devices. Conventional devices are fabricated as layered sheets, in which the thickness of each layer must be kept at micron scale to ensure efficient charge and ion diffusion. Stacking of multiple electrode layers is therefore necessary to meet the required loading of active material. The recent development of 3D printed electrodes provides an alternative method to reach high mass loading by increasing the electrode thickness,[50] while retaining excellent ion diffusion in the thick electrode. To further increase the areal capacitance and energy density of the ZIHC devices, we increased the electrode thickness to 2 mm (denoted as ZIF8/cel-2mm) and 3 mm (denoted as ZIF8/cel-3mm). As shown in Figure 2.20, the electrode mass increases linearly with the electrode thickness, with an average density of 217 mg $cm^{-3}$ (218, 216 and 217 mg $cm^{-3}$ for ZIF8/cel-1mm, ZIF8/cel-2mm, and ZIF8/cel-3mm, respectively). Figure 2.21 and Figure 2.22 show the electrochemical performances of ZIHC devices using ZIF8/cel cathodes with different thicknesses. The current densities of the quasi-rectangular CV curves of ZIF8/cel-1mm//Zn, ZIF8/cel-2mm//Zn and ZIF8/cel-3mm//Zn increase with the cathode thickness (Figure 2.22). Consistently, all three GCD curves exhibit quasi-triangular shapes (Figure 2.22). The maximum discharging capacity (Figure 2.23a) and capacitance (Figure 2.23b) obtained at 5 mA $cm^{-2}$ increases almost linearly with the cathode thickness. Significantly, the areal capacities of ZIF8/cel//Zn substantially outperform other reported ZIHC devices (Figure 2.24 and Table 2.2).[8,43,51-56] It is noteworthy that the increase of electrode thickness and mass did not severely sacrifice the rate capability of the ZIHC device.

When normalizing the capacitance to electrode volume (Figure 2.25a) and mass (Figure 2.25b), the 1 mm and 3 mm samples have almost the same volumetric and gravimetric capacitances. The discrepancy increases slightly with increased current density. These results confirm the 3D printed hierarchically porous structure is effective in maintaining accessibility to the electroactive sites despite the increased electrode volume and mass. This result is also reflected in the EIS results with good overlap between the semi-circles of 1 mm and 2 mm samples (Figure 2.26). ZIF8/cel-3mm//Zn reaches a maximum areal energy density of 7.23 mWh $cm^{-2}$ while ZIF8/cel-1mm//Zn reaches a maximum areal power density of 34.7 mW $cm^{-2}$ (Ragone plot, areal energy density vs. areal power density, Figure 2.27). These values are substantially higher than those reported for ZIHC devices constructed from cathodes based on other carbon materials (Table 2.2) Finally, all ZIF8/cel//Zn devices exhibited excellent cyclic stability with no capacitance decay after 2,000 CV cycles at 100 mV $s^{-1}$ (Figure 2.28). A slight increase in capacitance is presumably caused by further electrolyte permeation into the carbon structure.

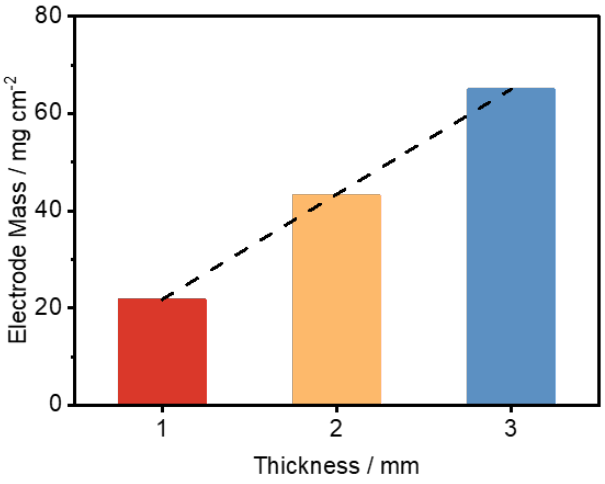


**Figure 2.20** Mass of ZIF8/cel electrodes with different thicknesses.

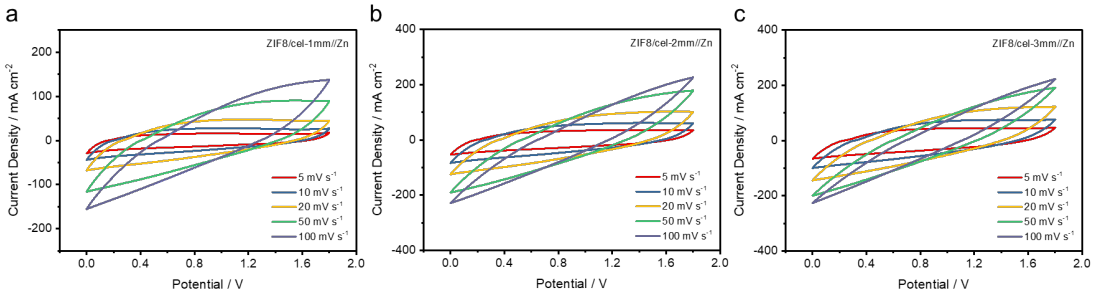


**Figure 2.21** CV curves measured at scan rates from 5 to 100 mV $s^{-1}$ of (a) ZIF8/cel-1mm//Zn, (b) ZIF8/cel-2mm//Zn, and (c) ZIF8/cel-3mm//Zn.

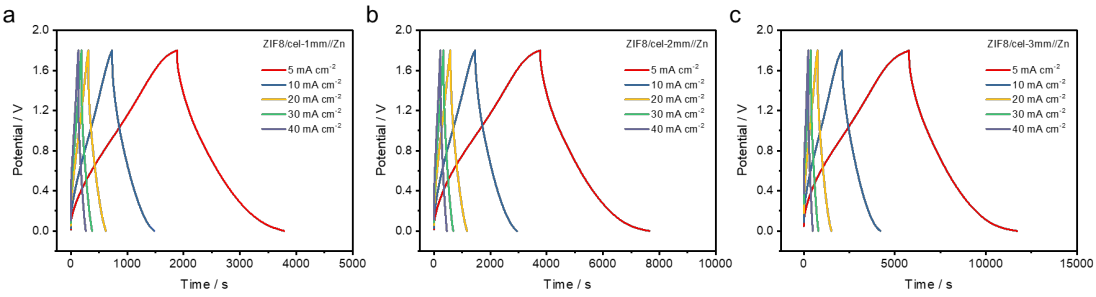

**Figure 2.22** GCD curves measured at current densities from 5 to 40 mA $cm^{-2}$ of (a) ZIF8/cel-1mm//Zn, (b) ZIF8/cel-2mm//Zn, and (c) ZIF8/cel-3mm//Zn.

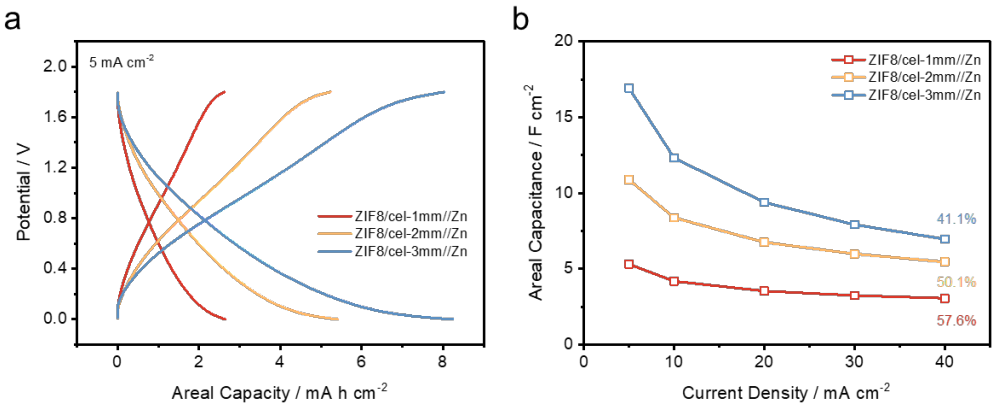


**Figure 2.23** (a) Charge-discharge capacities of ZIF8/cel-1mm//Zn, ZIF8/cel-2mm//Zn and ZIF8/cel-3mm//Zn measured at a current density of 5 mA $cm^{-2}$. (b) Areal capacitances and capacitance retentions of ZIF8/cel-1mm//Zn, ZIF8/cel-2mm//Zn and ZIF8/cel-3mm//Zn at different current densities.

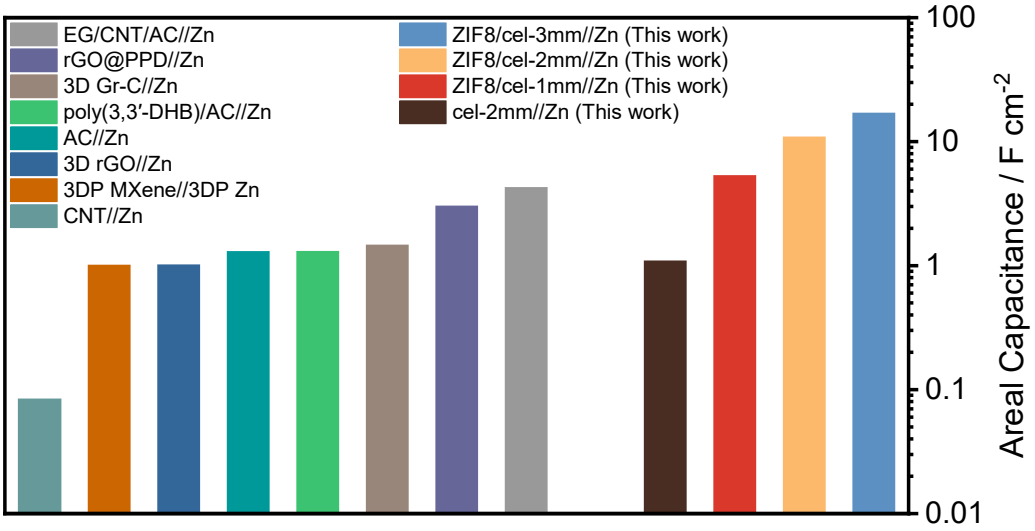


**Figure 2.24** A plot compares the areal capacitance of ZIF8/cel//Zn and cel-1mm//Zn with the values of previously reported ZIHCs.[8,43,51-56]

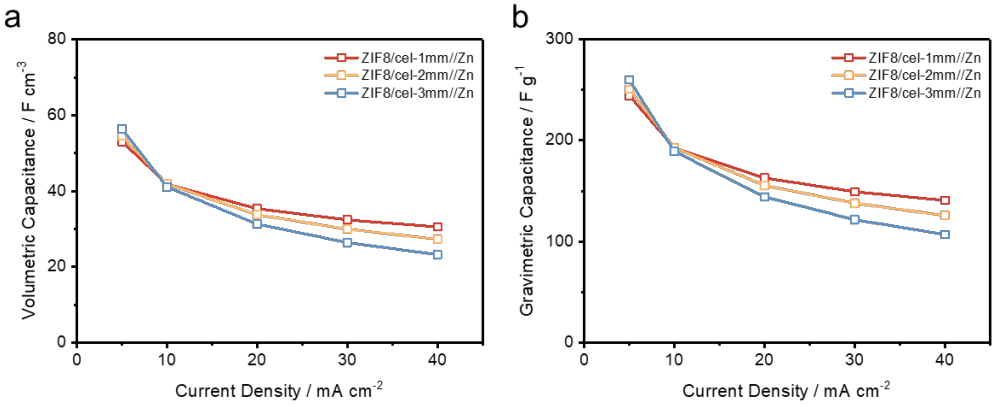


**Figure 2.25** (a) Volumetric capacitances and (b) gravimetric capacitances of ZIF8/cel-1mm//Zn, ZIF8/cel-2mm//Zn and ZIF8/cel-3mm//Zn at different current densities.

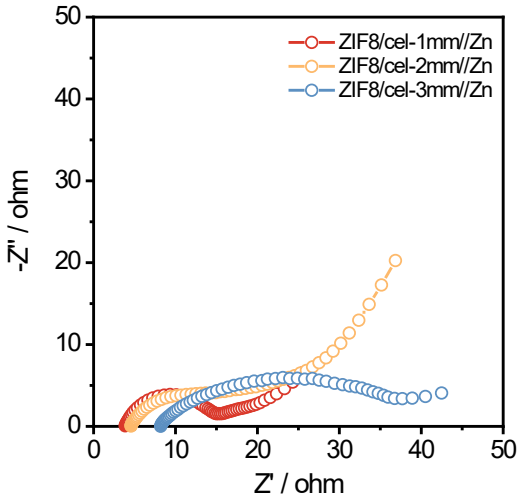


**Figure 2.26** Electrochemical impedance spectra of ZIF8/cel-1mm//Zn, ZIF8/cel-2mm//Zn and ZIF8/cel-3mm//Zn. Frequency range: $10^{-2}$-$10^{6}$ Hz.

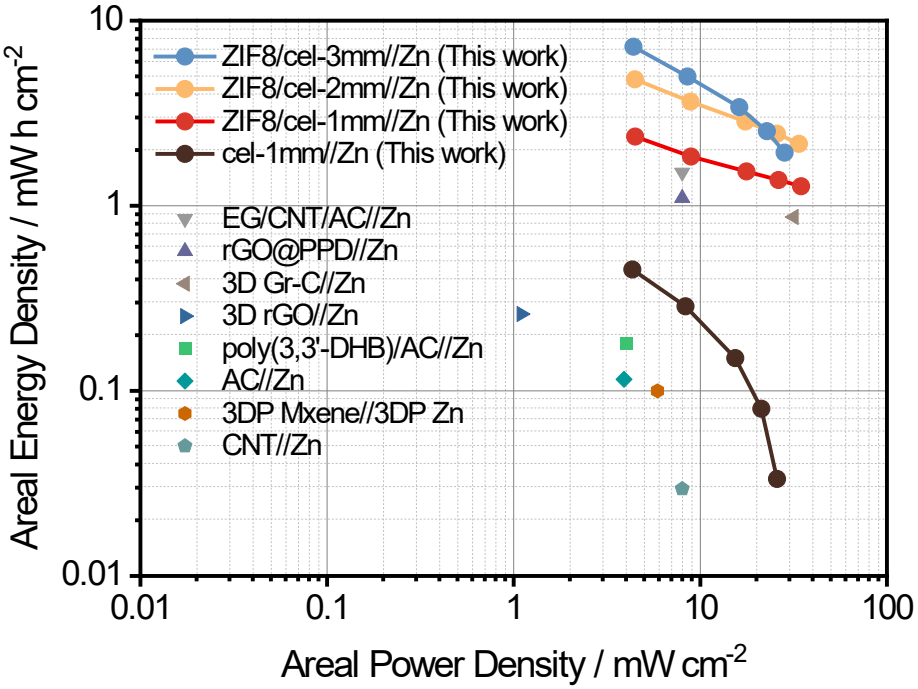

**Figure 2.27** Ragone plot comparing ZIF8/cel//Zn and cel-1mm//Zn with previously reported ZIHCs.[8,43,51-56]

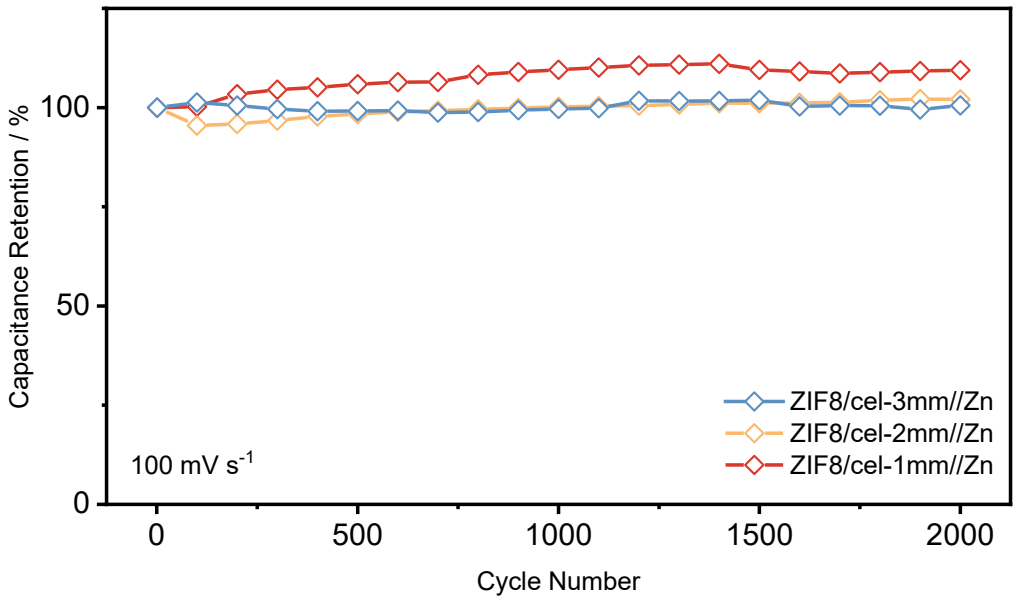


**Figure 2.28** Cyclic stability of ZIF8/cel-1mm//Zn, ZIF8/cel-2mm//Zn and ZIF8/cel-3mm//Zn measured at a scan rate of 100 mV $s^{-1}$.

**Table 2.2** Summary of electrochemical performances of ZIHCs. Samples reported in this work are highlighted in blue text.

| **Cathode** | **Thickness (mm)** | **Mass Loading (mg $cm^{-2}$)** | **Anode** | **Electrolyte** | **Voltage Window (V)** | **Max $C_A$ (F $cm^{-2}$)** | **Max $E_A$ (mW h $cm^{-2}$)** | **Max $P_A$ (mW $cm^{-2}$)** |
|---|---|---|---|---|---|---|---|---|
| CNT[56] | 0.02 | - | Zn | 1 M $ZnSO_4$ | 0.2-1.8 | 0.0832 | 0.0296 | 8 |

| Cathode | Thickness (mm) | Mass Loading (mg $cm^{-2}$) | Anode | Electrolyte | Voltage Window (V) | Max $C_A$ (F $cm^{-2}$) | Max $E_A$ (mW h $cm^{-2}$) | Max $P_A$ (mW $cm^{-2}$) |
|---|---|---|---|---|---|---|---|---|
| 3DP MXene[51] | 0.5 | 3.9 | 3DP CNT/Zn | 2 M $ZnSO_4$ | 0.1-1.2 | 1.0064 | 0.10 | 5.9 |
| AC[52] | 0.08 | - | Zn | 2 M $ZnSO_4$ | 0.5-1.5 | 1.297 | 0.1154 | 3.9 |
| poly(3, 3′-DHB)/AC[43] | - | 9.1 | Zn | 2 M $ZnSO_4$ | 0.5-1.5 | 1.3 | 0.18 | 4.01 |
| 3D rGO[53] | - | 5.5 | Zn | 1 M $ZnSO_4$ | 0.01-1.8 | 1.011 | 0.26 | 1.1 |
| 3D Gr-C[54] | 2.1 | 38 | Zn | 2 M $ZnSO_4$ and 2 M NaCl | 0-1.8 | 1.46 | 0.87 | 31.72 |
| rGO@PPD[55] | 0.024 | 4.5-5.0 | Zn | 1 M $Zn(Ac)_2$ | 0.2-1.8 | 3.0125 | 1.1 | 8 |
| EG/CNT/AC[8] | 3.2 | 22.8 | Zn | 2 M $ZnSO_4$ /$SiO_2$ gel | 0.2-1.8 | 4.259 | 1.514 | 8 |
| cel-1mm | 1.00 | 15.2 | Zn | 2 M $ZnSO_4$ | 0-1.8 | 1.09 | 0.453 | 25.8 |
| ZIF8/cel-1mm | 1.00 | 21.8 | Zn | 2 M $ZnSO_4$ | 0-1.8 | 5.30 | 2.36 | 34.7 |
| ZIF8/cel-2mm | 2.00 | 43.2 | Zn | 2 M $ZnSO_4$ | 0-1.8 | 10.9 | 4.82 | 33.8 |
| ZIF8/cel-3mm | 3.00 | 65.1 | Zn | 2 M $ZnSO_4$ | 0-1.8 | 16.9 | 7.23 | 28.3 |

## 2.4 Conclusion

In summary, a zinc-ion hybrid capacitor with exceptional performance was fabricated from a 3D printed microporous cathode material templated by the zinc imidazolate MOF known as ZIF-8. We developed an aqueous ink of 77 wt.% ZIF-8 supported by nanocellulose that we 3D printed through a 600 μm nozzle into a woodpile lattice architecture of 1.5 × 1.5 × 0.1-0.3 cm. We found that pyrolysis converted the 3D printed ZIF-8 lattice into an electrically conductive graphitic material that retained the microporosity and high surface area of the ZIF-8. These properties, combined with the hierarchical porosity of the 3D printed structure, provide a cathode material well suited to ion insertion and transport. The pyridinic nitrogen originating from the imidazole linkers may contribute to enhanced ion affinity and electrical conductivity. These advantages led to superior performance when assembled into a zinc-ion hybrid capacitor with a zinc foil anode, including a record high areal capacitance of 16.9 F $cm^{-2}$ and an exceptional areal energy density of 7.23 mW h $cm^{-2}$. This work demonstrates that the tunable chemical and surface properties of MOFs make them ideal templates of electrode materials tailor-made for affinity and transport of specific electrolyte ions. Our 3D printing results provide insight into the development of high wt.% MOF inks for high resolution (<1 mm) direct ink writing.

## References

1. M. Arbabzadeh, R. Sioshansi, J. X. Johnson, G. A. Keoleian. *Nat. Commun.* **2019**, *10*, 3413.

2. W. A. Braff, J. M. Mueller, J. E. Trancik. *Nat. Clim. Change* **2016**, *6*, 964-969.

3. F. Cheng, J. Liang, Z. Tao, J. Chen. *Adv. Mater.* **2011**, *23*, 1695-1715.

4. J. Ding, W. Hu, E. Paek, D. Mitlin. *Chem. Rev.* **2018**, *118*, 6457-6498.

5. T. Liu, Y. Li. *InfoMat* **2020**, *2*, 807-842.

6. J. Yang, M. A. Bissett, R. A. W. Dryfe. *ChemSusChem* **2021**, *14*, 1700-1709.

7. A. Vlad, N. Singh, J. Rolland, S. Melinte, P. M. Ajayan, J. F. Gohy. *Sci. Rep.* **2014**, *4*, 4315.

8. Y. Liu, S. Zheng, J. Ma, X. Wang, L. Zhang, P. Das, K. Wang, Z.-S. Wu. *Adv. Energy Mater.* **2022**, *12*, 2200341.

9. S. Wu, Y. Chen, T. Jiao, J. Zhou, J. Cheng, B. Liu, S. Yang, K. Zhang, W. Zhang. *Adv. Energy Mater.* **2019**, *9*, 1902915.

10. H. Zhang, Q. Liu, Y. Fang, C. Teng, X. Liu, P. Fang, Y. Tong, X. Lu. *Adv. Mater.* **2019**, *31*, 1904948.

11. A. Muzaffar, M. B. Ahamed, K. Deshmukh, J. Thirumalai. *Renewable Sustainable Energy Rev.* **2019**, *101*, 123-145.

12. H. Furukawa, K. E. Cordova, M. O'Keeffe, O. M. Yaghi. *Science* **2013**, *341*, 1230444.

13. Z. Wang, J. Huang, Z. Guo, X. Dong, Y. Liu, Y. Wang, Y. Xia. *Joule* **2019**, *3*, 1289-1300.

14. H. B. Wu, S. Wei, L. Zhang, R. Xu, H. H. Hng, X. W. Lou. *Chem. Eur. J.* **2013**, *19*, 10804-10808.

15. G. Cao, D. Bi, J. Zhao, J. Zheng, Z. Wang, Q. Lai, Y. Liang. *RSC Adv.* **2020**, *10*, 17345-17352.

16. N. Liédana, A. Galve, C. Rubio, C. Téllez, J. Coronas. *ACS Appl. Mater. Interfaces* **2012**, *4*, 5016-5021.

17. A. S. Munn, P. W. Dunne, S. V. Y. Tang, E. H. Lester. *Chem. Commun.* **2015**, *51*, 12811-12814.

18. N. C. Burtch, H. Jasuja, K. S. Walton. *Chem. Rev.* **2014**, *114*, 10575-10612.

19. K. S. Park, Z. Ni, A. P. Côté, J. Y. Choi, R. Huang, F. J. Uribe-Romo, H. K. Chae, M. O'Keeffe, O. M. Yaghi. *Proc. Natl. Acad. Sci.* **2006**, *103*, 10186-10191.

20. Z.-H. Huang, T.-Y. Liu, Y. Song, Y. Li, X.-X. Liu. *Nanoscale* **2017**, *9*, 13119-13127.

21. S. Fleischmann, J. B. Mitchell, R. Wang, C. Zhan, D.-e. Jiang, V. Presser, V. Augustyn. *Chem. Rev.* **2020**, *120*, 6738-6782.

22. T. Liu, F. Zhang, Y. Song, Y. Li. *J. Mater. Chem. A* **2017**, *5*, 17705-17733.

23. J. Sánchez-Laínez, B. Zornoza, S. Friebe, J. Caro, S. Cao, A. Sabetghadam, B. Seoane, J. Gascon, F. Kapteijn, C. Le Guillouzer, G. Clet, M. Daturi, C. Téllez, J. Coronas. *J. Membr. Sci.* **2016**, *515*, 45-53.

24. J. A. Lewis. *Adv. Funct. Mater.* **2006**, *16*, 2193-2204.

25. C.-T. Hsieh, K. Ariga, L. K. Shrestha, S.-h. Hsu. *Biomacromolecules* **2021**, *22*, 1053-1064.

26. L. Zhong, J. Chen, Z. Ma, H. Feng, S. Chen, H. Cai, Y. Xue, X. Pei, J. Wang, Q. Wan. *Nanoscale* **2020**, *12*, 24437-24449.

27. J. Dhainaut, M. Bonneau, R. Ueoka, K. Kanamori, S. Furukawa. *ACS Appl. Mater. Interfaces* **2020**, *12*, 10983-10992.

28. Z. Lyu, G. J. H. Lim, R. Guo, Z. Pan, X. Zhang, H. Zhang, Z. He, S. Adams, W. Chen, J. Ding, J. Wang. *Energy Storage Mater.* **2020**, *24*, 336-342.

29. B. Thomas, M. C. Raj, A. K. B, R. M. H, J. Joy, A. Moores, G. L. Drisko, C. Sanchez. *Chem. Rev.* **2018**, *118*, 11575-11625.

30. C. Zhu, T. Liu, F. Qian, W. Chen, S. Chandrasekaran, B. Yao, Y. Song, E. B. Duoss, J. D. Kuntz, C. M. Spadaccini, M. A. Worsley, Y. Li. *Nano Today* **2017**, *15*, 107-120.

31. W. Chen, H. Yu, S.-Y. Lee, T. Wei, J. Li, Z. Fan. *Chem. Soc. Rev.* **2018**, *47*, 2837-2872.

32. K.-Y. Lee, Y. Aitomäki, L. A. Berglund, K. Oksman, A. Bismarck. *Compos. Sci. Technol.* **2014**, *105*, 15-27.

33. C. Zhu, J. E. Smay. *J. Mater. Process. Technol.* **2012**, *212*, 727-733.

34. C. Zhu, J. E. Smay. *J. Rheol.* **2011**, *55*, 655-672.

35. B. Yao, H. Peng, H. Zhang, J. Kang, C. Zhu, G. Delgado, D. Byrne, S. Faulkner, M. Freyman, X. Lu, M. A. Worsley, J. Q. Lu, Y. Li. *Nano Lett.* **2021**, *21*, 3731-3737.

36. O. Kostko, B. Xu, M. Ahmed. *Phys. Chem. Chem. Phys.* **2021**, *23*, 8847-8853.

37. M. B. Haider. *Nanoscale Res. Lett.* **2017**, *12*, 5.

38. L. S. Xie, G. Skorupskii, M. Dincă. *Chem. Rev.* **2020**, *120*, 8536-8580.

39. S. Brunauer, P. H. Emmett, E. Teller. *J. Am. Chem. Soc.* **1938**, *60*, 309-319.

40. S. Chandrasekaran, B. Yao, T. Liu, W. Xiao, Y. Song, F. Qian, C. Zhu, E. B. Duoss, C. M. Spadaccini, Y. Li, M. A. Worsley. *Mater. Horiz.* **2018**, *5*, 1166-1175.

41. Y. Shao, S. Zhang, M. H. Engelhard, G. Li, G. Shao, Y. Wang, J. Liu, I. A. Aksay, Y. Lin. *J. Mater. Chem.* **2010**, *20*, 7491-7496.

42. T. Kondo, D. Guo, T. Shikano, T. Suzuki, M. Sakurai, S. Okada, J. Nakamura. *Sci. Rep.* **2015**, *5*, 16412.

43. N. Wang, T. Xin, Y. Zhao, Q. Li, M. Hu, J. Liu. *ACS Sustainable Chem. Eng.* **2019**, *7*, 14195-14202.

44. X. Li, Y. Li, S. Xie, Y. Zhou, J. Rong, L. Dong. *Chem. Eng. J.* **2022**, *427*, 131799.

45. T. Liu, T. Kou, D. Bulmahn, C. Ortuno-Quintana, G. Liu, J. Q. Lu, Y. Li. *ACS Appl. Energy Mater.* **2018**, *1*, 5043-5053.

46. H. Wang, M. Wang, Y. Tang. *Energy Storage Mater.* **2018**, *13*, 1-7.

47. Y. Song, T. Liu, B. Yao, M. Li, T. Kou, Z.-H. Huang, D.-Y. Feng, F. Wang, Y. Tong, X.-X. Liu, Y. Li. *ACS Energy Lett.* **2017**, *2*, 1752-1759.

48. S. Ardizzone, G. Fregonara, S. Trasatti. *Electrochim. Acta* **1990**, *35*, 263-267.

49. D. Baronetto, N. Krstajić, S. Trasatti. *Electrochim. Acta* **1994**, *39*, 2359-2362.

50. B. Yao, S. Chandrasekaran, J. Zhang, W. Xiao, F. Qian, C. Zhu, E. B. Duoss, C. M. Spadaccini, M. A. Worsley, Y. Li. *Joule* **2019**, *3*, 459-470.

51. Z. Fan, J. Jin, C. Li, J. Cai, C. Wei, Y. Shao, G. Zou, J. Sun. *ACS Nano* **2021**, *15*, 3098-3107.

52. P. Zhang, Y. Li, G. Wang, F. Wang, S. Yang, F. Zhu, X. Zhuang, O. G. Schmidt, X. Feng. *Adv. Mater.* **2019**, *31*, 1806005.

53. H. Xu, W. He, Z. Li, J. Chi, J. Jiang, K. Huang, S. Li, G. Sun, H. Dou, X. Zhang. *Adv. Funct. Mater.* **2022**, *32*, 2111131.

54. G. Nagaraju, S. Tagliaferri, A. Panagiotopoulos, M. Och, R. Quintin-Baxendale, C. Mattevi. *J. Mater. Chem. A* **2022**, *10*, 15665-15676.

55. Y. Xu, X. Chen, C. Huang, Y. Zhou, B. Fan, Y. Li, A. Hu, Q. Tang, K. Huang. *J. Power Sources* **2021**, *488*, 229426.

56. G. Sun, H. Yang, G. Zhang, J. Gao, X. Jin, Y. Zhao, L. Jiang, L. Qu. *Energy Environ. Sci.* **2018**, *11*, 3367-3374.

# Chapter 3 - 3D-Printed Graded Electrode with Ultrahigh $MnO_2$ Loading for Non-Aqueous Electrochemical Energy Storage


## Abstract

Electrolytic manganese dioxide is one of the promising cathode candidates for electrochemical energy storage devices due to its high redox capacity and ease of synthesis. Yet, high-loading $MnO_2$ often suffers from sluggish reaction kinetics, especially in non-aqueous electrolytes. The non-uniform deposition of $MnO_2$ on a porous current collector also makes it difficult to fully utilize the active materials at high mass loading. Here, a 3D printed graded graphene aerogel (3D GA) that contains sparsely separated exterior ligaments is developed to create large open channels for mass transport as well as densely arranged interior ligaments providing large ion-accessible active surface. The unique structural design homogenizes the thickness of electro deposited $MnO_2$ even at an ultrahigh mass loading of ≈70 mg $cm^{-2}$. The electrode achieves a remarkable volumetric capacity of 29.1 mA h $cm^{-3}$ in the non-aqueous electrolyte. A Li-ion hybrid capacitor device assembled with a graded 3D GA/$MnO_2$ cathode and graded 3D GA/$VO_x$ anode exhibits a wide voltage window of 0-4 V and a superior volumetric energy density of 20.2 W h $L^{-1}$. The findings offer guidance on 3D printed electrode design for supporting ultrahigh loading of active materials and developments of high energy density energy storage devices.

## 3.1 Introduction

The capability to deliver plenty of electrical energy within a compact device configuration is one of the major pursuits of many electrochemical energy storage devices, such as portable batteries, on-chip micro-supercapacitors, power supplies of electric vehicles, etc.[1-7] Such capability can be quantified by volumetric energy density, which is determined by the volumetric capacity (charge delivered per volume) and the output voltage of the device according to the following equation:

$$E_{\mathrm{V}} = \frac{\int_0^q U(q)dq}{V} = \frac{\int_0^U q(U)dU}{V} \tag{3.1}$$

where $E_{\mathrm{V}}$ is the volumetric energy density (mW h $cm^{-3}$ or W h $L^{-1}$), $q$ is the device output charge (mA h), $U$ is the device output voltage, and $V$ is the device volume ($cm^3$).[6,8] Electrodes featuring high volumetric capacities and high cathodic/low anodic operating potentials are keys to achieving outstanding volumetric energy density at the device level.[6,9]

Among numerous candidate electrode materials, electrolytic manganese dioxide ($MnO_2$) has been frequently reported as a cathode that can achieve ultrahigh areal mass loading through facile electrodeposition techniques and deliver high volumetric capacity for aqueous supercapacitors and batteries.[10-14] Yet, to increase the device output voltage, stable non-aqueous electrolytes are preferable to aqueous electrolytes, which typically limit the output voltages to less than 2 V because of the water-splitting reaction.[15-19] Therefore, the coupling of ultrahigh-loading electrolytic $MnO_2$ cathodes and non-aqueous electrolytes is logical and promising for achieving

high volumetric energy density. Unfortunately, the electrochemical performance of $MnO_2$ decreases rapidly with the increase of mass loading (i.e., thick $MnO_2$ layers) because of its intrinsically low electrical conductivity, sluggish ion diffusion and conduction in the non-aqueous electrolyte, and slow kinetics of the dominant aprotic redox reactions (e.g., $Li^+$ ion insertion/desertion).[20-22]

Recently, the concept of conductive 3D-printed lattice current collectors has been proven to enable efficient electron transport and ion diffusion of ultrahigh-loading of $MnO_2$ for energy-dense aqueous supercapacitors.[10,11] A 3D-printed graphene aerogel (3D GA) scaffold with orthogonal lattice structure and ordered large channels was able to support $MnO_2$ at an unprecedented loading level of hundreds mg $cm^{-2}$ while maintaining high gravimetric capacitance, volumetric capacitance and rate capability at electrode thicknesses up to few millimeters. [10] This excellent performance was attributed to the good electrical conductivity of the interconnected network of the 3D GA, and efficient ion transport benefiting from the low-tortuosity porous architecture. This strategy simultaneously enhances the accessibility of ultrahigh-loading $MnO_2$ to electrons and electrolyte ions compared to the conventional planar $MnO_2$ electrodes. Here, we extend this concept to non-aqueous energy storage systems by further optimizing the electrode architecture to improve the uniformity of $MnO_2$ deposition and to promote $MnO_2$ accessibility during charge/discharge.

We develop a modified 3D GA substrate with a graded porous structure (Figure 3.1). The center-to-center ligament spacing of the graded structure gradually decreases from the outer layer to the inner layer, in contrast to the conventional non-graded lattice

that has a fixed center-to-center ligament spacing. The gradient porous design facilitates ion/electrolyte diffusion throughout the entire GA for achieving uniform electrodeposition of $MnO_2$. At ultrahigh $MnO_2$ loadings (up to ≈70 mg $cm^{-2}$), the 3 mm thick graded 3D GA/$MnO_2$ composite electrode delivers an excellent volumetric capacity of 29.1 mA h $cm^{-3}$ at a high current density of 20 mA $cm^{-2}$ in the non-aqueous electrolyte, outperforming other previously reported 3D printed and/or high-$MnO_2$-loaded thick cathodes. The graded scaffold also considerably improves the high-rate capacity retention compared to the non-graded counterpart, due to the uniform deposition of $MnO_2$ in 3D structure and enhanced $MnO_2$ accessibility. A non-aqueous lithium-ion hybrid capacitor fabricated by a 3D-graded $MnO_2$ cathode and a 3D-graded mixed-valence vanadium oxide ($VO_x$) anode achieves a wide voltage window of 4 V and an excellent volumetric energy density of 20.2 W h $L^{-1}$. Structural optimization offers new opportunities for homogenizing the thickness of electrodeposited high-loadings of active materials on thick and porous substrates as well as improving the rate performance of high-energy-density electrochemical energy storage systems.

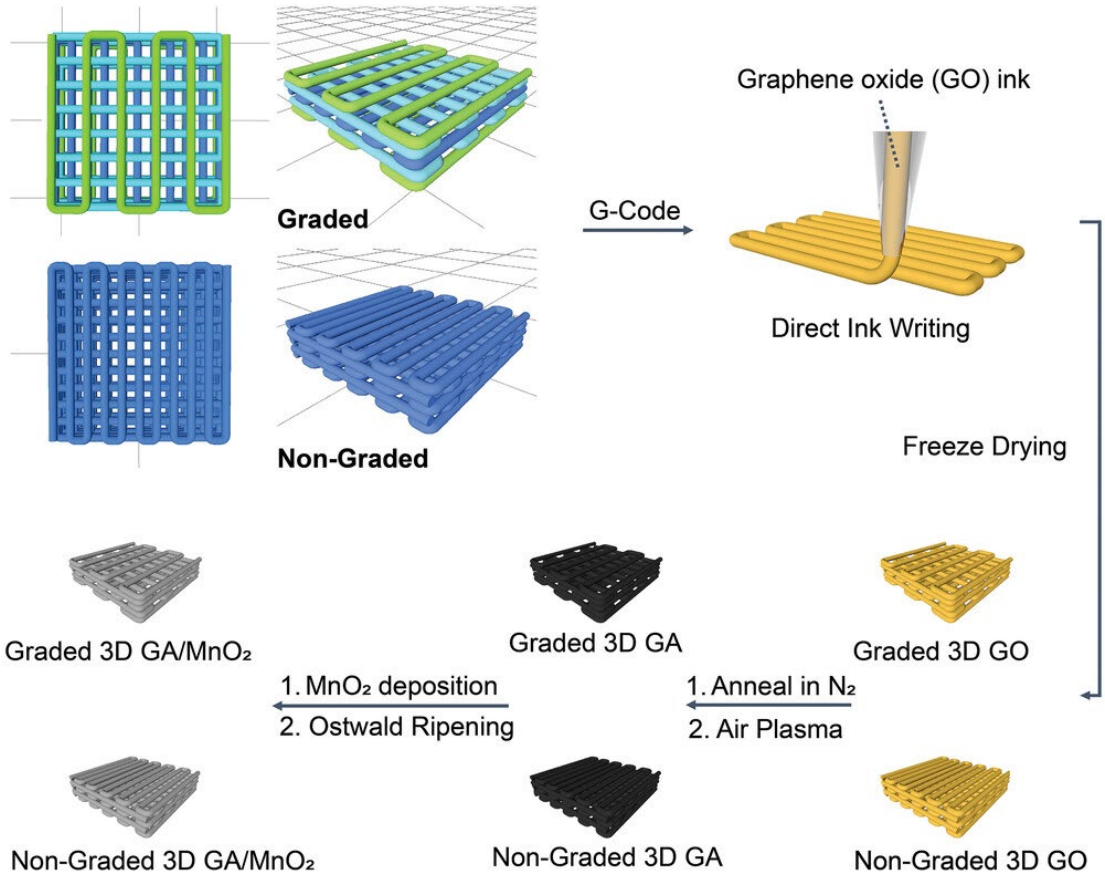


**Figure 3.1** Schematic illustration of the fabrication process of non-graded and graded 3D GA/$MnO_2$ composite electrodes.

## 3.2 Experimental Section

### Ink Preparation

Single-layer graphene oxide sheets (GO) having a lateral dimension of 300-800 nm purchased from Cheaptubes Inc. were used to prepare the aerogel inks. The GO suspension was prepared by ultra-sonicating 0.8 g of GO in 20 g of water for 24 h in a temperature-controlled sonication bath. This combination yielded a GO concentration

of 40 mg $ml^{-1}$. The suspension was then mixed with 5 wt.% of hydroxypropyl methylcellulose (from DOW chemicals) GO-ink in a planetary Thinky mixer at 2000 rpm until the cellulose was fully mixed without any agglomerates.

**Printing of Graphene Oxide**

The ink was loaded into a 10 ml syringe barrel (EFD) and centrifuged for a minute at 4500 rpm to remove air bubbles, after which the ink was extruded through a micro nozzle (200 μm diameter) to pattern 3D structures on a glass substrate. For direct ink writing, the syringe was attached by a luer-lock to a smooth-flow tapered nozzle whose inner diameter(d) is 200 μm. The ink was then extruded by means of an air-powered fluid dispenser (Ultimus V, EFD) which provided an appropriate pressure (in the range of 18-30 psi) for writing, and the writing speed was kept at 10 mm sec-1 for all the 3D printed structures. Although it was not mandatory to change the PTFE nozzle tip between the prints, for the fabrication of electrodes, a new tip was used for every sample.

Two types of simple cubic lattices, namely non-graded and graded structures, were printed on a glass substrate by varying the spacing between the ligaments. For the non-graded sample, a simple cubic lattice with multiple orthogonal layers of parallel cylindrical rods was printed alternately. The diameter of the cylindrical rods equaled the diameter of the nozzle and the center-to-center rod spacing of 0.4 mm (for 200 μm nozzle). The height of the electrodes was set at 2.21 mm (18 layers) and the layers were stacked on the structure such that each layer had a z-spacing of 0.12 mm. For the graded simple cubic lattice, multiple orthogonal layers of parallel cylindrical rods were printed

alternately using a 200 μm nozzle with similar z-spacing but the layer spacing after every 2 layers gradually decreased to a minimum and then gradually increased as the structure was built. The first 2 layers had a center-to-center rod spacing of 1.2 mm, followed by 1.0 mm spacing (layers 3 and 4), 0.8 mm (layers 5 and 6), 0.6 mm (layers 7 and 8), and 0.4 mm (layers 9 and 10). After which, the spacing gradually increased from 0.4 to 1.2 mm every 2 layers till the top. To avoid cracking or drying due to evaporation of water, soon after printing, the 3D printed structures were immersed in liquid nitrogen and freeze-dried for 48 h in vacuum.

**Synthesis of 3D Graphene Aerogel**

The 3D printed graphene oxide aerogels were subjected to a heat treatment process where the samples were first annealed in air at 240 °C and later pyrolyzed in a tube furnace under nitrogen atmosphere at 1000 °C for 1 h with a heating rate of 0.5 °C $min^{-1}$ to form graphene aerogels. To further improve the wettability of the aerogels for electrodeposition, the samples were treated in air plasma for 4 min using a Harrick basic plasma cleaner with adjustable RF power. The final dimension of the aerogel was 1.0 cm × 1.0 cm × 0.18 cm.

**Electrodeposition of $MnO_2$**

$MnO_2$ nanosheets were electrodeposited on the 3D printed graphene aerogel substrates in a two-electrode electrolytic cell using 0.1 M manganese acetate aqueous solution as the electrolyte and carbon paper as the counter electrode. Before electrodeposition, the graphene aerogel substrates were immersed in the electrolyte and

degassed in a vacuum chamber until no bubble was formed. A pulse technique was used for electrodeposition, a repetitive cycle of which consisted of electrodeposition with a constant current density of 10 mA $cm^{-2}$ for 60 s followed by an open circuit (rest) period of 10 s. The electrolyte was also constantly stirred using a magnetic stir bar and a stir plate during the deposition process. The degassing process, the pulse electrodeposition, and the constant stirring allowed sufficient ion supply to all accessible substrate surfaces for homogeneous deposition. After electrodeposition, the 3D GA/$MnO_2$ composite material was washed with deionized water. An Ostwald ripening procedure was consequently conducted by hydrothermally treating the 3D GA/$MnO_2$ composite material in a 25 mL Teflon-lined stainless-steel autoclave filled with 20 mL deionized water at 90 °C. The sample was then vacuum dried at room temperature overnight. The prepared samples were denoted as 3D GA/$MnO_2$-x, where x represented the number of pulse cycles (total minutes) of electrodeposition. The duration of the hydrothermal treatment for 3D GA/$MnO_2$-60, 3D GA/$MnO_2$-120, and 3D GA/$MnO_2$-180 are 40, 80, and 120 min, respectively. The $MnO_2$ mass loading of non-graded 3D GA/$MnO_2$-60, 3D GA/$MnO_2$-120, and 3D GA/$MnO_2$-180 was 24.0, 47.2 and 68.7 mg $cm^{-2}$, respectively. The $MnO_2$ mass loading of graded 3D GA/$MnO_2$-60, 3D GA/$MnO_2$-120, and 3D GA/$MnO_2$-180 was 22.7, 47.3 and 67.7 mg $cm^{-2}$, respectively.

**Fabrication of Three-Electrode Cells**

The three-electrode cell for electrochemical tests of electrodes was fabricated in a 10 mL beaker cell with the working electrode held by a Pt electrode holder, a piece

of carbon paper as the counter electrode, a Pt wire as the pseudo-reference electrode, and 5 mL 1 M $LiClO_4$/acetonitrile solution as the electrolyte. The beaker cell was sealed to avoid the evaporation of acetonitrile during tests. All the electrolyte preparations, cell fabrications, and electrochemical tests were conducted in a glovebox filled with dry Ar. The electrochemical tests were conducted using a BioLogic EC-Lab SP-300 electrochemical workstation.

**Electrodeposition of $VO_x$**

Mixed-valence vanadium oxide ($VO_x$) was electrodeposited on the graded 3D printed graphene aerogel substrates in a three-electrode electrolytic cell with 0.1 M of vanadium (IV) oxide sulfate hydrate + 0.2 M ammonium acetate aqueous solution mixture as the electrolyte, a piece of ring-shaped carbon cloth surrounding the working electrode as the counter electrode, and saturated calomel electrode (SCE) as the reference electrode. Before electrodeposition, the graphene aerogel substrates were immersed in the electrolyte and degassed in a vacuum chamber until no bubble was formed. A pulse cyclic voltammetry was used for electrodeposition, a repetitive cycle of which consisted of scanning from -1.5 to 1.5 back to -1.5 V versus SCE at 20 mV $s^{-1}$ followed by an open circuit (rest) period of 10 s. After 60 pulse cycles, the as-prepared vanadium oxide was further reduced under a constant potential of -1.5 V versus SCE for 2 min in the same electrolyte to introduce lower-valence vanadium, yielding the graded 3D GA/$VO_x$ composite electrode. The electrolyte was constantly stirred using a magnetic stir bar and a stir plate. After electrodeposition, the sample was washed with

deionized water and vacuum dried at room temperature overnight. The $VO_x$ mass loading was 36.0 mg $cm^{-2}$.

**Fabrication of Lithium-Ion Hybrid Capacitor Devices**

The lithium-ion hybrid capacitor device was fabricated in a 10 mL beaker cell with the graded 3D GA/$VO_x$ as a negative electrode, the graded 3D GA/$MnO_2$ as a positive electrode, and 5 mL 1 M $LiClO_4$/acetonitrile solution as the electrolyte. Both electrodes have an area of 0.2 $cm^2$ for charge balancing. Before assembling into the full device, both electrodes were individually activated to charged state in a three-electrode cell using cyclic voltammetry by scanning at 5 mV $s^{-1}$ for 3 cycles (0 to -2.6 V vs Pt for $VO_x$, and -0.8 to 1.4 V vs Pt for $MnO_2$). The beaker cell was sealed to avoid the evaporation of acetonitrile during tests. All the electrolyte preparations, cell fabrications, and electrochemical tests were conducted in a glovebox filled with dry Ar. The electrochemical tests were conducted using a BioLogic EC-Lab SP-300 electrochemical workstation.

**Characterizations**

The SEM images of the samples were obtained by a field emission SEM (FEI Quanta 3D FEG dual beam) to investigate the surface morphologies. A powder X-ray diffractometer (Rigaku D-MAX 2200 VPC) was used to collect the XRD spectra of the samples. Diffraction spectra were recorded from a 2θ angle of 10-70°, with a step size of 0.01° at a rate of 0.1° $min^{-1}$. The elemental composition of the samples was analyzed

by an XPS spectrometer (Thermo Scientific Nexsa G2) with an Al Kα X-ray source. The frequency range of electrochemical impedance spectroscopy was $10^{-2}$-$10^{6}$ Hz.

**Micro-CT**

Tomography scans were performed on desktop laboratory micro-computed tomography scanner SkyScan 1272 (Bruker, Billerica, MA, USA) equipped with Hamamatsu L10101-67 (Hamamatsu Photonics, Shizuoka, Japan) X-ray source and XIMEA xiRAY16 (Ximea GmbH, Münster, Germany) detector. The camera sensor had a 4904 × 3280 resolution with a 7.4-pixel size. All scans were done with source voltage and current tuned to 72 kV and 40 µA respectively. Camera-to-source and object-to-source distances were set to 274.8 and 55.7 mm respectively, resulting in projections with an effective pixel size of 1.5 µm. A total of 900 projections were collected over a 180° range.

Reconstructions were done using the standard filter back-projection algorithm of LTT (Livermore Tomography Tools, 1.6.38).[23] Reconstructed images were converted from 32-bits to 8-bits by scaling intensity (add 2 then multiply by 40) and analyzed both in 2D and 3D using Fiji (ImageJ 1.53t).[24]

**Trasatti Capacity Contribution Analysis**

The gravimetric capacities ($Q_{\mathrm{G,CV}}$) at different scan rates were first calculated from cyclic voltammetry (CV) curves using Equation 3.2.

$$Q_{\mathrm{G,CV}} = \frac{S_{\mathrm{CV}}}{2v} \tag{3.2}$$

where $S_{CV}$ is the area enclosed by the CV curve (A V $g^{-1}$) and $v$ is the scan rate (V $s^{-1}$). By assuming a semi-finite ion diffusion, a linear dependence of $Q_{G,CV}$ vs. $v^{-1/2}$ can be drawn at slow scan rates (1-5 mV $s^{-1}$). Due to the intrinsic electrical resistance of the electrode, the capacities calculated at high scan rates showed deviation from the linear trend, and thus were not included in the linear fitting. The y-intercept ($v \rightarrow +\infty$) of the extrapolated fitting line should represent the kinetically fast $Q_{surface}$ as capacities with relatively slow kinetic should be absent when $v \rightarrow +\infty$. Since $Q_{G,CV}$ at each scan rate is a sum of $Q_{surface}$ and $Q_{bulk}$, the percentage of capacity contribution from both $Q_{surface}$ and $Q_{bulk}$ can therefore be calculated.

**Calculations**

The gravimetric capacity ($Q_G$) and volumetric capacity ($Q_V$) of single electrodes were calculated based on the galvanostatic charging and discharging tests using Equation 3.3 and Equation 3.4, respectively.

$$Q_G = \frac{Q_{dis}}{m} \tag{3.3}$$

$$Q_V = \frac{Q_{dis}}{Ad} \tag{3.4}$$

where $Q_G$ and $Q_V$ are the gravimetric and volumetric capacities (mA h $g^{-1}$ and mA h $cm^{-3}$, respectively), $Q_{dis}$ is the discharging capacity (mA h) obtained from the galvanostatic discharging voltage profile of the single electrode, $m$ is the mass loading of the active material on the electrode (g), $A$ is the geometric electrode working area ($cm^2$), and $d$ is the thickness of the electrode (cm).

The gravimetric capacitance ($C_G$) and volumetric capacitance ($C_V$) of the lithium-ion hybrid capacitor device was calculated based on the galvanostatic charging and discharging tests using Equation 3.5 and Equation 3.6, respectively.

$$C_G = \frac{3600 \times Q_{dis}}{1000 \times \Delta U \times M} \tag{3.5}$$

$$C_V = \frac{3600 \times Q_{dis}}{1000 \times \Delta U \times V} \tag{3.6}$$

where $C_G$ and $C_V$ are the gravimetric and volumetric capacitances (F $g^{-1}$ and F $cm^{-3}$, respectively), $Q_{dis}$ is the discharging capacity (mA h) obtained from the galvanostatic discharging voltage profiles of the device, $\Delta U$ is the potential window (V) excluding the *iR* drop, $M$ is the total mass loading of the active materials on both electrodes (g), and $V$ is the total volume of both electrodes with active materials ($cm^3$).

The gravimetric capacity ($Q_G$) and volumetric capacity ($Q_V$) of the lithium-ion hybrid capacitor device was calculated based on the galvanostatic charging and discharging tests using Equation 3.7 and Equation 3.8, respectively.

$$Q_G = \frac{Q_{dis}}{M} \tag{3.7}$$

$$Q_V = \frac{Q_{dis}}{V} \tag{3.8}$$

where $Q_G$ and $Q_V$ are the gravimetric and volumetric capacities (mA h $g^{-1}$ and mA h $cm^{-3}$, respectively), $Q_{dis}$ is the discharging capacity (mA h) obtained from the galvanostatic discharging voltage profile of the device, $M$ is the total mass loading of the active materials on both electrodes (g), and $V$ is the total volume of both electrodes with active materials ($cm^3$).

The volumetric energy density ($E_V$, W h $L^{-1}$) and power density ($P_V$, W $L^{-1}$) of the lithium-ion hybrid capacitor device were calculated using the following equations:

$$E_V = \frac{Q_{dis} \times \Delta U}{2V} \tag{3.9}$$

$$P_V = \frac{3600 \times E_V}{t_{dis}} \tag{3.10}$$

where $Q_{dis}$ is the discharging capacity (mA h) obtained from the galvanostatic discharging voltage profiles of the device, $\Delta U$ is the potential window (V) excluding the $iR$ drop, $t_{dis}$ is the discharging time (s) in the galvanostatic discharging test, and $V$ is the total volume of both electrodes with active materials ($cm^3$).

## 3.3 Results and Discussion

### Preparation of Graded 3D GA

Figure 3.1 illustrates the fabrication process of the non-graded and graded 3D GA/$MnO_2$. The conventional non-graded structure was constructed by a simple cubic lattice with multiple orthogonal layers of parallel cylindrical rod ligaments. [10,11] The diameter of the cylindrical rods is set to 200 μm and the center-to-center rod spacing is 0.4 mm for each of the total 18 layers. Therefore, the size of the open channels is constantly 200 μm × 200 μm throughout the entire z-direction. The layer projections overlap with each other. For the graded simple cubic lattice, the orthogonal layers are also composed of parallel cylindrical rods with a diameter of 200 μm, while the layer spacing of every 2 layers gradually decreases to a minimum and then gradually increases from bottom to top. Specifically, the first 2 layers have a center-to-center rod

spacing of 1.2 mm, followed by 1.0 mm spacing (layers 3 and 4), 0.8 mm (layers 5 and 6), 0.6 mm (layers 7 and 8), and 0.4 mm (layers 9 and 10). Subsequently, the spacing gradually increases from 0.4 to 1.2 mm every 2 layers till the top. Such a graded structure was designed with the intention that the open channels at the exterior domains (top and bottom surface layers) would allow for maximum ion flux, while the densely placed cylindrical rods at the interior domains (center layers) would provide an enlarged available surface for electrochemical processes. Moreover, we anticipated that the cylindrical rods in the interior of the graded structure would be more exposed than those of the non-graded structure due to the reduced overlap of layer projections.

After generating G-codes from the models, the 3D structures were printed using the direct ink writing technique, where the aqueous ink contained single-layer graphene oxide (GO) sheets suspension (40 mg $mL^{-1}$) mixed with 5% hydroxypropyl methylcellulose and was extruded through a 200 μm nozzle. The 3D-printed GO structures were first freeze-dried and then annealed in a nitrogen atmosphere at 1050°C to convert GO to graphene. The samples were further air plasma treated for better wettability and $MnO_2$ affinity. The resultant 3D GA samples have a reasonably low mass density of ≈33 mg $cm^{-3}$. As shown in Figure 3.2, the parallel cylindrical rods composing each orthogonal layer of the printed lattice structure have a diameter of 200 μm, a porous morphology of interconnected graphene sheets, and a gradual variation of the center-to-center rod spacing, as designed. The surface of rods even in the inner layers is visible from the top view, ensuring higher accessibility for electrolytes and ions. On the contrary, the cylindric rods on each layer of non-graded 3D GA were

stacked together with a fixed center-to-center spacing of 0.4 mm, forming narrow open channels and overshadowing the rods beneath Figure 3.3.

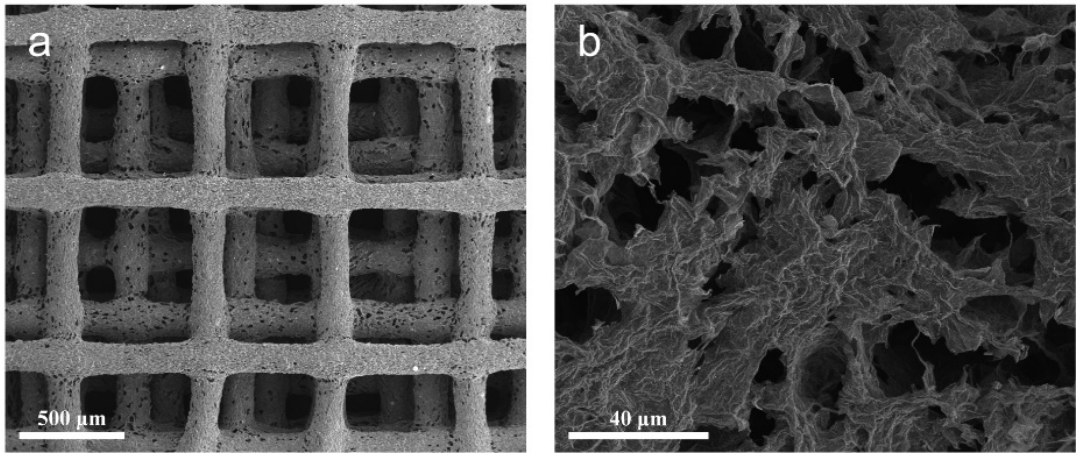


**Figure 3.2** SEM images of graded 3D GA.

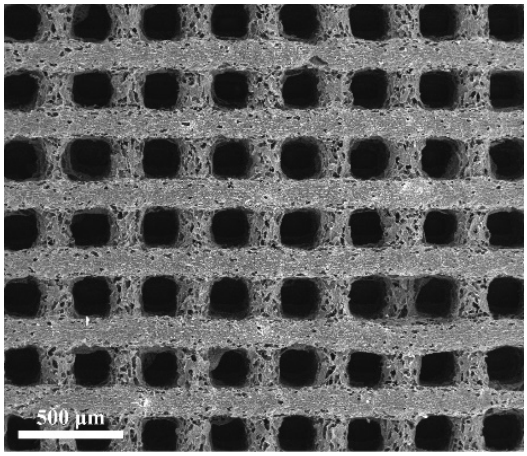


**Figure 3.3** SEM images of non-graded 3D GA.

**Preparation of Graded 3D GA/$MnO_2$**

Subsequently, $MnO_2$ nanosheets were pulse-electrodeposited onto the 3D GA substrates followed by an Ostwald ripening treatment to obtain the composite electrode (3D GA/$MnO_2$). The Ostwald ripening treatment was reported to be useful in improving the $MnO_2$ electrical conductivity and facilitating the ion transfer in $MnO_2$.[12] The $MnO_2$ mass loadings obtained at different numbers of pulse electrodeposition cycles are depicted in Table 3.1. After 60 pulse cycles, the obtained graded 3D GA/$MnO_2$-60 reached a high $MnO_2$ mass loading of 22.7 mg $cm^{-2}$. Significantly, the deposited $MnO_2$ nanosheets are conformally coated on the cylindric rods including the interior layers, inheriting the porous morphology of the underlying 3D GA substrate (Figures 3.4a and 3.5). X-ray diffraction (XRD) and X-ray photoelectron spectroscopy (XPS) results confirmed the nanosheets are ε-$MnO_2$ (Figures 3.6 and 3.7). [10,12] The $MnO_2$ mass loading also increases linearly with the number of pulse electrodeposition cycles. The graded electrodes prepared by 120 (3D GA/$MnO_2$-120) and 180 (3D GA/$MnO_2$-180) cycles achieve ultrahigh $MnO_2$ loadings of 47.3 and 67.7 mg $cm^{-2}$, respectively. As shown in Figures 3.4b and 3.4c, these samples also maintain a conformal $MnO_2$ coating. Notably, the thickening of $MnO_2$ layers does not block the open channels, retaining good accessibility to the interior of the 3D GA scaffold. In contrast, the non-graded 3D GA/$MnO_2$ samples suffered from severe shrinkage of open channels due to excess coating of $MnO_2$ on the scaffold's exterior surface (Figure 3.8). Non-destructive micro-computed tomography (micro-CT) was employed to visualize the distributions of $MnO_2$ deposits on the ligaments along the *z*-direction (Figures 3.4d-f and 3.9). The bright contrast region represents the $MnO_2$ coating on the scaffold

surface. The coating thickness increases with the number of pulse electrodeposition cycles (mass loading) for both non-graded and graded samples. For graded 3D GA/$MnO_2$ samples, uniform $MnO_2$ coatings can be clearly observed even on the surface of middle layers (Figures 3.4d-f), suggesting the surface of these interior ligaments is readily accessible by $Mn^{2+}$ ions during electrodeposition. On the contrary, the $MnO_2$ signal is relatively weak in the interior domains of the non-graded 3D GA/$MnO_2$ (Figure 3.9) and indicated that most $MnO_2$ was deposited on the exterior surface of the GA substrate (edges of the cross-section image). These results confirm the critical role of open channels of the graded structure in improving the uniformity of deposited $MnO_2$ by allowing efficient transport of ions into the interior part of the 3D GA substrate during electrodeposition. In the meantime, the densely packed interior structure guarantees a large electrochemically active surface area for supporting high loading of $MnO_2$.

**Table 3.1** Summary of synthesis conditions and mass loadings of non-graded and graded 3D GA/$MnO_2$.

| **$MnO_2$ Deposition Cycles** | **Ostwald Ripening Time / min** | **Mass Loading / mg $cm^{-2}$** | |
|---|---|---|---|
| | | Non-Graded | Graded |
| 60 | 40 | 24.0 | 22.7 |
| 120 | 80 | 47.2 | 47.3 |
| 180 | 120 | 68.7 | 67.7 |

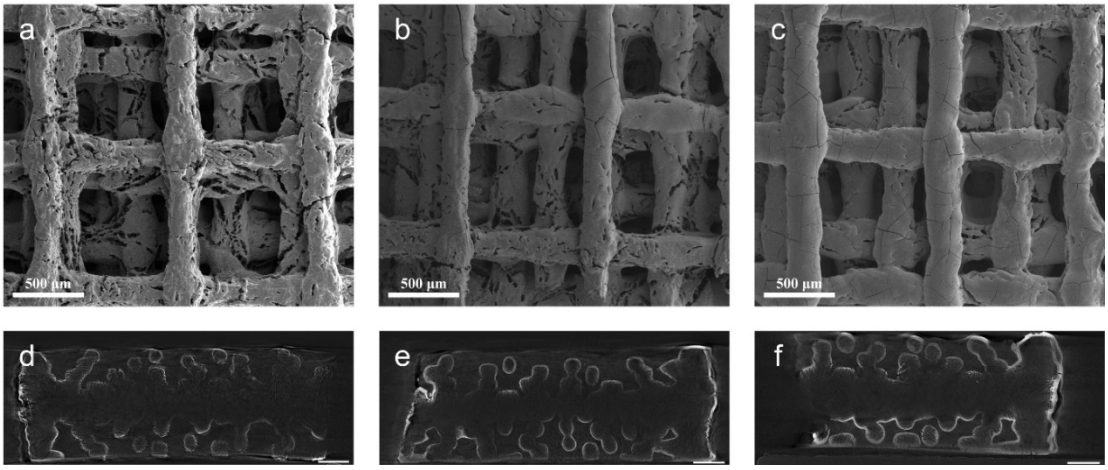


**Figure 3.4** Top-view SEM images of (a) graded 3D GA/$MnO_2$-60 (22.7 mg $cm^{-2}$), (b) graded 3D GA/$MnO_2$-120 (47.3 mg $cm^{-2}$), and (c) graded 3D GA/$MnO_2$-180 (67.7 mg $cm^{-2}$). Side-view cross-section micro-CT images of (d) graded 3D GA/$MnO_2$-60, (e) graded 3D GA/$MnO_2$-120, and (f) graded 3D GA/$MnO_2$-180. Scale bars of CT images are 500 µm.

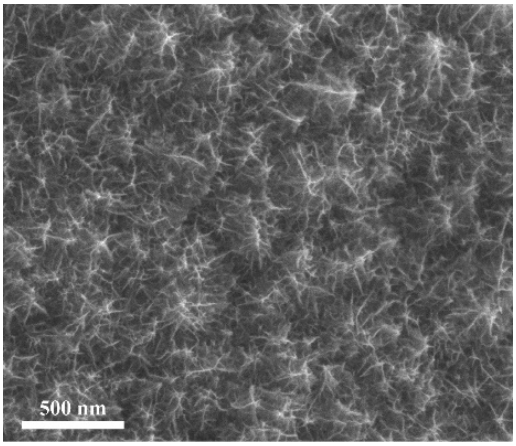


**Figure 3.5** SEM image of $MnO_2$ nanosheets of graded 3D GA/$MnO_2$-60.

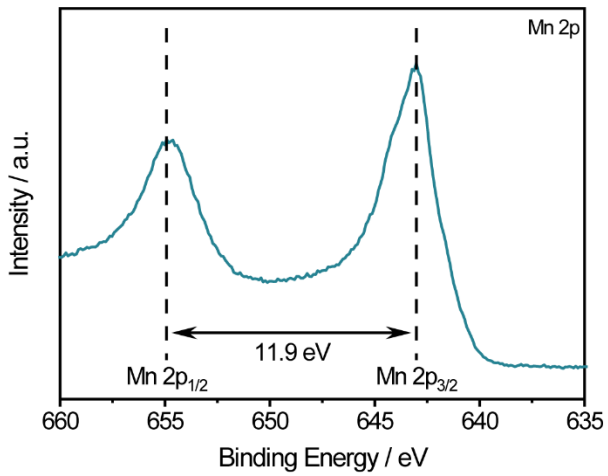


**Figure 3.6** Mn 2p XPS spectra of graded 3D GA/$MnO_2$-60, which shows the $MnO_2$ characteristic spin-energy separation of 11.9 eV between Mn $2p_{1/2}$ (654.9 eV) and Mn $2p_{3/2}$ (643.0 eV).

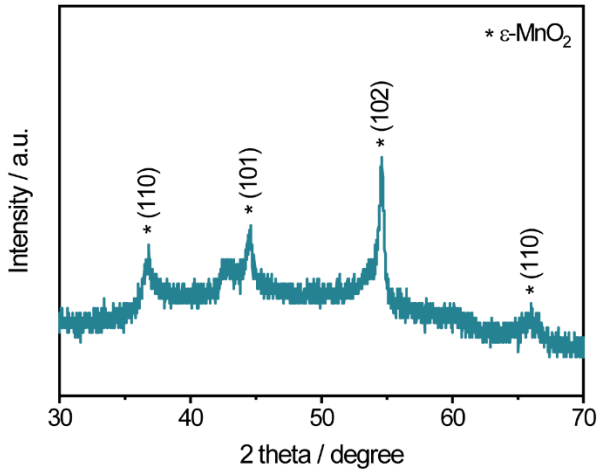


**Figure 3.7** XRD spectra of graded 3D GA/$MnO_2$-60. The marked peaks are correspondent to ε-$MnO_2$ (JCPDS 30-0820).

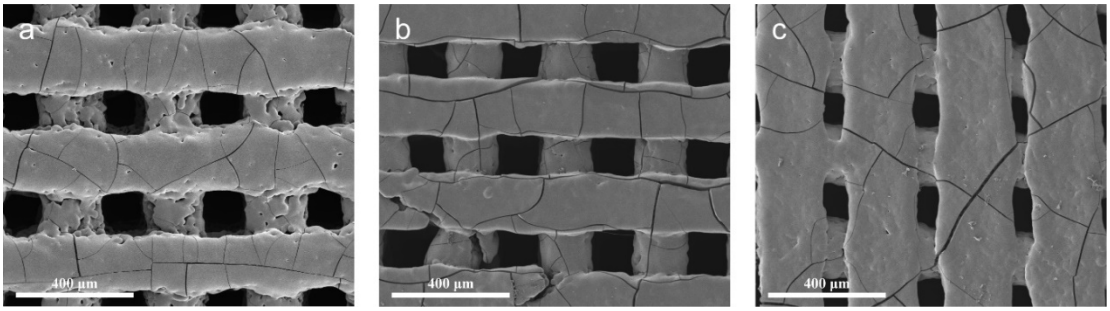


**Figure 3.8** Top-view SEM images of (a) non-graded 3D GA/$MnO_2$-60 (24.0 mg $cm^{-2}$), (b) non-graded 3D GA/$MnO_2$-120 (47.2 mg $cm^{-2}$), and (c) non-graded 3D GA/$MnO_2$-180 (68.7 mg $cm^{-2}$).

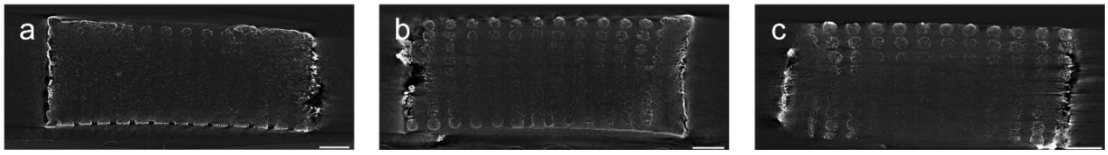


**Figure 3.9** Side-view cross-section micro-CT images of (a) non-graded 3D GA/$MnO_2$-60 (24.0 mg $cm^{-2}$), (b) non-graded 3D GA/$MnO_2$-120 (47.2 mg $cm^{-2}$), and (c) non-graded 3D GA/$MnO_2$-180 (68.7 mg $cm^{-2}$). Scale bars are 500 µm. /

**Electrochemical Performances of Graded 3D GA/$MnO_2$**

The electrochemical performance of both non-graded and graded 3D GA/$MnO_2$ with different $MnO_2$ loadings was evaluated in a non-aqueous 1 M $LiClO_4$/acetonitrile electrolyte using a three-electrode system under a dry Ar atmosphere. The galvanostatic charge/discharge (GCD) voltage profiles are illustrated in Figures 3.10a, 3.11, and 3.12. In contrast to the limited voltage windows (typically 0.8-1.2 V) in aqueous electrolytes, the use of Li-ion-based non-aqueous electrolytes effectively expands the stable voltage

window to 2.2 V (-0.8~1.4 V vs Pt). Redox reactions can take place in this wide voltage window, such as:

$$MnO_2 + xLi^+ + xe^- \leftrightarrow Li_xMnO_2 \quad (3.11)$$

where *x* represents the number of moles of Li ions and electrons involved in the $Li^+$ intercalation (discharge) and de-intercalation (charge) reactions.[20] The charge/discharge curves with nearly constant slopes indicate a capacitor-battery hybrid behavior. Figure 3.10b shows the volumetric capacities of graded 3D GA/$MnO_2$ with different $MnO_2$ loadings obtained at different rates. Benefiting from the high materials loading capability and improved ion transport provided by the 3D GA scaffold, the graded 3D GA/$MnO_2$ electrodes can operate at a range of ultrahigh areal current densities of 20-100 mA $cm^{-2}$, resulting in remarkable volumetric capacities up to 29.1 mA h $cm^{-3}$ at the current density of 20 mA $cm^{-2}$. Note that the volumetric capacity increases with the mass loading, indicating unimpeded ion transport even at high mass loadings and high rates. Importantly, despite the graded 3D GA having less surface area (less printed ligaments) per unit volume for $MnO_2$ electrodeposition, the maximum volumetric capacities at 20 mA $cm^{-2}$ with different loadings are comparable to those of non-graded 3D GA/$MnO_2$ electrodes (Figure 3.13). The obtained volumetric capacities are higher than the values reported for most 3D printed and/or high-$MnO_2$-loaded thick cathodes (Figure 3.10c and Table 3.2). [10,12,25-34] It is noteworthy that these volumetric capacities were achieved at an outstanding current density (20 mA $cm^{-2}$ or ≈0.3 A $g^{-1}$), which is also among the highest in previous studies (Table 3.2). Finally, the graded 3D GA/$MnO_2$-180 retained 86.4% of capacity after 1000 charge/discharge cycles at 100

mA $cm^{-2}$ without noticeable morphological change (Figures 3.14 and 3.15), reflecting its good potential for practical applications.

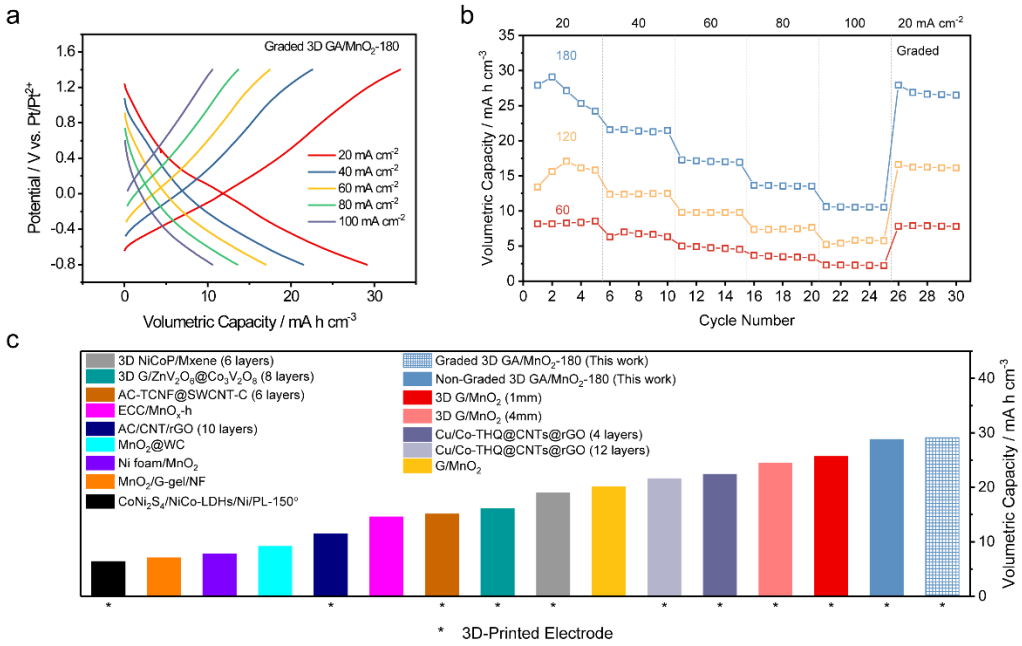


**Figure 3.10** (a) GCD voltage profiles of graded 3D GA/$MnO_2$-180 (67.7 mg $cm^{-2}$). (b) Volumetric capacity retention of graded 3D GA/$MnO_2$ obtained at different current densities. (c) A plot compares the volumetric capacity of non-graded 3D GA/$MnO_2$-180 (68.7 mg $cm^{-2}$) and graded 3D GA/$MnO_2$-180 (67.7 mg $cm^{-2}$) with the values of previously reported for 3D printed and/or high-$MnO_2$-loaded thick cathodes.[10,12,25-34]

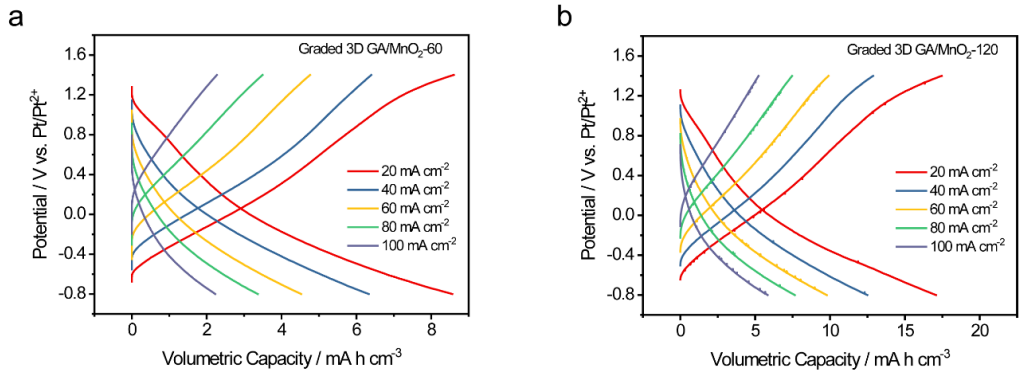


**Figure 3.11** GCD voltage profiles of (a) graded 3D GA/$MnO_2$-60 (22.7 mg $cm^{-2}$) and (b) graded 3D GA/$MnO_2$-120 (47.3 mg $cm^{-2}$).

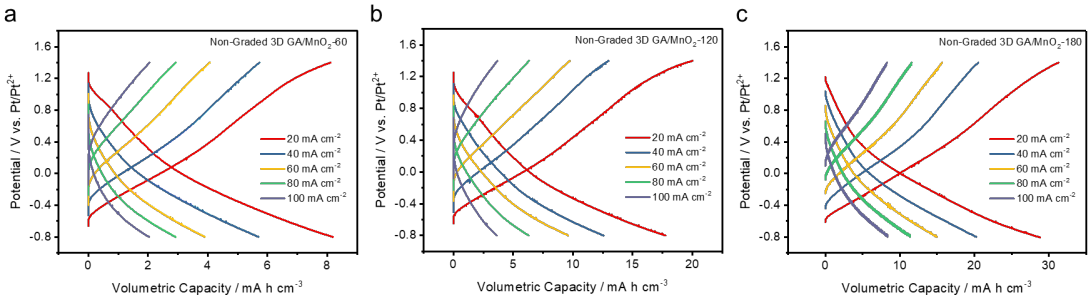


**Figure 3.12** GCD voltage profiles of (a) non-graded 3D GA/$MnO_2$-60 (24.0 mg $cm^{-2}$), (b) non-graded 3D GA/$MnO_2$-120 (47.2 mg $cm^{-2}$), and (c) non-graded 3D GA/$MnO_2$-180 (68.7 mg $cm^{-2}$).

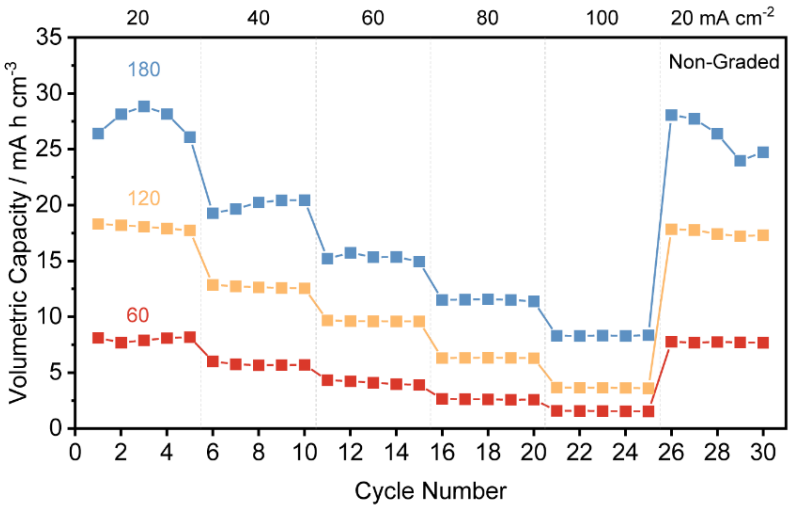


**Figure 3.13** Volumetric capacity retention of non-graded 3D GA/$MnO_2$ obtained at different current densities.

**Table 3.2** Summary of mass loading, thickness, volumetric capacity and corresponding current density/scan rate of 3D printed and/or high-$MnO_2$-loaded thick cathodes. Samples reported in this work are highlighted in blue text.

| **Electrode** | **Mass Loading / mg cm$^{-2}$** | **Thickness / mm** | **$Q_v$ / mA h cm$^{-3}$** | ***j* or *v*** | **Electrolyte** |
|---|---|---|---|---|---|
| $CoNi_2S_4$/Ni Co-LDHs/Ni/PL-150°[34] | 1.2 | 3 | 6.4 | 10 mA cm$^{-3}$ | 6 M KOH (aq.) |
| $MnO_2$/G-gel/NF[33] | 13.6 | 1 | 7.1 | 1 mV s$^{-1}$ | 0.5 M $Na_2SO_4$ (aq.) |
| Ni foam/$MnO_2$ [32] | 18 | 0.5 | 7.8 | 2 mA cm$^{-2}$ | 1 M $Na_2SO_4$ (aq.) |
| $MnO_2$@WC[31] | 75 | 1 | 9.2 | 1 mA cm$^{-2}$ | 1 M $Na_2SO_4$ (aq.) |

| Electrode | Mass Loading / mg $cm^{-2}$ | Thickness / mm | $Q_v$ / mA h $cm^{-3}$ | *j* or *v* | Electrolyte |
|---|---|---|---|---|---|
| AC/CNT/rGO (10 layers)[30] | 56.9 | 2.2 | 11.5 | 10 mV $s^{-1}$ | 6 M KOH (aq.) |
| ECC/$MnO_x$-h[12] | 23.5 | 0.8 | 14.6 | 5 mV $s^{-1}$ | 5 M LiCl (aq.) |
| AC-TCNF@SWCNT-C (6 layers)[29] | 134 | 4.5 | 15.1 | 0.2 A $g^{-1}$ | 1 M $H_2SO_4$ (aq.) |
| 3D G/$ZnV_2O_6$@$Co_3V_2O_8$ (8 layers)[28] | 65.2 | 2 | 16.1 | 0.5 A $g^{-1}$ | 1 M KOH (aq.) |
| 3D NiCoP/Mxene (6 layers)[27] | 46.3 | 1.5 | 19.0 | 10 mA $cm^{-2}$ | 2 M KOH (aq.) |
| G/$MnO_2$[26] | 9.8 | 0.2 | 20.1 | 2 mV $s^{-1}$ | 0.5 M $Na_2SO_4$ (aq.) |
| Cu/Co-THQ@CNTs@rGO (12 layers)[25] | 19.9 | 3 | 21.6 | 0.05 A $g^{-1}$ | 1 M LiPF6 in EC/DEC (*v* 1:1) |
| Cu/Co-THQ@CNTs@rGO (4 layers)[25] | 6.6 | 1 | 22.4 | 0.05 A $g^{-1}$ | 1 M LiPF6 in EC/DEC (*v* 1:1) |
| 3D G/$MnO_2$ (4mm)[10] | 182.2 | 4 | 24.5 | 0.5 mA $cm^{-2}$ | 3 M LiCl (aq.) |
| 3D G/$MnO_2$ (1mm)[10] | 45.2 | 1 | 25.7 | 0.5 mA $cm^{-2}$ | 3 M LiCl (aq.) |
| Non-Graded 3D GA/$MnO_2$-180 | 68.7 | 1.80 | 28.8 | 20 mA $cm^{-2}$ (≈0.3 A $g^{-1}$) | 1 M $LiClO_4$ in AN |

| Electrode | Mass Loading / mg $cm^{-2}$ | Thickness / mm | $Q_v$ / mA h $cm^{-3}$ | *j* or *v* | Electrolyte |
|---|---|---|---|---|---|
| Graded 3D GA/$MnO_2$-180 | 67.7 | 1.80 | 29.1 | 20 mA $cm^{-2}$ (≈0.3 A $g^{-1}$) | 1 M $LiClO_4$ in AN |

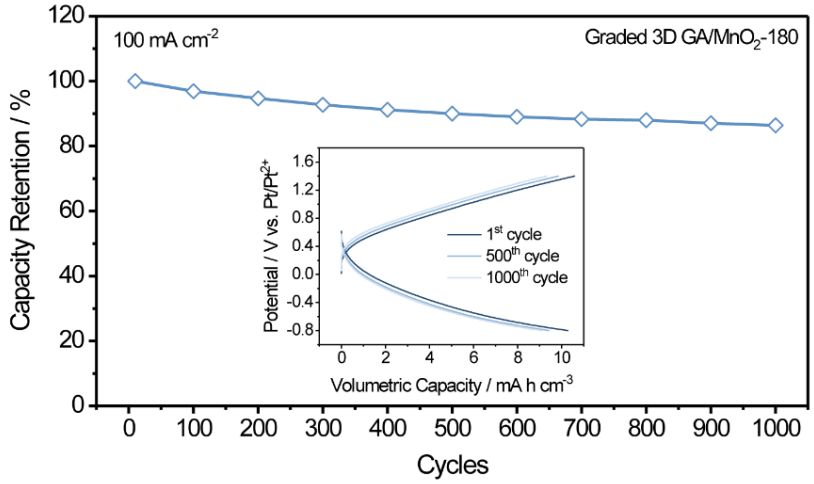


**Figure 3.14** Long-term cyclic stability of graded 3D GA/$MnO_2$-180 (67.7 mg $cm^{-2}$). Inset compares the GCD voltage profiles at different cycles.

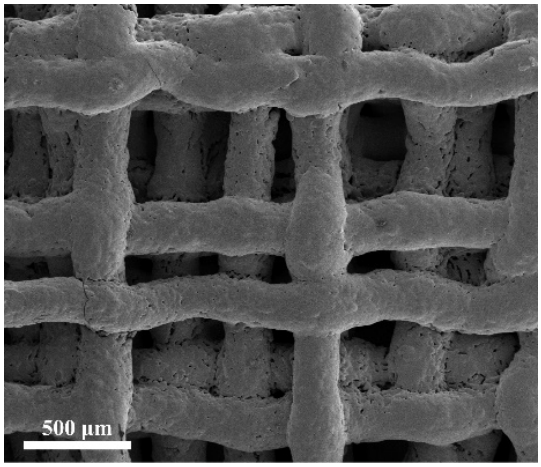

**Figure 3.15** SEM image of graded 3D GA/$MnO_2$-180 (67.7 mg $cm^{-2}$) after the cyclic stability test.

Despite the graded and non-graded electrodes having similar volumetric capacitance at 20 mA $cm^{-2}$, the graded electrode shows considerably better capacity retention. As shown in Figure 3.16, compared to the non-graded electrode, the graded 3D GA/$MnO_2$-180 exhibits not only higher volumetric capacities but also better capacity retentions at measured current densities (39.5% vs 29.0%) and improved capacity retention implies faster kinetics exhibited by the system. We also performed electrochemical impedance spectroscopy and fitted the data with proper equivalent circuits to deconvolute resistances of different electrochemical processes, including series resistance ($R_s$), charge transfer resistance ($R_{ct}$), diffusion resistance ($R_d$), and diffusion time constant ($\tau_d$) (Figure 3.17). Noted that $R_d$ and $\tau_d$ were obtained from the restricted diffusion element *M*, which is used for diffusions involving $Li^+$ ion insertion/desertion. Both graded and non-graded 3D GA/$MnO_2$-180 have comparable series resistance and charge transfer resistance. The greatest difference observed between them is in diffusion resistance. The graded electrode has a diffusion resistance of 11.19 Ω and a diffusion time constant of 4.946 s, which are substantially smaller than that of the non-graded electrode (38.25 Ω and 11.12 s, respectively), representing a less impeded and more efficient ion diffusion process in the graded structure. Smaller diffusion resistance is critical for sufficient ion supply and thus preserving a high degree of active material utilization during fast charge/discharge.

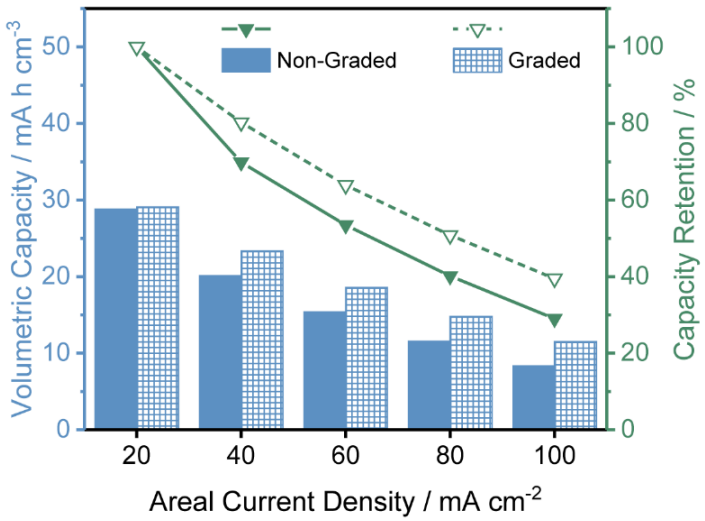


**Figure 3.16** Comparisons of volumetric capacities and capacity retentions at different areal current densities between non-graded 3D GA/$MnO_2$-180 (68.7 mg $cm^{-2}$) and graded 3D GA/$MnO_2$-180 (67.7 mg $cm^{-2}$).

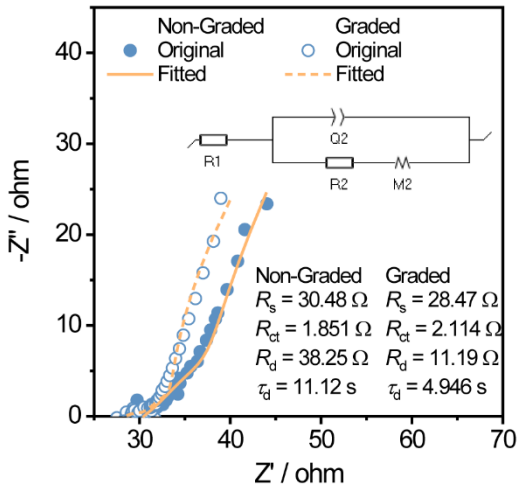

**Figure 3.17** Nyquist plots and the fitted results of non-graded and graded 3D GA/$MnO_2$-180.

To quantitatively unveil the portions of capacity originating from fast reversible surface electrochemical reactions, Trasatti capacity contribution analysis was performed.[12,35,36] The gravimetric capacities based on $MnO_2$ mass loadings are calculated from cyclic voltammetry curves (Figure 3.18) and plotted against $v^{-1/2}$ ($v$ is scan rate), as shown in Figure 3.19. By assuming semi-infinite ion diffusion, a linear fitting line at low scan rates can be extrapolated to determine the y-intercept ($v \rightarrow +\infty$) that represents the gravimetric capacity contributed by the surface ($Q_{surface}$). Compared to a non-graded electrode, the graded 3D GA/$MnO_2$-180 prevailed not only in the total gravimetric capacity at all scan rates but also in $Q_{surface}$ with a nearly onefold increase from 22.7 to 46.9 mA h $g^{-1}$. At a low scan rate of 1 mV $s^{-1}$, the $Q_{surface}$ of graded 3D GA/$MnO_2$-180 contributed 62.0% of the total capacity, while the non-graded counterpart is only 32.4% (Figure 3.20a). When the scan rate increased to 5 mV $s^{-1}$, the contribution from $Q_{surface}$ was further increased to 78.7% for graded 3D GA/$MnO_2$-180, while merely 53.0% for non-graded 3D GA/$MnO_2$-180 (Figure 3.20b). These results again support better accessibility and utilization of $MnO_2$ benefited by the graded structure, as the enlarged exterior pores guaranteed higher $Li^+$ ion flux to reach the interior domains (Figure 3.21).

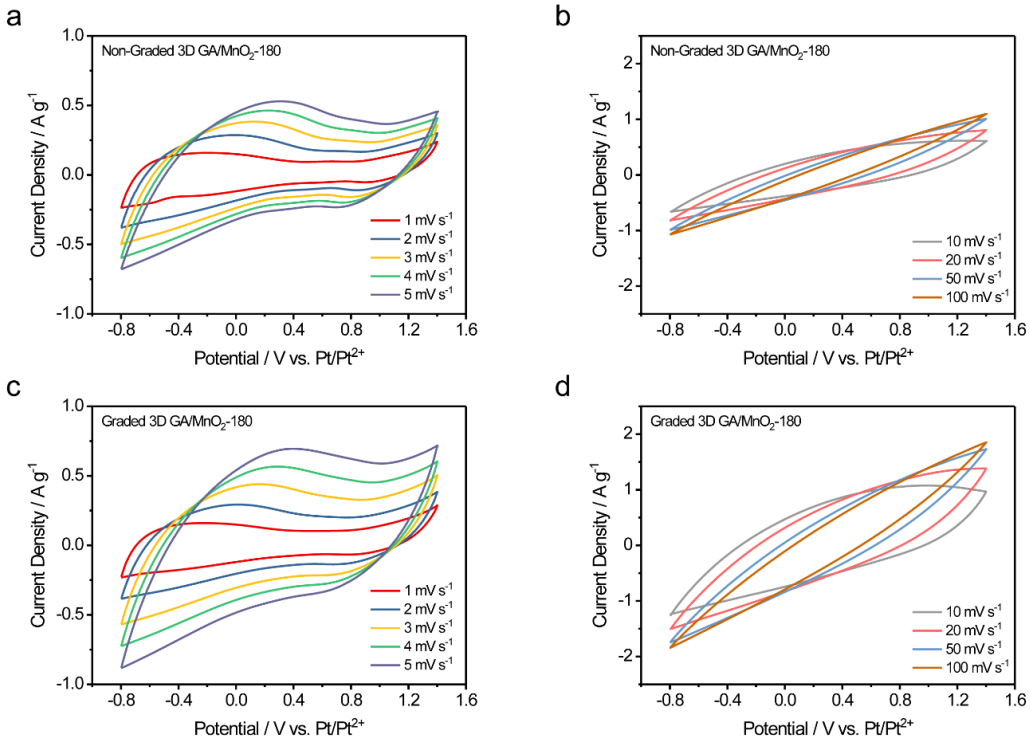


**Figure 3.18** CV curves of non-graded 3D GA/$MnO_2$-180 (68.7 mg $cm^{-2}$) at (a) low scan rates and (b) high scan rates. CV curves of graded 3D GA/$MnO_2$-180 (67.7 mg $cm^{-2}$) at (c) low scan rates and (d) high scan rates.

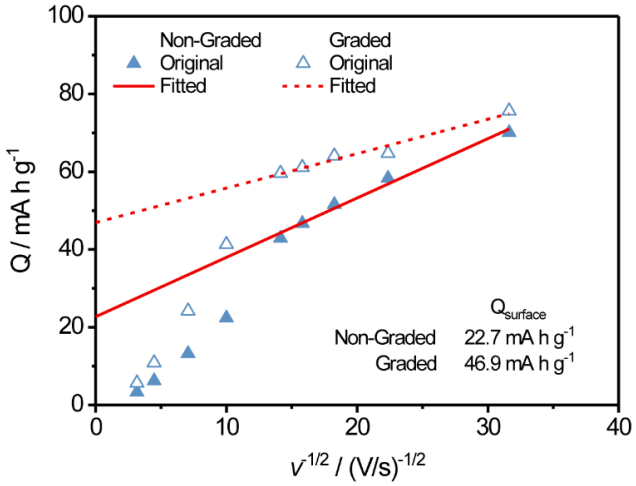


**Figure 3.19** Plot of gravimetric capacity ($Q$) vs. $v^{-1/2}$ for non-graded and graded 3D GA/$MnO_2$-180.

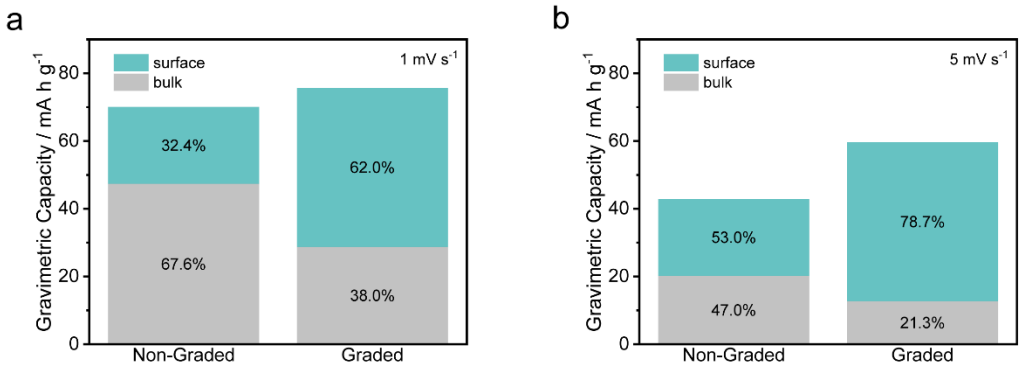


**Figure 3.20** Histogram illustrations of surface capacity contributions in non-graded and graded 3D GA/$MnO_2$-180 at a scan rate of (a) 1 mV $s^{-1}$ and (b) 5 mV $s^{-1}$.

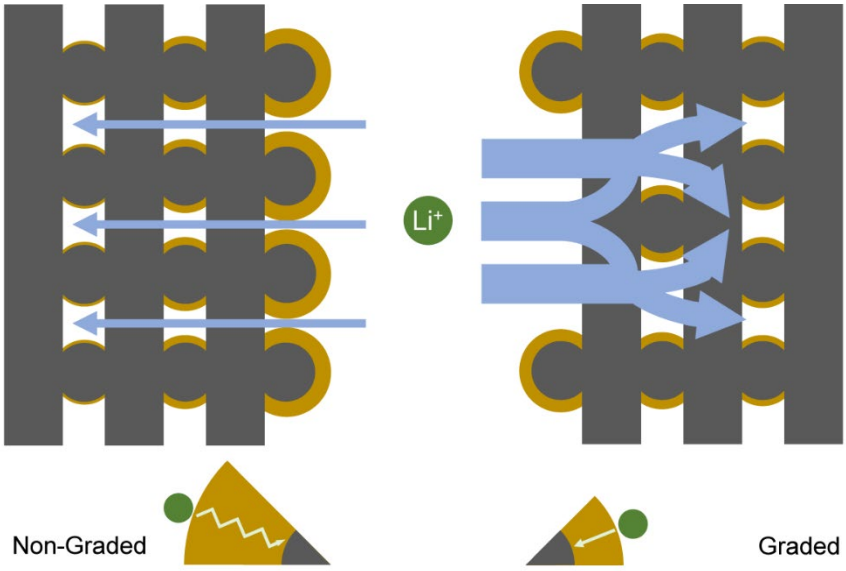


**Figure 3.21** Schematic illustration of the $Li^+$ ion flux in graded *vs.* non-graded structure.

**Electrochemical Performances of Lithium-Ion Hybrid Capacitor Devices**

The graded 3D GA/$MnO_2$-180 (68.2 mg $cm^{-2}$) electrode was paired with a graded 3D GA anode electrodeposited with $VO_x$ (3D GA/$VO_x$, 33.3 mg $cm^{-2}$) to assemble a non-aqueous Li-ion hybrid capacitor device (Figure 3.22). A high output voltage of 4 V was achieved (Figure 3.23a), accompanied by a typical capacitor-battery hybrid behavior within this wide voltage window (Figure 3.23b). The impressive maximum volumetric capacity of 11.6 mA h $cm^{-3}$ (Figure 3.23c) and maximum volumetric capacitance of 11.9 F $cm^{-3}$ (Figure 3.24) were achieved, ultimately leading to a large volumetric energy density of 20.2 W h $L^{-1}$ compared against other reported 3D-structured supercapacitors and Li-ion hybrid capacitors (Figure 3.23d), such as G/$ZnV_2O_6$@$Co_3V_2O_8$//G/VN,[28] $MnO_2$@WC//AWC,[31] AC-TCNF@SWCNT-C

symmetric supercapacitor (SSC),[29] 3D G/$MnO_2$ SSC,[10] 3D GA/$MnO_2$//SF-3D GA,[11] 3D-GCA SSC,[37] etc.

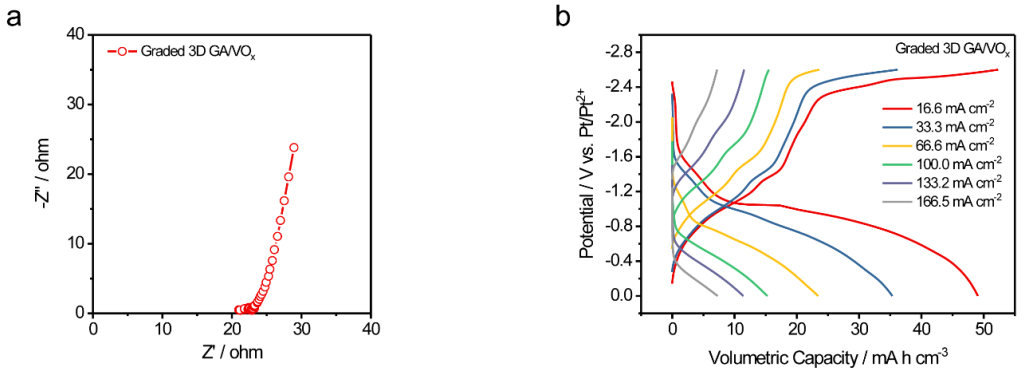


**Figure 3.22** (a) EIS spectra and (b) GCD voltage profiles of graded 3D GA/$VO_x$ (36.0 mg $cm^{-2}$).

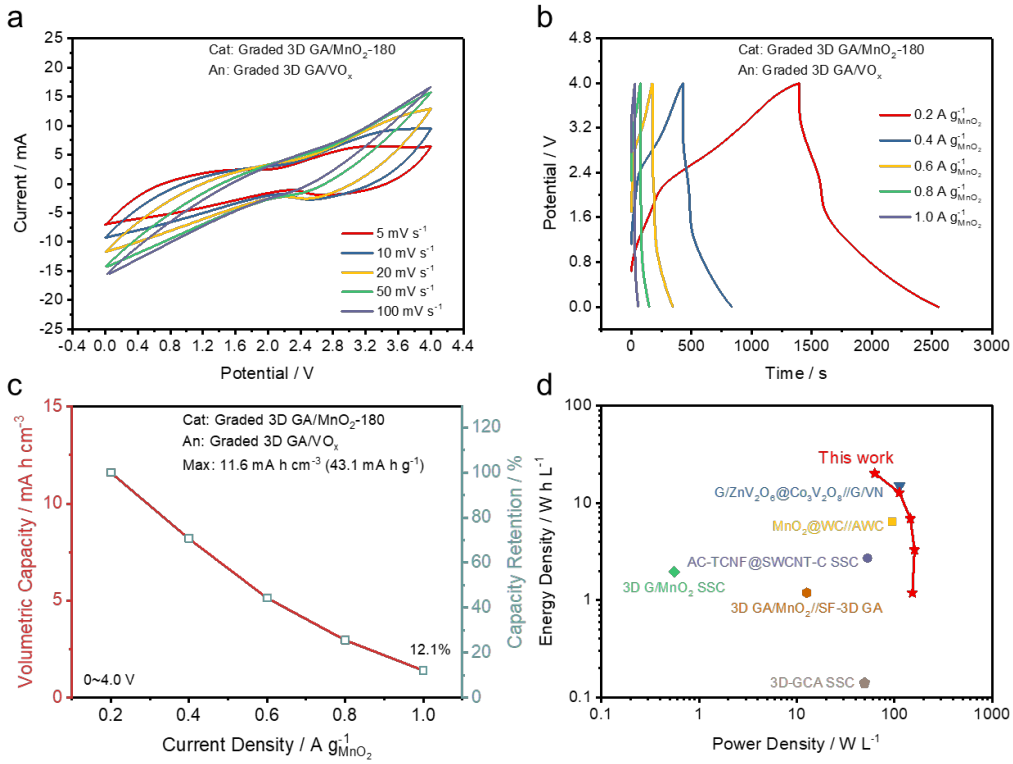

**Figure 3.23** (a) Cyclic voltammetry curves, (b) galvanostatic charge/discharge curves, and (c) volumetric capacity and capacity retention of the graded 3D/GA-$MnO_2$-180//3D GA/$VO_x$ Li-ion hybrid capacitor device. (d) Ragone plot of the graded 3D/GA-$MnO_2$-180//3D GA/$VO_x$ device. Values reported for other 3D-structured supercapacitors and Li-ion hybrid capacitors are added for comparison.[10,11,28,29,31,37]

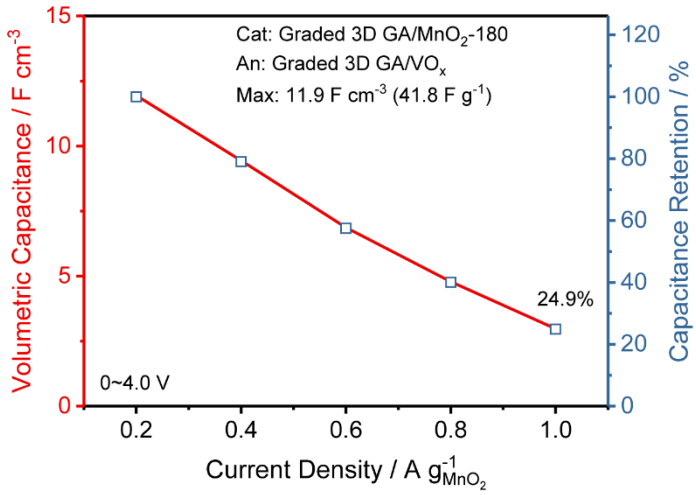


**Figure 3.24** Volumetric capacitance and capacitance retention of the graded 3D/GA-$MnO_2$-180//3D GA/$VO_x$ Li-ion hybrid capacitor device.

### 3.4 Conclusion

In conclusion, we have demonstrated a 3D printed graded structure that can better accommodate ultrahigh loading of $MnO_2$ than conventional lattice structure by homogenizing the $MnO_2$ film thickness and uniformity. The large exterior pores in the graded structure allow efficient ion diffusion during electrodeposition and

charge/discharge cycling, while the densely arranged interior ligaments provide a large ion-accessible active surface. The graded 3D GA/$MnO_2$-180 cathode achieves a record high maximum volumetric capacity of 29.1 mA h $cm^{-3}$ at a high current density of 20 mA $cm^{-2}$ with a wide voltage window of 2.2 V in the non-aqueous electrolyte, outperforming most reported 3D printed and/or high-$MnO_2$-loaded thick cathodes. Significantly, the electrodes show good capacity retention even at current densities as high as 100 mA $cm^{-2}$, which can be ascribed to the efficient ion transport into the interior domains of the electrode through the unimpeded open channels of the graded scaffold. The assembled Li-ion hybrid capacitor device with graded 3D GA/$MnO_2$-180 cathode and graded 3D GA/$VO_x$ anode exhibits a wide voltage window of 0-4 V and a superior volumetric energy density of 20.2 W h $L^{-1}$. These findings can inspire the future development of thick and porous substrates for the electrodeposition of high-loading materials and improve capacitance retention and volumetric energy density.

## References


1. X. Yang, C. Cheng, Y. Wang, L. Qiu, D. Li. *Science* **2013**, *341*, 534-537.

2. D. Yu, K. Goh, H. Wang, L. Wei, W. Jiang, Q. Zhang, L. Dai, Y. Chen. *Nat. Nanotechnol.* **2014**, *9*, 555-562.

3. Y. Xu, Z. Lin, X. Zhong, X. Huang, N. O. Weiss, Y. Huang, X. Duan. *Nat. Commun.* **2014**, *5*, 4554.

4. G. Li, K. Mao, M. Liu, M. Yan, J. Zhao, Y. Zeng, L. Yang, Q. Wu, X. Wang, Z. Hu. *Adv. Mater.* **2020**, *32*, 2004632.

5. J. Yan, Q. Wang, T. Wei, L. Jiang, M. Zhang, X. Jing, Z. Fan. *ACS Nano* **2014**, *8*, 4720-4729.

6. J. B. Goodenough, A. Manthiram. *MRS Commun.* **2014**, *4*, 135-142.

7. Y. Tao, X. Xie, W. Lv, D.-M. Tang, D. Kong, Z. Huang, H. Nishihara, T. Ishii, B. Li, D. Golberg, F. Kang, T. Kyotani, Q.-H. Yang. *Sci. Rep.* **2013**, *3*, 2975.

8. A. Noori, M. F. El-Kady, M. S. Rahmanifar, R. B. Kaner, M. F. Mousavi. *Chem. Soc. Rev.* **2019**, *48*, 1272-1341.

9. M. Yu, Y. Lu, H. Zheng, X. Lu. *Chem. Eur. J.* **2018**, *24*, 3639-3649.

10. B. Yao, S. Chandrasekaran, J. Zhang, W. Xiao, F. Qian, C. Zhu, E. B. Duoss, C. M. Spadaccini, M. A. Worsley, Y. Li. *Joule* **2019**, *3*, 459-470.

11. B. Yao, S. Chandrasekaran, H. Zhang, A. Ma, J. Kang, L. Zhang, X. Lu, F. Qian, C. Zhu, E. B. Duoss, C. M. Spadaccini, M. A. Worsley, Y. Li. *Adv. Mater.* **2020**, *32*, 1906652.

12. Y. Song, T. Liu, B. Yao, M. Li, T. Kou, Z.-H. Huang, D.-Y. Feng, F. Wang, Y. Tong, X.-X. Liu, Y. Li. *ACS Energy Lett.* **2017**, *2*, 1752-1759.

13. A. Huang, J. Chen, W. Zhou, A. Wang, M. Chen, Q. Tian, J. Xu. *J. Electroanal. Chem.* **2020**, *873*, 114392.

14. W. Sun, F. Wang, S. Hou, C. Yang, X. Fan, Z. Ma, T. Gao, F. Han, R. Hu, M. Zhu, C. Wang. *J. Am. Chem. Soc.* **2017**, *139*, 9775-9778.

15. C. Pan, R. Zhang, R. G. Nuzzo, A. A. Gewirth. *Adv. Energy Mater.* **2018**, *8*, 1800589.

16. Y. Wang, Z. Hong, M. Wei, Y. Xia. *Adv. Funct. Mater.* **2012**, *22*, 5185-5193.

17. D. Kundu, S. Hosseini Vajargah, L. Wan, B. Adams, D. Prendergast, L. F. Nazar. *Energy Environ. Sci.* **2018**, *11*, 881-892.

18. G. Lee, D. Kim, D. Kim, S. Oh, J. Yun, J. Kim, S.-S. Lee, J. S. Ha. *Energy Environ. Sci.* **2015**, *8*, 1764-1774.

19. H.-Q. Wang, Z.-S. Li, Y.-G. Huang, Q.-Y. Li, X.-Y. Wang. *J. Mater. Chem.* **2010**, *20*, 3883-3889.

20. K.-W. Nam, C.-W. Lee, X.-Q. Yang, B. W. Cho, W.-S. Yoon, K.-B. Kim. *J. Power Sources* **2009**, *188*, 323-331.

21. L. Y. Chen, J. L. Kang, Y. Hou, P. Liu, T. Fujita, A. Hirata, M. W. Chen. *J. Mater. Chem. A* **2013**, *1*, 9202-9207.

22. J. Duay, S. A. Sherrill, Z. Gui, E. Gillette, S. B. Lee. *ACS Nano* **2013**, *7*, 1200-1214.

23. K. M. Champley, T. M. Willey, H. Kim, K. Bond, S. M. Glenn, J. A. Smith, J. S. Kallman, W. D. Brown, I. M. Seetho, L. Keene, S. G. Azevedo, L. D. McMichael, G. Overturf, H. E. Martz. *NDT & E Int.* **2022**, *126*, 102595.

24. J. Schindelin, I. Arganda-Carreras, E. Frise, V. Kaynig, M. Longair, T. Pietzsch, S. Preibisch, C. Rueden, S. Saalfeld, B. Schmid, J.-Y. Tinevez, D. J. White, V. Hartenstein, K. Eliceiri, P. Tomancak, A. Cardona. *Nat. Methods* **2012**, *9*, 676-682.

25. J. Zhao, Y. Zhang, H. Lu, Y. Wang, X. D. Liu, H. Maleki Kheimeh Sari, J. Peng, S. Chen, X. Li, Y. Zhang, X. Sun, B. Xu. *Nano Lett.* **2022**, *22*, 1198-1206.

26. Y. He, W. Chen, X. Li, Z. Zhang, J. Fu, C. Zhao, E. Xie. *ACS Nano* **2013**, *7*, 174-182.

27. L. Yu, W. Li, C. Wei, Q. Yang, Y. Shao, J. Sun. *Nano Micro Lett.* **2020**, *12*, 143.

28. J. Zhao, Y. Zhang, X. Zhao, R. Wang, J. Xie, C. Yang, J. Wang, Q. Zhang, L. Li, C. Lu, Y. Yao. *Adv. Funct. Mater.* **2019**, *29*, 1900809.

29. W. Kang, L. Zeng, S. Ling, C. Lv, J. Liu, R. Yuan, C. Zhang. *Adv. Funct. Mater.* **2021**, *31*, 2102184.

30. T. Gao, Z. Zhou, J. Yu, J. Zhao, G. Wang, D. Cao, B. Ding, Y. Li. *Adv. Energy Mater.* **2019**, *9*, 1802578.

31. C. Chen, Y. Zhang, Y. Li, J. Dai, J. Song, Y. Yao, Y. Gong, I. Kierzewski, J. Xie, L. Hu. *Energy Environ. Sci.* **2017**, *10*, 538-545.

32. J. Yang, L. Lian, H. Ruan, F. Xie, M. Wei. *Electrochim. Acta* **2014**, *136*, 189-194.

33. T. Zhai, F. Wang, M. Yu, S. Xie, C. Liang, C. Li, F. Xiao, R. Tang, Q. Wu, X. Lu, Y. Tong. *Nanoscale* **2013**, *5*, 6790-6796.

34. P. Chang, H. Mei, Y. Tan, Y. Zhao, W. Huang, L. Cheng. *J. Mater. Chem. A* **2020**, *8*, 13646-13658.

35. S. Ardizzone, G. Fregonara, S. Trasatti. *Electrochim. Acta* **1990**, *35*, 263-267.

36. D. Baronetto, N. Krstajić, S. Trasatti. *Electrochim. Acta* **1994**, *39*, 2359-2362.

37. C. Zhu, T. Liu, F. Qian, T. Y.-J. Han, E. B. Duoss, J. D. Kuntz, C. M. Spadaccini, M. A. Worsley, Y. Li. *Nano Lett.* **2016**, *16*, 3448-3456.

# Chapter 4 - Prototypical Study of Double-Layered Cathodes for Aqueous Rechargeable Static Zn-$I_2$ Batteries


## Abstract

Aqueous rechargeable zinc-iodine batteries (ZIBs) are promising candidates for grid energy storage because they are safe and low-cost and have high energy density. However, the shuttling of highly soluble triiodide ions severely limits the device's Coulombic efficiency. Herein, we demonstrate for the first time a double-layered cathode configuration with a conductive layer (CL) coupled with an adsorptive layer (AL) for ZIBs. This unique cathode structure enables the formation and reduction of adsorbed $I_3^-$ ions at the CL/AL interface, successfully suppressing triiodide ion shuttling. A prototypical ZIB using a carbon cloth as the CL and a polypyrrole layer as the AL simultaneously achieves outstanding Coulombic efficiency (up to 95.6%) and voltage efficiency (up to 91.3%) in the aqueous $ZnI_2$ electrolyte even at high-rate intermittent charging/discharging, without the need of ion selective membranes. These findings provide new insights to the design and fabrication of ZIBs and other batteries based on conversion reactions.

## 4.1 Introduction

Aqueous rechargeable zinc-based batteries, including Zn-ion batteries, alkaline Zn-based batteries, and Zn-based redox flow batteries, are promising candidates for next-generation grid storage and battery-buffered charging stations due to the high level of safety, low cost, and high power density.[1-5] Among them, the zinc-iodine ($Zn\text{-}I_2$) redox flow battery using an aqueous $ZnI_2$ electrolyte has attracted a lot of attention. It offers impressive theoretical capacity (211 mAh $g_{iodine}^{-1}$, 820 mAh $g_{zinc}^{-1}$) and energy density (322 Wh $L^{-1}$) owing to the high solubility of $ZnI_2$ (up to 7 M) and multielectron conversion reactions.[6-13] During charging, metallic zinc is electrodeposited on the anode ($Zn^{2+} + 2e^- \rightarrow Zn$), while the slightly soluble iodine is generated on the cathode and spontaneously transformed into highly soluble triiodide ($I_3^-$) ions with the presence of iodide ($I^-$) ions ($2I^- \rightarrow I_2 + 2e^-$; $I_2 + I^- \rightarrow I_3^-$).[11] Reverse reactions occur during discharging.

Static $Zn\text{-}I_2$ batteries (ZIBs) have recently been developed to overcome critical drawbacks of flow batteries, such as bulky, complex cell configuration and low overall energy density due to the need of supporting equipment. However, a major challenge for both static and flow ZIBs is the self-discharge caused by the shuttling of $I_3^-$ ions to the zinc anode, which causes low Coulombic efficiency (CE).[9,11] A common solution is physically blocking the $I_3^-$ shuttling using an ion selective membrane (ISM) separator. Nevertheless, adding ISMs substantially increases the device cost and inner resistance.[8,11,13-16] An alternative option is to encapsulate $I_2$ in a microporous carbon electrode and use a non-$ZnI_2$ solution (e.g., $ZnSO_4$) as the electrolyte. In this case, the

$I_2/I^-$ conversion reactions are confined inside micropores, while the generation and shuttling of $I_3^-$ are also eliminated in the absence of $I^-$ in the aqueous electrolyte.[6,9,12] Yet, as a trade-off for high CE, the device's total capacity and energy density are limited by the $I_2$ loading in a microporous carbon. A water-in-salt electrolyte has also been used to achieve surface heterogeneous ($I_2/I^-$) conversion reactions without the need of ISMs.[7] Despite the enhanced CE, the electrolyte with high viscosity and low conductivity limited the highest charge/discharge rate, which is unfavorable for high-power applications.

An outstanding challenge for the static ZIB is how to retain a high CE in an aqueous $ZnI_2$ electrolyte without the need of ISMs. To tackle this challenge, here we design a new ZIB system (Figure 4.1) with a double-layered cathode configuration containing a conductive layer (CL, as a cathodic current collector) and an inexpensive adsorptive layer (AL, a cathode extension). During charging, the $I^-$ ions in the electrolyte transfer electrons to the CL and spontaneously form adsorbed $I_3^-$ ions (denoted as A-$I_3^-$) at the CL/AL interface. These A-$I_3^-$ ions subsequently diffuse into the bulk AL under a concentration gradient and re-expose the interfacial adsorption sites for the newly formed $I_3^-$ ions. During discharging, the dominant A-$I_3^-$ ions are reduced at the CL/AL interface to regenerate $I^-$ ions.

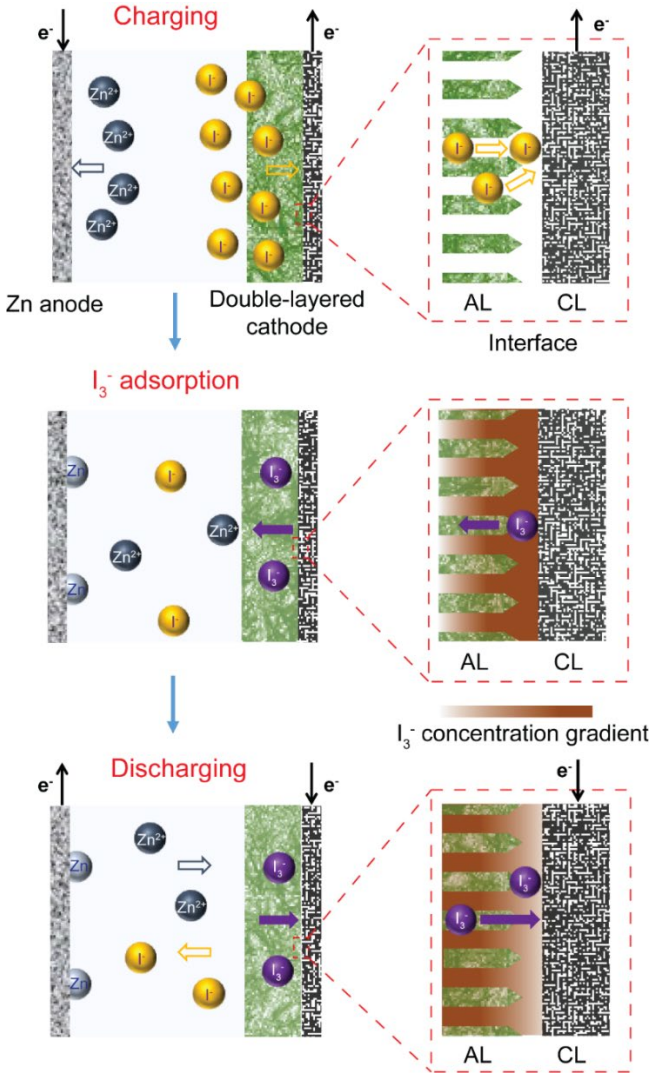


**Figure 4.1** Schematic illustrations of the operation mechanisms of a ZIB with a double-layered cathode (AL in green and CL in black). Dashed boxes highlight the reactions that take place at the CL/AL interface. Empty arrows represent electromigration. Solid arrows represent diffusion.

The CL requires good conductivity, while the AL needs a good $I_3^-$ adsorption capability. We believe that conducting polymers such as polypyrrole (PPy), polyaniline,

and poly(3,4-ethylenedioxythiophene) are promising candidates for AL because they allow both physical and chemical interaction with $I_3^-$ ions. $I_3^-$ ions tend to chemically interact with many polymers by bonding with cations,[17,18] doping positive-charged polymers,[19] or assembling into clathrates through secondary interactions.[20] As a proof of concept, we used carbon cloth (CC) as the CL and CC electrodeposited with a PPy film (CC-PPy) as the AL. The static ZIBs equipped with the double-layered cathode were tested in a $ZnI_2$ aqueous electrolyte. They showed a significantly improved CE (up to 95.6%) at different charging/discharging rates, confirming the self-discharge caused by $I_3^-$ shuttling was mostly suppressed.

## 4.2 Experimental Methods

### Synthesis of Carbon Cloth-Polypyrrole Composite Adsorptive Layers

All chemicals are of analytical grade and directly used without further purification. Polypyrrole (PPy) film was electro-polymerized on carbon cloth (CC) substrate using a three-electrode system in a solution of 0.1 M pyrrole and 0.05 M sulfuric acid. Graphite rod and saturated calomel electrode were used as the counter and the reference electrodes, respectively. Before electro-polymerization, the CC was immersed in the solution (effective area: 1.0 × 1.0 $cm^2$) and degassed in vacuum at room temperature until no air bubble was released. The electro-polymerization was conducted using a pulse current method. In one deposition cycle, the current density was kept at 2 mA $cm^{-2}$ for 1 min and then open circuit for 10 s to allow uniform redistribution of pyrrole. This deposition step was repeated to increase the mass loading

of PPy. The composite ALs are denoted as CC-PPy-x, where x represents the number of cycles for electro-polymerization. The obtained samples were washed with deionized water and ethanol, and then vacuum dried overnight at room temperature. The average mass loadings of PPy are 1.48 mg $cm^{-2}$ (CC-PPy-30), 2.88 mg $cm^{-2}$ (CC-PPy-60), 5.23 mg $cm^{-2}$ (CC-PPy-120), and 9.56 mg $cm^{-2}$ (CC-PPy-240). For batteries with CC-PPy-120 adsorptive layers, the mass of PPy is only ~2.38% of the total mass of the battery (Zn anode + double-layered cathode + separator + electrolyte). If the mass of current collectors and outer packages are included, the difference of energy density will be even smaller. Therefore, the additional mass of PPy has a negligible effect on the overall energy density of the cell.

**Material Characterization**

The microstructures and compositions of the electrode materials were analyzed using a field emission scanning electron microscope (SEM, FEI Quanta 3D FEG dual beam). Elemental analysis was conducted using a Genesis energy-dispersive X-ray spectrometer installed in a FEI Quanta 200 environmental scanning electron microscope (ESEM). The CC-PPy-120 ALs for elemental analysis were re-charged to 1.15 V after galvanostatic charge/discharge cycles to ensure PPy at the same fully charged (doped) state as the as-prepared counterparts. 1.15 V is the open circuit potential of the as-assembled ZIBs with the as-prepared CC-PPy-120 ALs, and the oxidation of $I^-$ to $I_3^-$ does not take place at this voltage. The atomic content of sulfur and iodine were normalized to the atomic content of nitrogen, because the nitrogen content is directly correlated to the mass loading of PPy.

**Fabrication of the Aqueous Zn-$I_2$ Battery with Swagelok Cell**

A Swagelok cell consists of a Teflon case and two stainless-steel rods as current collectors. To prevent corrosion during charging/discharging in mild acidic electrolyte, the end of each stainless-steel rod was protected with a titanium cap. Inside the Swagelok cell case, the aqueous Zn-$I_2$ battery was assembled with a zinc foil anode, an anode-side separator (to prevent zinc dendrite penetration), a cathode-side separator (to reserve enough electrolyte), an AL, a CC CL, and 60 μL $ZnI_2$ electrolyte. The CC CLs and the zinc anodes were hollow punched with a diameter of 9/32 inches (40 $mm^2$) from a CC sheet and a zinc foil (0.8 mm thick), respectively. The anode-side separator and the cathode-side separator were hollow punched with a diameter of 3/8 inches (71 $mm^2$) from a Whatman glass microfiber filter and a Whatman filter paper, respectively. The AL was hollow punched with a diameter of 5/16 inches (49.7 $mm^2$) from a CC-PPy-x sample or a CC (as control sample). The electrolyte was prepared by dissolving 0.5 M $ZnI_2$ powders into 0.1 M HAc/NaAc buffer solution. All battery devices have the same electrolyte usage and comparable interfacial resistance.

**Electrochemical Measurements**

All electrochemical tests were conducted on an electrochemical workstation (BioLogic) using Swagelok cells. Data were collected after a 2-cycle cyclic voltammetry test at 10 mV $s^{-1}$ (0.8 ~ 1.6 V) to allow complete permeation of electrolyte. All current rates are determined by the capacity of the $ZnI_2$ in the electrolyte. For a typical electrolyte volume of 60 μL, the charges required to fully reduce $Zn^{2+}$ to $Zn^0$ (or fully oxidize $I^-$ to $I_2$) is 1.6 mA h, and therefore 1 C = 1.6 mA. 10% depth of charge

corresponds to a charging capacity of 0.16 mA h and 20% depth of charge corresponds to 0.32 mA h. The frequency range of electrochemical impedance spectroscopy is $10^{-2}$ ~ $10^{6}$ Hz.

For intermittent GCD tests, CC+CC-PPy-120 was first activated by running ten consecutive GCD cycles at 0.5 C and 10% depth of charge. Different standby times (0, 15, 30, 60, 120 mins) were applied between charge and discharge processes to allow diffusion/adsorption/shuttle of $I_3^-$ after charging, which can rule out the false high CE due to the incomplete shuttling of F-$I_3^-$ before discharging, especially in high-rate consecutive charge/discharge processes. Since the voltages of CC+CC discharging after standby process are indistinguishable (mainly from capacitance of CC), charging/discharging voltages from consecutive GCD tests of CC+CC are used as comparison to show distinguishable F-$I_3^-$ discharging voltages at different rates.

**Density Functional Theory (DFT) Calculations**

Vienna *ab initio* simulation package (VASP)[21] was employed to perform all DFT calculations, including geometric structures optimization and adsorption energy. For each calculation, projected augmented wave (PAW) method combined with exchange-correlation functional of Perdew-Burke-Ernzerhof (PBE) in the generalized gradient approximation (GGA)[22,23] were used to describe ion-electron interactions, using the parameters of $10^{-5}$ eV in energy, $10^{-2}$ eV/Å in force and 500 eV in cut-off energy. In order to accurately describe the weak interactions, the Grimme DFT-D3 dispersion correction method was employed for all calculations.[24]

## 4.3 Results and Discussions

### Mechanism Studies of the Double-Layered Cathode

CC-PPy-*x* ALs with different PPy loadings were prepared by galvanostatic electropolymerization of pyrrole on CC in an aqueous sulfuric acid electrolyte, where *x* represents the number of electro-polymerization cycles. AL samples have uniform and compact PPy films wrapping on carbon fibers (Figure 4.2). Galvanostatic charge/discharge (GCD) tests with a fixed depth of charge (10%, 0.16 mA h) were conducted at 0.5 C to investigate the influence of ALs on the ZIB's performance. The enhancement of CE is directly correlated to the loading of PPy (Figure 4.3). However, the device's inner resistance also increases with the PPy loading. Among the samples we studied, CC-PPy-120 AL has the optimal balance between the CE and the inner resistance. The ZIB that uses CC as the CL and CC-PPy-120 as the AL is denoted as CC+CC-PPy-120. We also prepared a control sample with bare CC as both the CL and the AL (denoted as CC+CC). Figure 4.4a shows the voltage profiles of the first 10 consecutive GCD cycles. The presence of the PPy-coated AL significantly enhanced the ZIB's CE from 36.2% (CC+CC) to 95.5% (CC+CC-PPy-120, the 10th cycle). This finding confirmed that the PPy coating can effectively trap and adsorb soluble $I_3^-$ ions generated during charging. In contrast, the bare CC has nearly no adsorption capability for the $I_3^-$ ions.

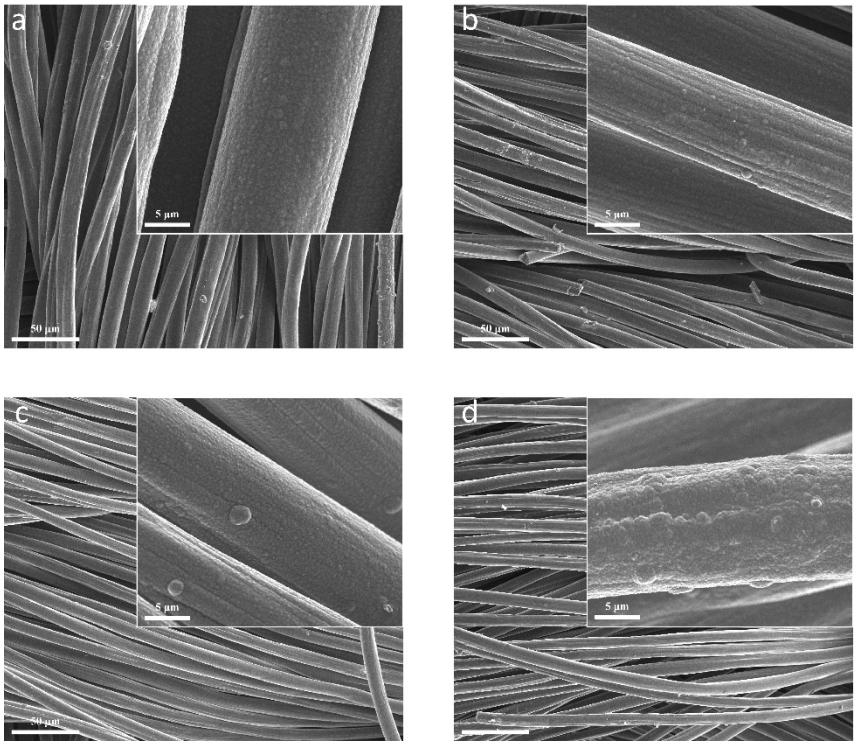


**Figure 4.2** SEM images of (a) CC-PPy-30, (b) CC-PPy-60, (c) CC-PPy-120, and (d) CC-PPy-240.

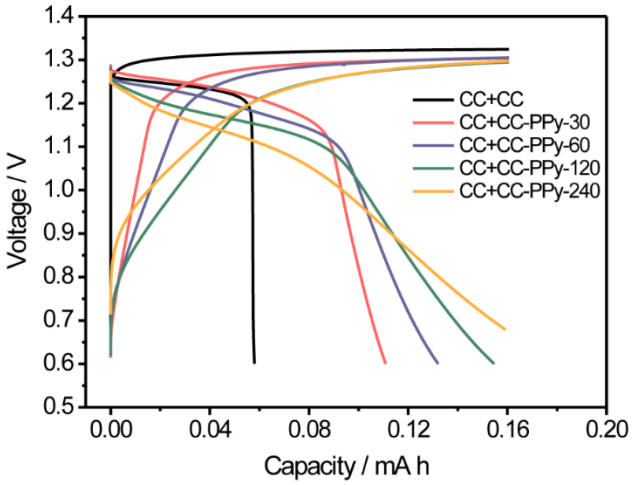

**Figure 4.3** Voltage profiles of CC+CC, CC+CC-PPy-30, CC+CC-PPy-60, CC+CC-PPy-120, and CC+CC-PPy-240 obtained at 0.5 C.

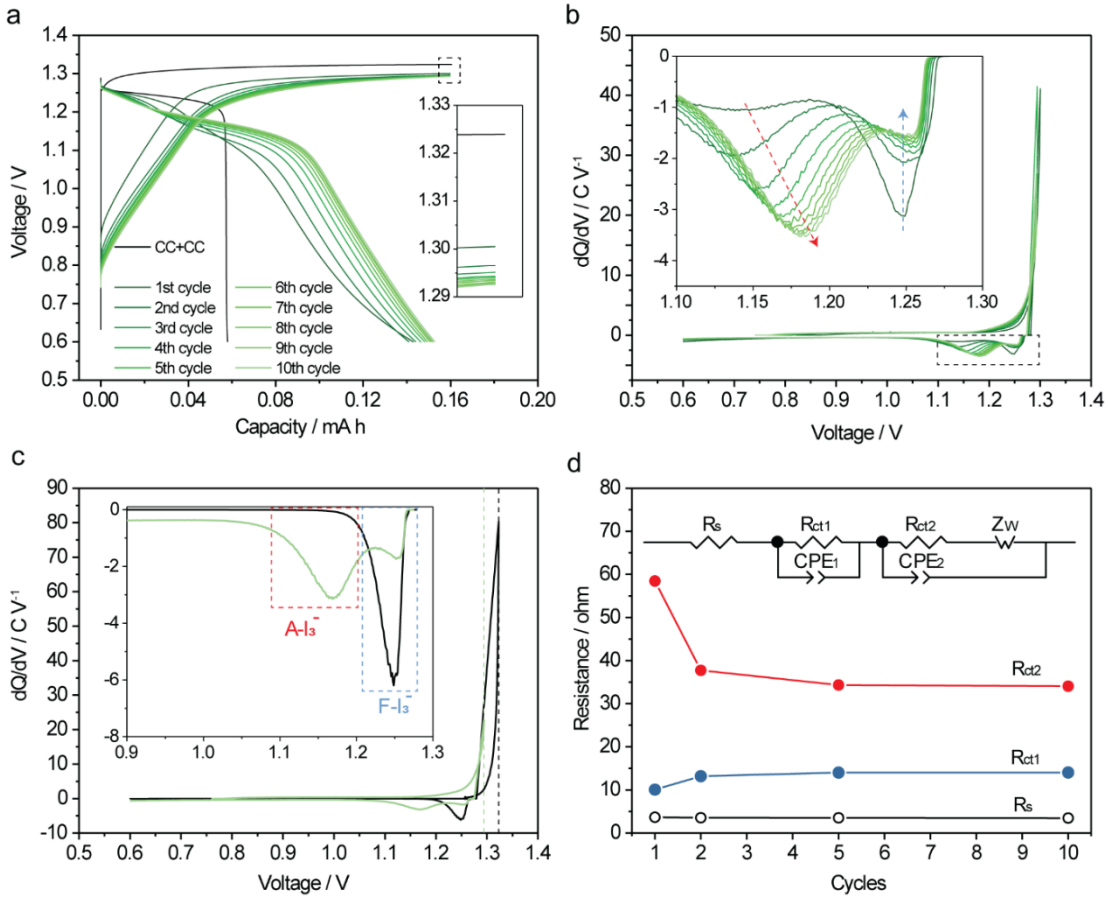


**Figure 4.4** (a) Voltage profiles of CC+CC (black curves) and CC+CC-PPy-120 (the first 10 charge/discharge cycles, green curves) obtained at 0.5 C. Inset shows the magnified view of the charging voltages highlighted in the dashed box. (b) Differential capacity plots of CC+CC-PPy-120 collected at 0.5 C for the first 10 charge/discharge cycles. Inset shows the magnified view of the discharging voltages highlighted in the dashed box. The higher the peak intensity, the flatter the voltage plateau, and therefore a higher concentration of the respective redox species. A larger area means a higher

number of charges. Arrows highlight the peak position and intensity changes over the cycles. (c) Differential capacity plots of CC+CC and CC+CC-PPy-120 (the 10th cycle) obtained at 0.5 C. Dashed lines highlight their charging voltages. Inset shows the magnified discharge peaks. (d) Values of the elements from the fitted EIS data collected at 1.17 V.

The GCD results also disclosed important mechanistic information for the CE enhancement and the role of PPy coating during charging/discharging. As shown in Figure 4.4a, the CE of CC+CC-PPy-120 increases over the first 10 cycles, indicating possible PPy transformations. Differential capacity plots (Figure 4.4b) derived from the voltage profiles (Figure 4.4a) can precisely identify the respective voltages of charge/discharge plateaus by transforming them into distinguishable peaks. CC+CC exhibits a charging plateau at 1.32 V (Figure 4.4a). CC+CC-PPy-120 has a slightly lower charging voltage at around 1.30 V in the first cycle, which gradually decreases and stabilizes over the cycles to 1.29 V. All devices with PPy ALs have a similar charging voltage at around 1.30 V (Figure 4.5). Differential capacity plots (Figures 4.4b and 4.4c) further show that CC+CC has a single discharging peak at 1.25 V, while CC+CC-PPy-120 have two discharging peaks. One of the two peaks locates at 1.25 V, and its peak position stays constant while the peak signal decreases over the cycles. The other discharge peak gradually increases from 1.13 to 1.18 V over cycles accompanied by the increase of the peak intensity. Based on the evolution of the CE and voltage, we deduced that the charge/discharge of CC+CC-PPy-120 involve free

solvated $I_3^-$ (denoted as F-$I_3^-$) and PPy-adsorbed $I_3^-$ (denoted as A-$I_3^-$). A-$I_3^-$ is expected to be more stable and, thus, has a lower Gibbs free energy of formation than that of F-$I_3^-$ (Figure 4.6). This model explains why CC+CC-PPy-120 has a lower charging voltage than CC+CC and exhibits an extra discharging peak at a lower voltage, because the generation of A-$I_3^-$ is thermodynamically favorable and its reduction is thermodynamically unfavorable compared to F-$I_3^-$. There is a negligible change of the F-$I_3^-$ discharging voltage of CC+CC-PPy-120 over the cycles because both the formation and the reduction of F-$I_3^-$ occur on the CC surface.

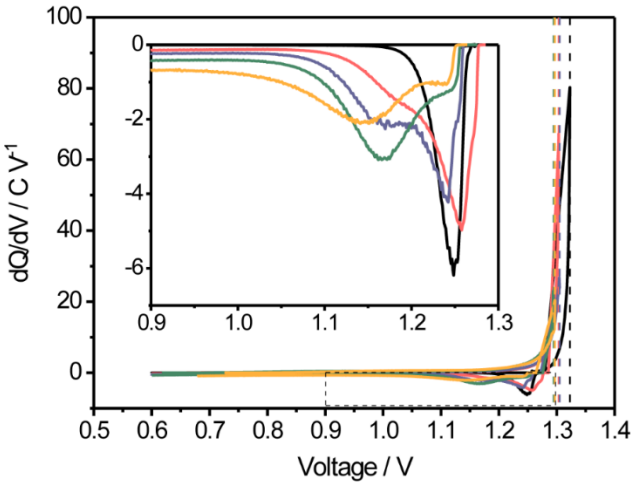


**Figure 4.5** Differential capacity plot of CC+CC, CC+CC-PPy-30, CC+CC-PPy-60, CC+CC-PPy-120, and CC+CC-PPy-240 obtained at 0.5 C. Dashed lines represent charging voltages. Inset figure is the magnification of discharging voltages highlighted in the dashed box.

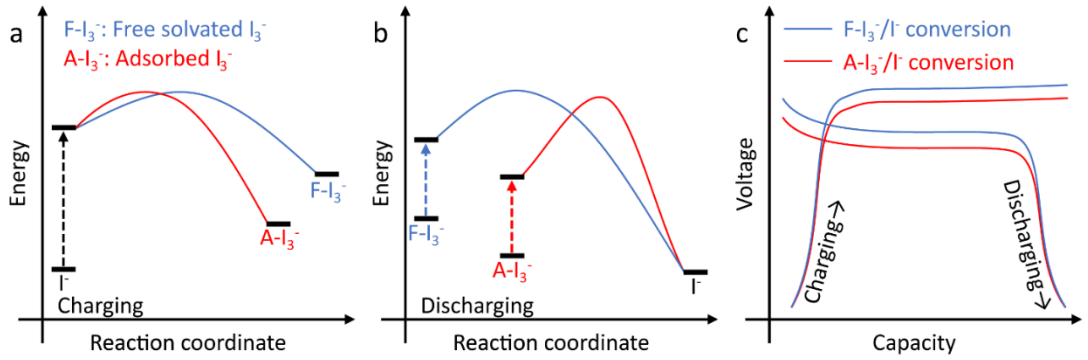


**Figure 4.6** Schematic illustration of the proposed energy profiles of $I_3^-/I^-$ conversions during (a) charging and (b) discharging, and proposed galvanostatic charge/discharge curves of (c) $F\text{-}I_3^-/I^-$ and $A\text{-}I_3^-/I^-$ conversions.

These results also offer important information on where the formation and reduction of $A\text{-}I_3^-$ take place. If $F\text{-}I_3^-$ generates on CC CL first and then diffuses to CC-PPy AL and gets adsorbed by PPy to form $A\text{-}I_3^-$, CC+CC-PPy-120 should have the same charging voltage as CC+CC (1.32 V). Likewise, if $A\text{-}I_3^-$ desorbs from the CC-PPy AL to form $F\text{-}I_3^-$ and then diffuses to the CC CL to get reduced, it should occur at the same discharging voltage (1.25 V) as CC+CC. Neither case was observed. All devices with CC-PPy ALs not only have a lower charging voltage than the CC+CC device but also exhibit an extra discharging peak at a lower voltage (Figure 4.5). It suggested that the formation and reduction of $A\text{-}I_3^-$ take place at the CL/AL interface. During charging, $I^-$ ions migrate from the bulk electrolyte solution, transfer electrons to CL, and spontaneously form $A\text{-}I_3^-$ at the CL/AL interface. The generated $A\text{-}I_3^-$ ions will subsequently migrate into the bulk AL under a concentration gradient and re-

expose adsorption sites for other $I_3^-$ ions. During discharging, A-$I_3^-$ ions will diffuse from the bulk AL to the CL/AL interface under the concentration gradient and accept electrons from the CL to regenerate $I^-$ ions.

Moreover, the increase of the CE and the simultaneous decrease of the charging voltage (Figure 4.4a) imply that the PPy coating underwent certain transformations over the cycles to enhance its interactions with $I_3^-$. As shown in the differential capacity plots (Figure 4.4b), the signal corresponding to the reduction of A-$I_3^-$ increases over the cycles, while the signal of F-$I_3^-$ becomes lower. It implies that the formation of A-$I_3^-$ becomes more favorable over F-$I_3^-$ with an increasing $I_3^-$ adsorption capacity. The positive shift of the A-$I_3^-$ discharging voltage (Figure 4.4b) also indicates that the reduction of A-$I_3^-$ is improved. Taken together, the charging/discharging voltage gap of A-$I_3^-$ is getting narrower, suggesting improved kinetics of A-$I_3^-$/$I^-$ conversion over the cycles (Figure 4.6c). This conclusion is supported by the electrochemical impedance spectra (EIS) of 10 consecutive GCD cycles collected at the discharging voltage of A-$I_3^-$ (1.17 V) (Figure 4.7). The equivalent circuit resistance ($R_s$) and charge transfer resistance of the $Zn^{2+}$/Zn redox couple ($R_{ct1}$) remained unchanged, while the charge transfer resistance of the A-$I_3^-$/$I^-$ redox couple ($R_{ct2}$) drastically decreased in the first few cycles and then reached a stable state (Figure 4.4d). This result again indicates a possible PPy transformation during the first few charge/discharge cycles.

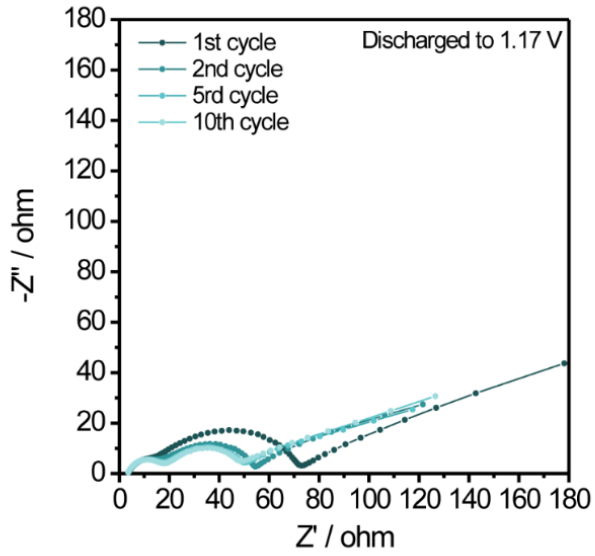


**Figure 4.7** EIS data collected from CC+CC-PPy-120 at 1.17 V over cycles.

To understand the possible transformation of PPy, we investigated its capacitive behaviors below 1.15 V (Figure 4.8a). The capacitances of CC+CC-PPy-*x* increase with PPy loading (Figure 4.9). The capacitive behavior of PPy comes from the anion doping (charging) and dedoping (discharging). The anions available under the given voltage window are sulfate ions ($SO_4^{2-}$) in the as-prepared PPy and $I^-$ in the electrolyte. Since $I^-$ ions are in excess and they have a smaller ionic size (0.220 nm) and lower charge than $SO_4^{2-}$ (0.230 nm),[25] anion exchange will likely take place on PPy over the initial cycles.[26] The capacitance signal at a deep discharge voltage (0.6 V) can be attributed to the dedoping of $SO_4^{2-}$. The significant decrease of this capacitive signal in the initial cycles [highlighted by the purple arrow in Figure 4.8a suggests the loss of $SO_4^{2-}$ upon discharging and the replacement by $I^-$ upon subsequent recharging. The

negatively shifted onset charging voltage [highlighted by the brown arrow in Figure 4.8(a) also implies the PPy is redoped by the kinetically more favorable $I^-$ instead of $SO_4^{2-}$. The capacitive oxidation ($I^-$ doping)/reduction ($I^-$ dedoping) of PPy has a 100% Coulombic efficiency (Figure 4.10). Above 1.15 V, PPy is completely charged (doped with an anion). We proposed a mechanism based on these data (Figure 4.8b). To elucidate this mechanism, elemental analysis was conducted to probe the AL compositional change over the cycles. As shown in Figure 4.8c, the variations of the sulfur and iodine contents on CC-PPy-120 ALs over the cycles show the opposite trend, in agreement with the proposed mechanism. We believed that the $I^-$ doped sites on CC-PPy AL are favorable for the adsorption of $I^0$ and, thus, increased the adsorption capacity and reaction kinetics over cycles. DFT simulations (Figure 4.8d) revealed that $I^-$ ions interact strongly with the PPy chains in oxidized state (denoted as $PPy^+ \cdot I^-$), with a Gibbs free energy change of adsorption ($\Delta G_{ads}$) of -1.05 eV. In contrast, the adsorption of the $I^-$ ions on graphene (CC surface) is less preferable because it has a $\Delta G_{ads}$ of +0.43 eV. Therefore, the doping of $I^-$ in the PPy chains is highly plausible. The optimized geometric structure of F-$I_3^-$ is identified as quasi-octahedral hexacoordinated $[Zn \cdot I_3 \cdot 5H_2O]^+$, which is consistent with the previous reports.[11,27] $[Zn \cdot I_3 \cdot 5H_2O]^+$ can physically adsorb to PPy ($\Delta G_{ads}$ = -2.155 eV, denoted as PPy-$[Zn \cdot I_3 \cdot 5H_2O]^+$) and graphene ($\Delta G_{ads}$ = -1.869 eV, denoted as Gr-$[Zn \cdot I_3 \cdot 5H_2O]^+$) through molecular interactions. Notably, it is thermodynamically more favorable for these three forms of $[Zn \cdot I_3 \cdot 5H_2O]^+$ to further transfer a molecular $I_2$ to $PPy^+ \cdot I^-$ to form $I_3^-$-doped PPy (denoted as $PPy^+ \cdot I_3^-$) given that an $I_3^-$ ion is an analogue to a molecular

$I_2$ linking to an $I^-$ ion with a weak chemical bond. Therefore, $PPy^+ \cdot I_3^-$ should be the most stable form of A-$I_3^-$, which shows a strong chemical adsorption to $I_3^-$ ions with a $\Delta G_{ads}$ of -0.612 eV.

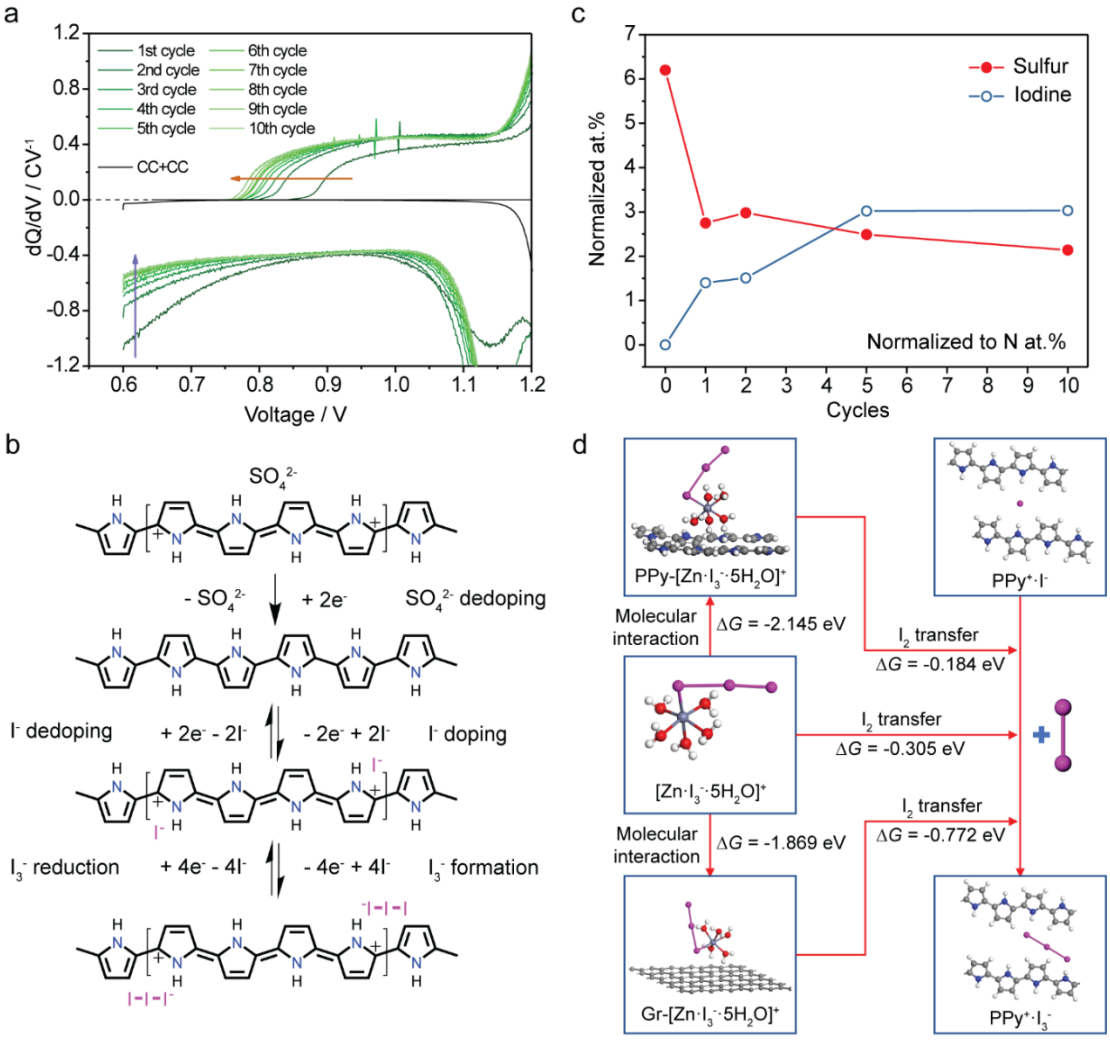


**Figure 4.8** (a) Magnified differential capacity plots of CC+CC (black) and CC+CC-PPy-120 (green) obtained at 0.5 C in PPy's capacitive voltage window; (b) Schematic illustration of anion exchange mechanisms on PPy and A-$I_3^-$ conversion reactions; (c) Normalized atomic contents of sulfur and iodine on the CC-PPy-120 charged at 1.15 V are plotted as a function of number of cycles; (d) DFT calculation results of the

evolution processes of F-$I_3^-$ and A-$I_3^-$, including optimized geometric structures and Gibbs free energy changes.

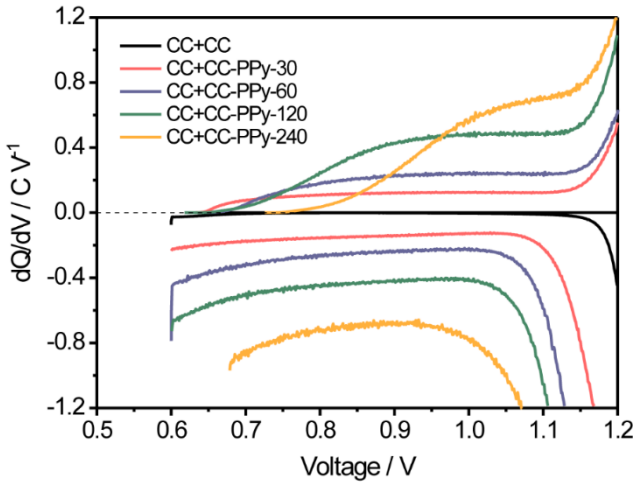


**Figure 4.9** Magnified differential capacity plots of CC+CC, CC+CC-PPy-30, CC+CC-PPy-60, CC+CC-PPy-120, and CC+CC-PPy-240 obtained in the capacitive voltage window at 0.5 C.

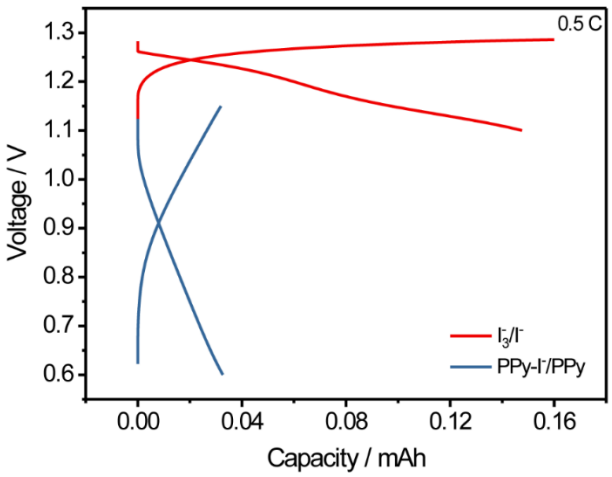


**Figure 4.10** Voltage profiles of CC+CC-PPy-120 obtained in different voltage windows at 0.5 C and maximum 10% depth of charge.

**Electrochemical Performances of ZIBs with Double-Layered Cathodes**

To evaluate the performances of ZIBs with double-layered cathodes, we conducted intermittent GCD tests for CC+CC and CC+CC-PPy-120 at different charge/discharge rates (Figures 4.11 and 1.12). The voltages were recorded at the beginning and the end of the standby processes (Figure 4.13a). The voltage difference represents the device's voltage loss during standby time (Figure 4.13b). CC+CC-PPy-120 exhibited much smaller voltage drops compared to CC+CC when the standby time extended from 15 min to 2 h, evidencing the contribution of PPy in suppressing self-discharge. Notably, when CC+CC stood for more than 60 min after being fully charged, the voltage drastically dropped by more than 300 mV to near 1.00 V due to the shuttling of generated F-$I_3^-$, resulting in the discharging capacities and CEs of CC+CC near zero

(Figure 4.13c). In contrast, the voltage of CC+CC-PPy-120 remained above 1.22 V even after 120 min of standby, which suggests that A-$I_3^-$ barely shuttled. This is confirmed by the differential capacity plots of CC+CC-PPy-120 (Figure 4.14), where the F-$I_3^-$ discharging peaks completely disappeared after the standby process, while the signal A-$I_3^-$ discharging remained unchanged and even slightly increased due to the capture of F-$I_3^-$ during standby. Benefitting from the $I_3^-$-adsorbing layer, CC+CC-PPy-120 achieved outstanding CEs up to 95.6% (0.5 C, 0 min standby), which are significantly better than those of CC+CC at all the charging/discharging rates we studied.

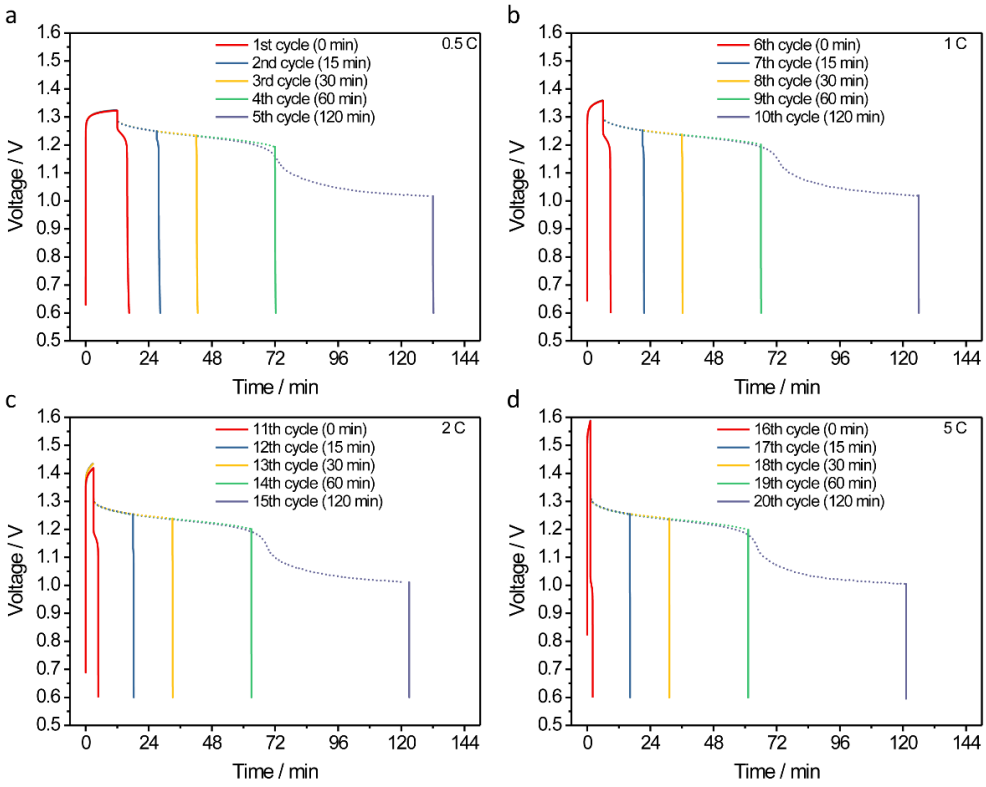

**Figure 4.11** GCD curves of CC+CC at (a) 0.5 C (1st to 5th cycles), (b) 1 C (6th to 10th cycles), (c) 2 C (11th to 15th cycles), and (d) 5 C (16th to 20th cycles) with different standby times (dashed lines).

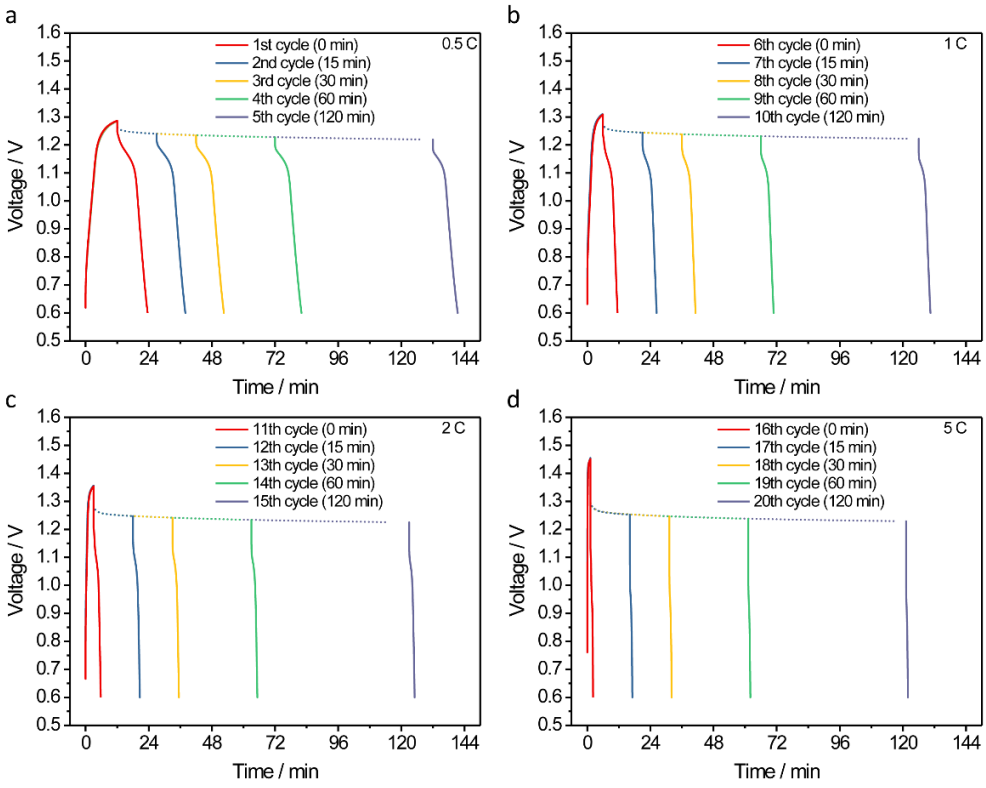


**Figure 4.12** GCD curves of CC+CC-PPy-120 at (a) 0.5 C (1st to 5th cycles), (b) 1 C (6th to 10th cycles), (c) 2 C (11th to 15th cycles), and (d) 5 C (16th to 20th cycles) with different standby times (dashed lines).

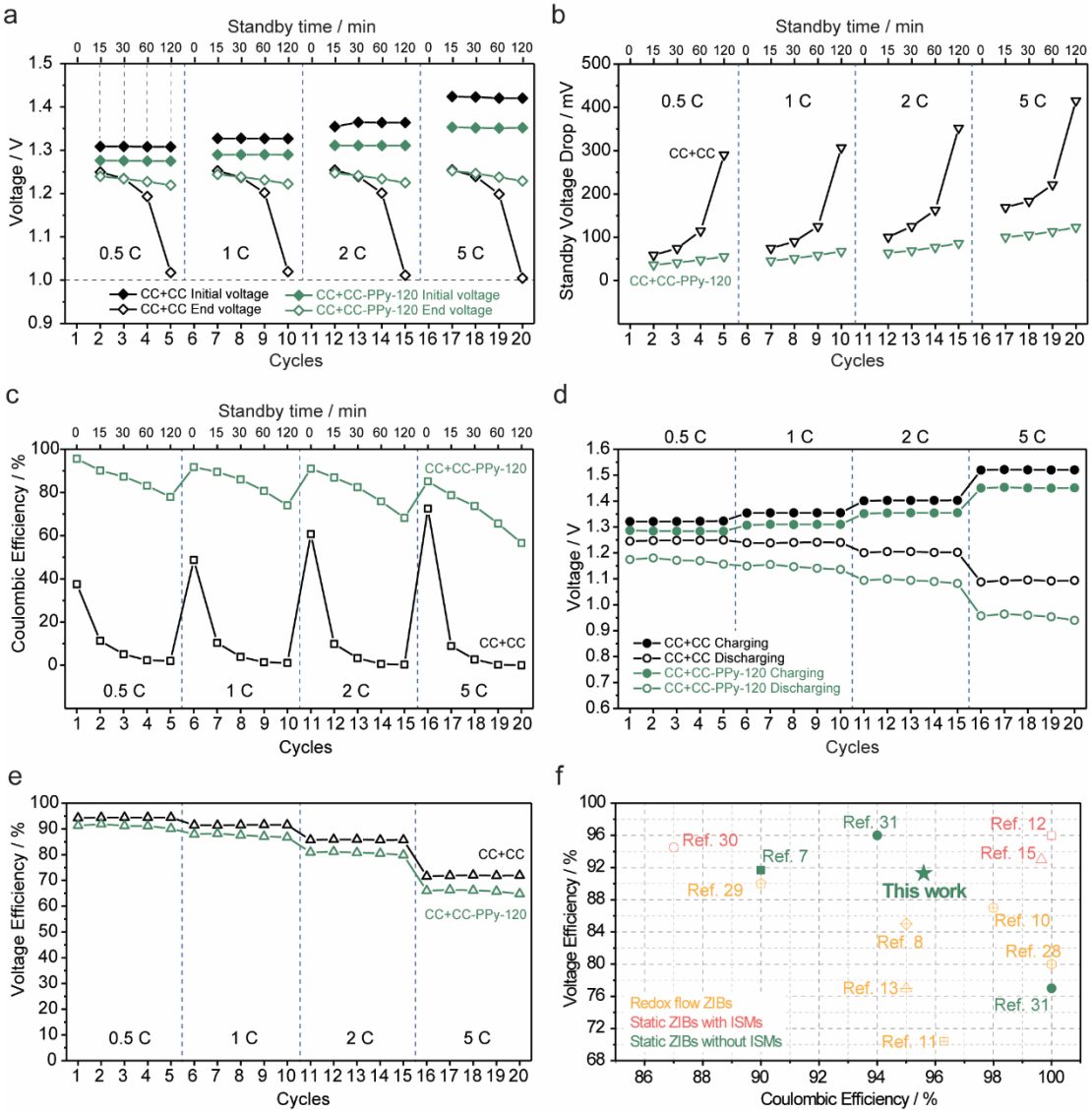


**Figure 4.13** Comparisons of the intermittent charge/discharge profiles of CC+CC and CC+CC-PPy-120 collected at different rates in terms of (a) voltage at the beginning and the end of standby process; (b) calculated voltage drops during standby process; (c) Coulombic efficiencies; (d) charging and discharging voltages; (e) voltage efficiencies. (f) Comparisons among other aqueous rechargeable Zn-$I_2$ batteries with iodine-free cathodes in terms of Coulombic efficiency and voltage efficiency.[7,8,10-13,15,28-31]

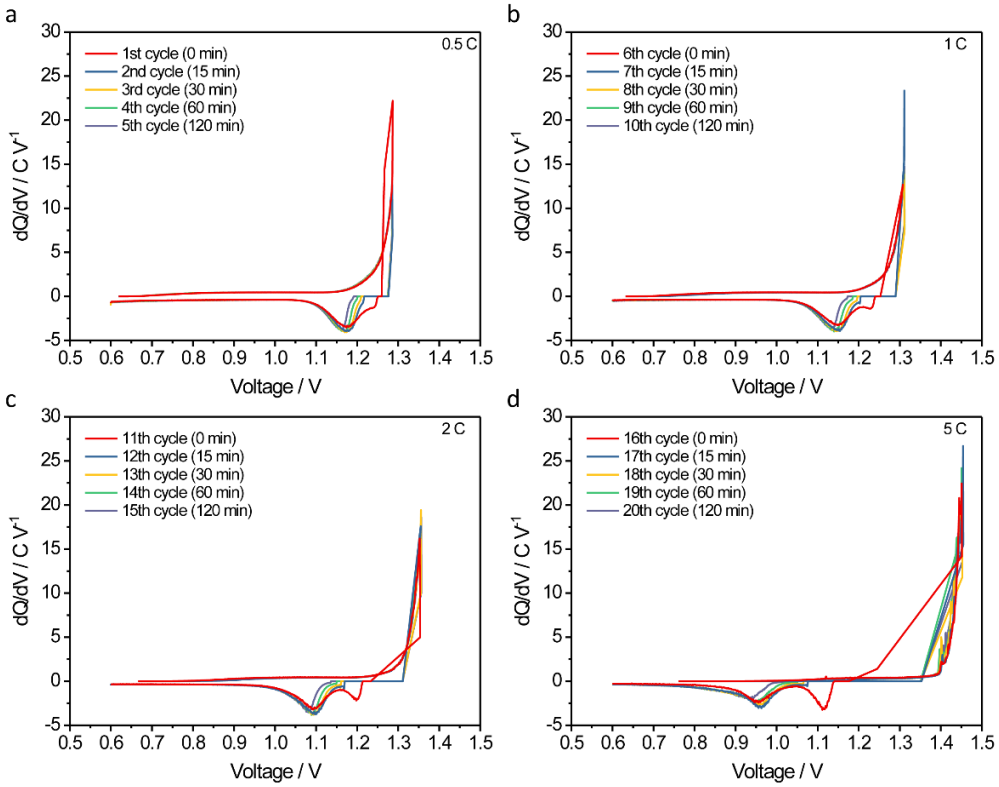


**Figure 4.14** Differential capacity plots of CC+CC-PPy-120 at (a) 0.5 C ($1^{st}$ to $5^{th}$ cycles), (b) 1 C ($6^{th}$ to $10^{th}$ cycles), (c) 2 C ($11^{th}$ to $15^{th}$ cycles), and (d) 5 C ($16^{th}$ to $20^{th}$ cycles) with different standby times.

Furthermore, we investigate the charging/discharging voltages of CC+CC-PPy-120 (Figure 4.13d) and CC+CC (Figure 4.15). Since A-$I_3^-$ is more thermodynamically favorable to form than F-$I_3^-$, the charging/discharging voltages of CC+CC-PPy-120 are lower than those of CC+CC at all rates (Figure 4.13d). Significantly, CC+CC-PPy-120 still delivered decent voltage efficiencies (VEs) at all rates, with only up to 5% (at 5 C) lower than that of CC+CC (Figure 4.13e). It means that the introduction of the CC-PPy-120 ALs did not severely hinder the charging/discharging kinetics. In comparison

to other aqueous rechargeable ZIBs with iodine-free cathodes, our prototypical ZIB with a double-layered cathode configuration achieved highly competitive CE (95%) and VE (91%) values (Figure 4.13f). When the device's depth of charge was increased to 20% (Figure 4.16), we observed a slight decrease of the CE because of the limited PPy loading ($I_3^-$ adsorption capacity) of CC-PPy-120. When switching to CC-PPy-240 with a higher PPy loading, the CE was largely restored up to 90%. The decrease of the VE at higher rates is due to the increased internal resistance, which can be addressed by optimizing the AL structure and polymer properties.

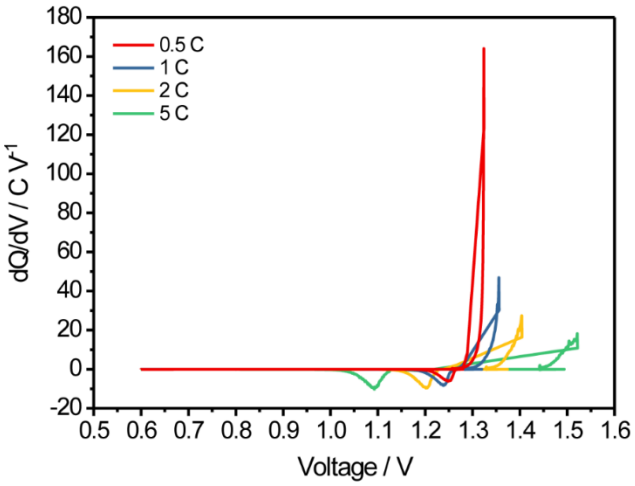


**Figure 4.15** Differential capacity plots of CC+CC at different rates in consecutive GCD tests.

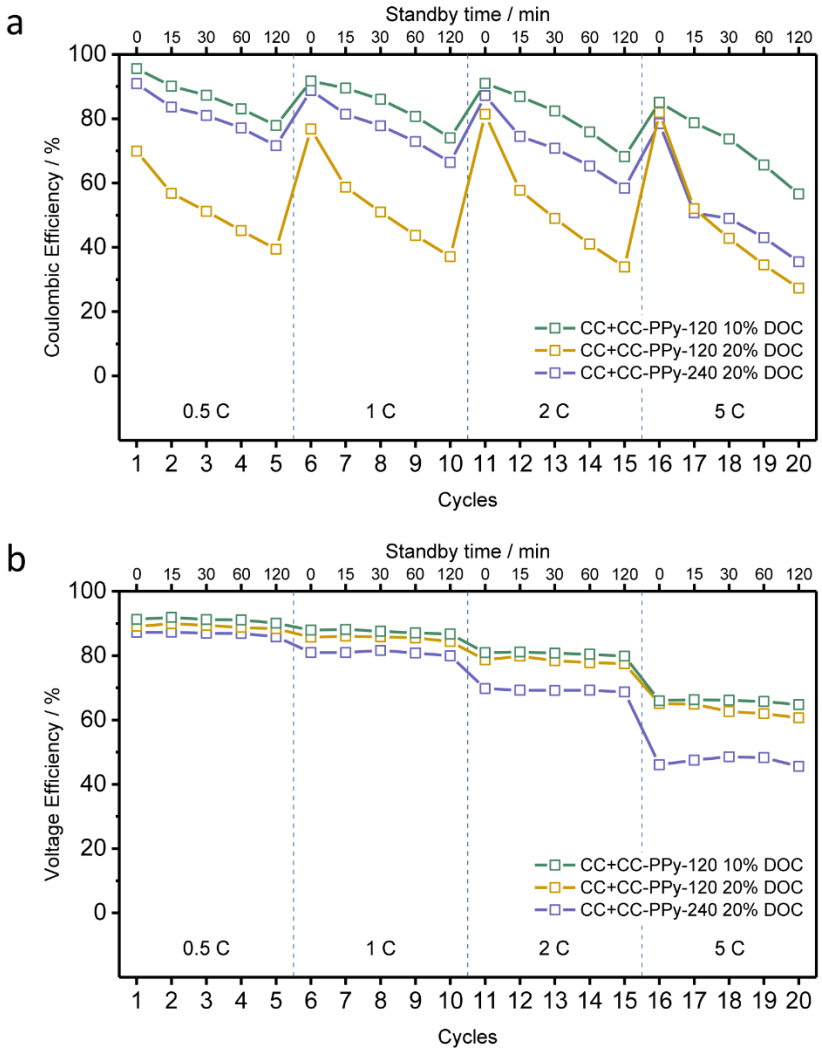


**Figure 4.16** (a) Coulombic efficiencies and (b) voltage efficiencies of CC+CC-PPy-120 (10% depth of charge), CC+CC-PPy-120 (20% depth of charge), and CC+CC-PPy-240 (20% depth of charge) obtained from intermittent charge/discharge tests at different rates.

Finally, we tested the retention of CE and VE of CC+CC and CC+CC-PPy-120 in long-term charge/discharge cycling at 0.5 C (Figure 4.17). Impressively, CC+CC-

PPy-120 maintained both a high CE (99.3% to 97.5%) and a high VE (92.5% to 87.9%) for 600 cycles. CC+CC showed a slightly better VE (95.1% to 91.1%) but a much lower CE below 40%. After 10 days of operation, the CC-PPy-120 AL showed no observable structural degradation (Figure 4.18). The outstanding consistency and durability of the CC-PPy ALs open up new opportunities for the design, fabrication, and applications of aqueous rechargeable ZIBs.

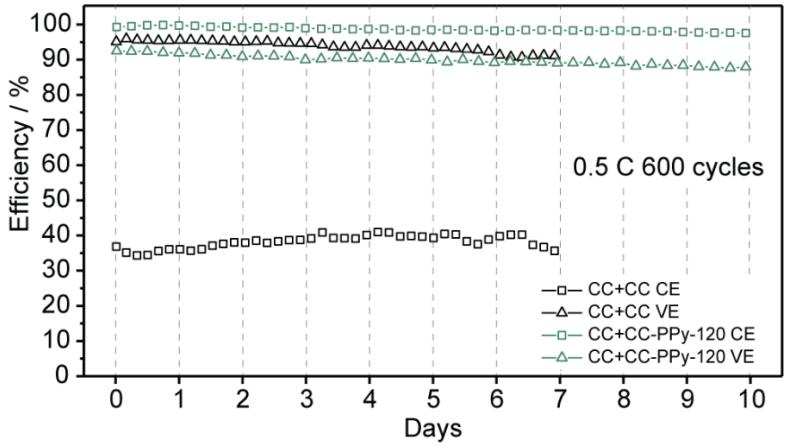


**Figure 4.17** Plots of cycling stability of Coulombic and voltage efficiencies of CC+CC and CC+CC-PPy-120 obtained at 0.5 C for 600 cycles.

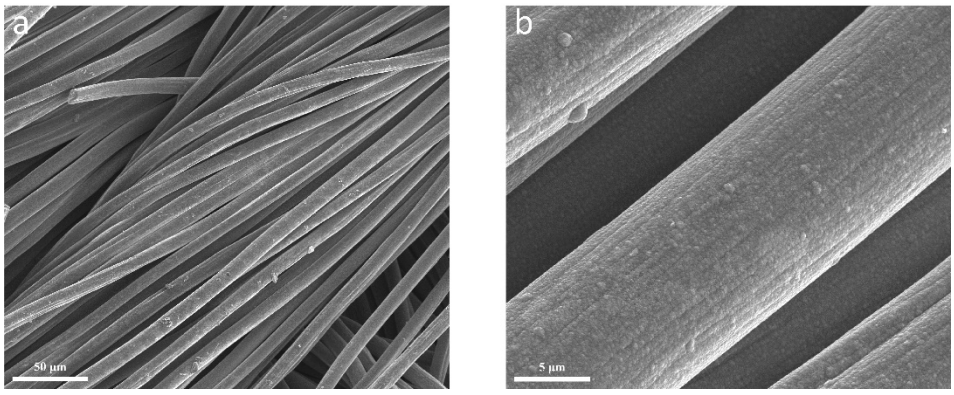


**Figure 4.18** SEM images of CC-PPy-120 AL after 10 days of charge/discharge.

## 4.4 Conclusion

In conclusion, we have demonstrated a new cathode configuration for aqueous rechargeable static ZIBs. The prototypical ZIB achieved a substantially enhanced CE (up to 95.6%) without compromising the VE (up to 91.3%) even at high-rate intermittent charge/discharge. The enhanced CE is attributed to the formation/reduction of adsorbed $I_3^-$ ions at the CL/AL interface, which effectively suppresses the shuttling of the $I_3^-$ ions while minimally affecting the charging/discharging kinetics. The successful validation of this device concept opens up new opportunities to the design, fabrication, and applications of the ZIBs. The conductive ALs could also be coupled with $I_2$/microporous carbon composite cathodes and work the same way as the interlayers in the Li-S batteries, which will possibly capture the discharging product ($I^-$) and serve as a conductive extension of the cathode to convert $I^-$ to $I_2$ during charging. Other batteries with liquid-liquid conversion reactions could also benefit from the double-layer cathode configuration to reduce the potential shuttle of active electrolyte species, such as vanadium cations, bromine, ferrocene, ferrocyanide, and organic molecules.

## References


1. Y. Li, H. Dai. *Chem. Soc. Rev.* **2014**, *43*, 5257-5275.
2. C. Xu, B. Li, H. Du, F. Kang. *Angew. Chem. Int. Ed.* **2012**, *51*, 933-935.
3. G. Fang, J. Zhou, A. Pan, S. Liang. *ACS Energy Lett.* **2018**, *3*, 2480-2501.
4. P. Yu, Y. Zeng, H. Zhang, M. Yu, Y. Tong, X. Lu. *Small* **2019**, *15*, 1804760.

5. Y. Yu, J. Xie, H. Zhang, R. Qin, X. Liu, X. Lu. *Small Sci.* **2021**, *1*, 2000066.

6. F. Wang, J. Tseng, Z. Liu, P. Zhang, G. Wang, G. Chen, W. Wu, M. Yu, Y. Wu, X. Feng. *Adv. Mater.* **2020**, *32*, 2000287.

7. J. J. Hong, L. Zhu, C. Chen, L. Tang, H. Jiang, B. Jin, T. C. Gallagher, Q. Guo, C. Fang, X. Ji. *Angew. Chem. Int. Ed.* **2019**, *58*, 15910-15915.

8. C. Xie, H. Zhang, W. Xu, W. Wang, X. Li. *Angew. Chem. Int. Ed.* **2018**, *57*, 11171-11176.

9. H. Pan, B. Li, D. Mei, Z. Nie, Y. Shao, G. Li, X. S. Li, K. S. Han, K. T. Mueller, V. Sprenkle, J. Liu. *ACS Energy Lett.* **2017**, *2*, 2674-2680.

10. B. Li, J. Liu, Z. Nie, W. Wang, D. Reed, J. Liu, P. McGrail, V. Sprenkle. *Nano Lett.* **2016**, *16*, 4335-4340.

11. B. Li, Z. Nie, M. Vijayakumar, G. Li, J. Liu, V. Sprenkle, W. Wang. *Nat. Commun.* **2015**, *6*, 6303.

12. Z. Wang, J. Huang, Z. Guo, X. Dong, Y. Liu, Y. Wang, Y. Xia. *Joule* **2019**, *3*, 1289-1300.

13. G.-M. Weng, Z. Li, G. Cong, Y. Zhou, Y.-C. Lu. *Energy Environ. Sci.* **2017**, *10*, 735-741.

14. Y. Li, L. Liu, H. Li, F. Cheng, J. Chen. *Chem. Commun.* **2018**, *54*, 6792-6795.

15. H. Yang, Y. Qiao, Z. Chang, H. Deng, P. He, H. Zhou. *Adv. Mater.* **2020**, *32*, 2004240.

16. A. J. Bard, L. R. Faulkner, *Electrochemical Methods: Fundamentals and Applications*. 2nd ed.; New York: John Wiley & Sons, **2000**, 608-619.

17. M. J. Goodwin, B. W. Steed, D. S. Yufit, O. M. Musa, D. J. Berry, J. W. Steed. *Cryst. Growth Des.* **2017**, *17*, 5552-5558.

18. H.-U. Schenck, P. Simak, E. Haedicke. *J. Pharm. Sci.* **1979**, *68*, 1505-1509.

19. S. Moulay. *J. Polym. Eng.* **2013**, *33*, 389-443.

20. F.-s. Cai, Y.-q. Duan, Z.-h. Yuan. *J. Mater. Sci.: Mater. Electron.* **2018**, *29*, 11540-11545.

21. G. Kresse, J. Furthmüller. *Phys. Rev. B* **1996**, *54*, 11169-11186.

22. P. E. Blöchl. *Phys. Rev. B* **1994**, *50*, 17953-17979.

23. G. Kresse, D. Joubert. *Phys. Rev. B* **1999**, *59*, 1758-1775.

24. S. Grimme, J. Antony, S. Ehrlich, H. Krieg. *J. Chem. Phys.* **2010**, *132*.

25. Y. Marcus. *Chem. Rev.* **1988**, *88*, 1475-1498.

26. H. Ge, G. G. Wallace. *React. Polym.* **1992**, *18*, 133-140.

27. W. Li, K. Wang, K. Jiang. *J. Mater. Chem. A* **2020**, *8*, 3785-3794.

28. J. Zhang, G. Jiang, P. Xu, A. Ghorbani Kashkooli, M. Mousavi, A. Yu, Z. Chen. *Energy Environ. Sci.* **2018**, *11*, 2010-2015.

29. C. Xie, Y. Liu, W. Lu, H. Zhang, X. Li. *Energy Environ. Sci.* **2019**, *12*, 1834-1839.

30. K. Lu, H. Zhang, B. Song, W. Pan, H. Ma, J. Zhang. *Electrochim. Acta* **2019**, *296*, 755-761.

31. J. Lee, P. Srimuk, S. Fleischmann, A. Ridder, M. Zeiger, V. Presser. *J. Mater. Chem. A* **2017**, *5*, 12520-12527.

# Chapter 5 - Outlook

The previous chapters of this dissertation have discussed the developments and optimizations of different cathodes based on their individual mechanisms and challenges, which have improved their performances for different device applications. Integrated with the advances of other research works, lab-scale cathodes and devices will progress to further industrialization and commercialization. Yet, one should keep in mind that the improvements in cathodes are never limited to making better cathode materials. The performances of a cathode material are closely related to other factors, including electrode morphology, electrolyte properties, device assembly, testing conditions, performance indicators, and much more.

The morphology of an electrode, such as particle size, thickness, density and porosity, distributions of materials, etc., can significantly affect the utilization of active materials.[1,2] For example, large particles may experience inefficient penetration of ions into the interior domains and pulverization due to volume change, while small particles may easily agglomerate and have less contact with conducting additives.[3] Thin electrodes prevail in ion accessibility and material utilization but fail to store high capacity.[4] Porous electrodes are commonly used to improve ion diffusion, which in the meantime sacrifice electrical conductivity and structural integrity.[5] Nonetheless, a homogeneous mixture of active material particles, conducting additives and binders is important for constructing efficient and robust electron pathways for active materials.[6] The optimizations of electrode morphologies require a clear understanding of material

properties, empirical knowledge from countless try-and-errors in electrode fabrication, as well as the assistance of the developing characterization and simulation techniques.

The interaction and synergy between electrode materials and electrolytes are also critical in harnessing the potential of cathode material, because the energy storage processes during charging/discharging always require the participation of the ions and even solvents in the electrolyte.[7] One obvious example, which is also a major lesson in the research work of Chapter 3, is the pairing of $MnO_2$ with different electrolytes. $MnO_2$ achieved promising results in previous publications even with ultrahigh loadings and film thicknesses thanks to the pseudocapacitive behaviors originated from fast reversible surface redox reactions of adsorption/desorption of hydronium, although the voltage window is limited to avoid water splitting and $MnO_2$ dissolution.[8] The switch from aqueous to $Li^+$-based non-aqueous electrolyte, while extended the voltage window in absence of water-involving side reactions, greatly changed the reaction mechanisms to insertion/desertion of $Li^+$ due to the elimination of water and proton. The insertion/desertion of $Li^+$ is kinetically much slower, which is attributed to the larger size of $Li^+$, participation of bulk materials, and the higher energy required for desolvation.[9,10] Under the extended voltage window, $MnO_2$ showed higher overall capacity, lower rate capability, more structural degradation during cycling, and worse performances at a higher loading and film density/thickness. Therefore, rational electrolyte design and pairing helps to make use of strengths and avoid weaknesses of the cathode material. As previously mentioned, property understanding, empirical knowledge and modern technique assistance are necessary. In addition, insight studies

of different electrode/electrolyte combinations regardless of performances are encouraged to help build a database for future reference.

The performances of cathodes are also largely determined from the device level, especially when the manufacture is scaled up.[11] For example, the voltage and current distributions could differ depending on the electrode size and the current input/output position, which is worth more concern for self-standing electrodes with inferior electrical conductivity and large sizes without conductive current collectors like Cu foil or Al foil.[12] In fact, this problem essentially led to the use of Ti gauze wrapping strategy and the limited electrode area in the research work of Chapter 2 in order to compensate for the conductivity decay of the thick 3D printed carbon cathode. Besides, electrolyte volume varies drastically from lean-electrolyte cells (Swagelok cells and coin cells) to electrolyte-adjustable pouch cells to flooded cells (beaker cells and flow cells). Large electrolyte volume offers sufficient ion supply and higher tolerance to side reactions, generally benefiting the performance of electrodes. However, large electrolyte volume does harm to gravimetric/volumetric performances and device cost, which is not favored in commercial products.[13] The selection of device configurations also affects the stacking density of electrodes. Dense and compact packing of electrodes commonly seen in commercialized devices, while may facilitate ion transport and mitigate volume change and pulverization (thin-film electrodes), may also risk separator piercing (rough-surface electrodes) and structural collapse (thick and fragile electrodes).[14] Moreover, the electrochemical behaviors of electrodes could alter with counter electrode, reference electrode, flow status of electrolyte, use of separator, *etc.* Hence,

the reasonable selection, and more importantly, creative and case-specific design of device configurations play an indispensable role in maximizing the performances of cathodes.

Testing conditions, including the parameter settings of electrochemical tests and environmental factors, should not be underestimated when studying a cathode material. Voltage window, for instance, needs to be carefully determined, as inappropriate voltage windows can result in side reactions (too wide) or unutilized capacity (too narrow).[15] The range of current densities (galvanostatic charge/discharge) or scan rates (cyclic voltammetry) is also tricky. Low rates allow higher degrees of both favorable and unfavorable reactions, which normally deliver higher capacity but poorer stability, while high rates do the opposite.[16] Other tunable testing protocols include electrode activation, potentiostatic charging, state of charge, intermittent charge/discharge, orders of testing techniques, *etc.*[17] One of the most profound environmental factors is temperature. Low temperature, for example, limits ion mobility and reaction kinetics. Under low temperatures, cathodes based on bulk insertion/desertion of large ions and slow conversion reactions are severely disabled, while those based on EDLC, pseudocapacitance, and proton-storage reactions could largely survive only if the cathode is also conductive enough.[18] Unfortunately, the fine-tuning of testing conditions has no shortcut but to rely on experience and trials. Future developments of powerful macroscale simulation tools and assistance from artificial intelligence should speed up this process.

Finally, to correctly evaluate the performance of a cathode and make fair comparisons with other reported works, suitable indicators need to be discussed.[19] Among performance indicators, the most argued is the usage of gravimetric, areal, and volumetric capacitance/capacity, where the gravimetric data of ultralow-loading electrodes, the areal data of ultrathick electrodes, and the volumetric data of ultrathin electrodes are often exaggerated. Making comparisons of these data without highlighting the mass loading and size could be unfair and meaningless. The use of capacitance and capacity is another long-debated topic, where the former is only valid when describing electrodes and devices with unambiguous capacitive behaviors while the latter is more universal. Likewise, the calculations of capacitance from cyclic voltammetry curves and energy density from galvanostatic charge/discharge curves of supercapacitors involve many approximations, which can cause noticeable errors for non-capacitive electrodes and devices. Thus, standardized data report protocols, which allow self-consistent calculations of different performance indicators from complete original data, should be promoted in the research community.

## References


1. L. Zhang, W. Wang, X. Ma, S. Lu, Y. Xiang. *Nano Today* **2021**, *37*, 101074.
2. X. Xue, D. Lin, Y. Li. *Small Struct.* **2022**, *3*, 2200159.
3. W.-J. Zhang. *J. Power Sources* **2011**, *196*, 2962-2970.
4. J. Ni, L. Li. *Adv. Mater.* **2020**, *32*, 2000288.

5. J. C. Stallard, L. Wheatcroft, S. G. Booth, R. Boston, S. A. Corr, M. F. L. De Volder, B. J. Inkson, N. A. Fleck. *Joule* **2022**, *6*, 984-1007.

6. R. Gonçalves, S. Lanceros-Méndez, C. M. Costa. *Electrochem. Commun.* **2022**, *135*, 107210.

7. D. Aurbach, B. Markovsky, G. Salitra, E. Markevich, Y. Talyossef, M. Koltypin, L. Nazar, B. Ellis, D. Kovacheva. *J. Power Sources* **2007**, *165*, 491-499.

8. B. Yao, S. Chandrasekaran, J. Zhang, W. Xiao, F. Qian, C. Zhu, E. B. Duoss, C. M. Spadaccini, M. A. Worsley, Y. Li. *Joule* **2019**, *3*, 459-470.

9. J. Duay, S. A. Sherrill, Z. Gui, E. Gillette, S. B. Lee. *ACS Nano* **2013**, *7*, 1200-1214.

10. N. F. Carvalho, J. R. Pliego. *Phys. Chem. Chem. Phys.* **2015**, *17*, 26745-26755.

11. A. Kwade, W. Haselrieder, R. Leithoff, A. Modlinger, F. Dietrich, K. Droeder. *Nat. Energy* **2018**, *3*, 290-300.

12. P. Taheri, A. Mansouri, B. Schweitzer, M. Yazdanpour, M. Bahrami. *J. Electrochem. Soc.* **2013**, *160*, A1731.

13. M. Zhao, B.-Q. Li, H.-J. Peng, H. Yuan, J.-Y. Wei, J.-Q. Huang. *Angew. Chem. Int. Ed.* **2020**, *59*, 12636-12652.

14. R. Li, W. Li, A. Singh, D. Ren, Z. Hou, M. Ouyang. *Energy Storage Mater.* **2022**, *52*, 395-429.

15. C. Liu, Z. G. Neale, G. Cao. *Mater. Today* **2016**, *19*, 109-123.

16. Y. Lu, C.-Z. Zhao, H. Yuan, X.-B. Cheng, J.-Q. Huang, Q. Zhang. *Adv. Funct. Mater.* **2021**, *31*, 2009925.

17. R. Dugas, J. D. Forero-Saboya, A. Ponrouch. *Chem. Mater.* **2019**, *31*, 8613-8628.

18. Q. Nian, T. Sun, S. Liu, H. Du, X. Ren, Z. Tao. *Chem. Eng. J.* **2021**, *423*, 130253.

19. T. S. Mathis, N. Kurra, X. Wang, D. Pinto, P. Simon, Y. Gogotsi. *Adv. Energy Mater.* **2019**, *9*, 1902007.